Large-scale Ocean Circulation Observed from Autonomous Profiling Floats

Alison R. Gray

A dissertation
submitted in partial fulfillment of the
requirements for the degree of

Doctor of Philosophy

University of Washington

2014

Reading Committee:

Stephen C. Riser, Chair

Susan L. Hautala

Peter B. Rhines

Program Authorized to Offer Degree:
School of Oceanography

University of Washington

Abstract

Large-scale Ocean Circulation Observed from Autonomous Profiling Floats

Alison R. Gray

Chair of the Supervisory Committee:
Professor Stephen C. Riser
School of Oceanography

The general circulation of the ocean plays a central role in the global transport of heat, freshwater, carbon, oxygen, nutrients, and other constituents. The ocean's large-scale circulation strongly influences the distribution of these important quantities and thus shapes both global climate and patterns of marine biological production. Observations of large-scale circulation, however, have traditionally been limited in both space and time because of the resource-intensive nature of shipboard observations and the sheer magnitude of the world's oceans. The focus of this dissertation is to examine the large-scale circulation of the ocean using observations from the Argo array of autonomous profiling floats, which have unprecedented resolution in both space and time. A novel multi-scale optimal analysis method is developed and applied in order to map the hydrographic and velocity data provided by the Argo floats. Using this method monthly estimates of absolute geostrophic velocities, potential temperature, and salinity in the upper 2000 decibars of the global ocean are computed for the period December 2004 to November 2010. These results are then combined with satellite observations of wind stress to assess the extent to which observed geostrophic transports are accurately predicted by Sverdrup balance, a simple but ubiquitous theory of the relationship between wind-forcing and ocean circulation. Within the uncertainties, good agreement is found over a large portion of the global ocean, namely

the interior subtropics and tropics, while poorer agreement is found in the high latitudes and boundary regions. The meridional overturning circulation in the Southern Ocean, which plays an important role in the global climate system, is investigated using the computed absolute geostrophic velocity fields, together with eddy thickness fluxes also estimated from the Argo data. The resulting direct observations of the overturning circulation are examined in terms of spatial variability, and the relative contributions of the mean and eddy components of the overturning are determined. In addition to the scientific results found here, this dissertation demonstrates that measurements from the Argo array of profiling floats can be used to quantitatively estimate the large-scale circulation of the global ocean with unparalleled spatial and temporal resolution.

TABLE OF CONTENTS

LIST OF FIGURES

LIST OF TABLES

ACKNOWLEDGMENTS

I would like to thank, first and foremost, my advisor Stephen Riser for his consistent support and guidance throughout my time in graduate school. I am incredibly grateful that I have had Steve as an advisor, mentor, colleague, and friend.

I have learned a great deal from and enjoyed working with all of the members of my committee: Peter Rhines, Susan Hautala, Kathyrn Kelly, Steve Emerson, and Chris Bretherton. This work has been greatly influenced by my interactions with my committee members, and I am very grateful for their input and support.

My experience in graduate school has been greatly enhanced by my relationships with current and former UW students, particularly Nick Beaird, Sally Warner, Sara Bender, Li Ren, Jesse Anderson, and Eleanor Frajka-Williams.

The Argo data used in this work were collected by the International Argo Program and the many national programs that have been involved. I thank each of the many agencies and individuals that have contributed to Argo over the past decade.

Last but not least, I am endlessly grateful to my husband, David, for his continual support and encouragement over the years.

DEDICATION

To my seventh-grade teacher, Mrs. Harvey.

Chapter 1
INTRODUCTION

Covering more than 70% of the Earth's surface and containing an immense amount of heat, freshwater, carbon, and oxygen, the world ocean constitutes an important part of the Earth system. The gyres and currents that make up the large-scale circulation of the ocean govern the uptake, storage, and transport of these quantities (Talley et al., 2011b; Siedler et al., 2013). The large-scale circulation is therefore thought to strongly influence both the global climate system (Hartmann, 1994) and marine biological productivity (Mann and Lazier, 2006). Accordingly, the large-scale circulation and the forces that control it have been a topic of central importance in oceanography since the beginning of the field (see Talley et al., 2011a, for a brief history). Two of the primary factors driving the large-scale circulation are forcing due to wind stress and forcing due to changes in buoyancy (Talley et al., 2011b).

On a global basis, the stress of the wind acting on the ocean surface introduces approximately 1×10^{12} watts of energy into the ocean, which is eventually dissipated through small-scale motions (Munk and Wunsch, 1998). The spatial and temporal patterns of the wind power over the global ocean (e.g., Liu et al., 2008) help shape the large-scale circulation. One of the simplest relationships that describes how wind forcing drives ocean circulation was first proposed by Harald Sverdrup in 1947 (Sverdrup, 1947). Fundamentally a statement about the conservation of potential vorticity, this model, known as Sverdrup balance, relates wind stress curl to meridional geostrophic transport in the ocean interior through basic Ekman dynamics. Sverdrup balance forms a cornerstone for our understanding of the large-scale wind-driven circulation.

Another aspect of the large-scale circulation, the global meridional overturning

circulation (MOC), is forced in part by changes in buoyancy. The MOC, often conceptualized as "the great ocean conveyor belt", consists of dense waters that sink in a few places around Antarctica and in the high latitude North Atlantic (Talley et al., 2011b). These waters, which form the deep and bottom water masses that fill the global ocean, must be returned to the surface ocean eventually in order to complete the circuit. The resulting overturning circulation, which has a time scale on the order of 1,000 years, is thought to be one of the primary mechanisms by which the ocean affects the global climate system over longer time periods. The Southern Ocean has been proposed to play an important role in the upwelling branch of the global MOC, and a great deal of work, especially theoretical and numerical studies, has been focused on understanding the dynamics of this unique region (for an overview, see Rintoul et al., 2001).

Although models that describe how the winds and changes in buoyancy force the large-scale circulation were first proposed many decades ago, our ability to test these theories directly using observations has been limited historically because the available observations, especially of the subsurface ocean, have been limited in space and time. However, the Argo array of autonomous profiling floats, an in situ observing system for the upper ocean developed over the past twenty years, now provides a vast data set that can be used to analyze the forces that govern the large-scale circulation.

The Argo array consists of over three thousand autonomous semi-Lagrangian floats deployed throughout most of the global ocean (Roemmich et al., 2004). Each float collects profiles of temperature and salinity in the upper 2000 db, typically every ten days, and then transmits those data to shore-based centers in real-time. Between profiles, the float drifts with the predominant currents at a preprogrammed pressure, usually around 1000 decibars (db). The trajectory of a float, as recorded by satellite positioning systems when the float is at the surface, can be used to estimate the absolute geostrophic velocity at depth. In this dissertation, these subsurface velocity estimates are used together with the temperature and salinity profiles to quanti-

tatively estimate the global large-scale ocean circulation directly from observations. The resulting estimate, which is purely data-based, has a number of important advantages, including no ad hoc assumption regarding the reference velocity, quantitative error estimates at each grid point, and greatly improved coverage in space and time compared to previous data sets.

The overall objective of this work is to investigate the forces that shape the large-scale circulation of the global ocean, using observations primarily from the Argo array of autonomous profiling floats. To accomplish this, the data are first mapped to a regular grid in space and time using a new multi-scale objective analysis method. This method, which builds on the work by Bretherton et al. (1976), Davis (1985), and LeTraon (1990), is developed, tested, and then applied to Argo data in Chapter 2. In Chapter 3, the resulting estimates of velocity, temperature, and salinity in the upper 2000 db of the global ocean, together with satellite wind stress observations, are used to assess Sverdrup balance, the simple theory of the wind-driven circulation, on a global, point-by-point basis. Chapter 4 presents an analysis of the meridional overturning circulation in the upper portion of the Southern Ocean conducted using the velocity estimates and temperature and salinity data collected by the Argo floats as well as observations of wind stress. Lastly, concluding remarks are given in Chapter 5. Chapters 2, 3, and 4 are intended to stand alone as individual research articles that either have been published in or will be submitted to peer-reviewed journals, co-authored with S. C. Riser.

Chapter 2

A METHOD FOR MULTISCALE OPTIMAL ANALYSIS WITH APPLICATION TO ARGO DATA

This study presents an optimal analysis method for estimating large and small scale components of a field from observations. This technique uses an iterative generalized least squares procedure to determine the statistics of the small scale fluctuations directly from the data and thus is especially valuable when such information is not known a priori. The use of spherical radial basis functions in fitting the large scale signal is suggested, particularly when the domain is sufficiently large. This method is used to map simulated dynamic height data, salinities taken from high resolution model output, and absolute geostrophic velocities computed from Argo data. These applications illustrate some of the properties of this procedure and demonstrate its utility.

2.1 Introduction

Oceanographic data are often mapped to a regular grid to aid in further analysis and interpretation. One of the most commonly used mapping methods, objective analysis (also known as Kriging in geological sciences or optimal interpolation in atmospheric sciences) was introduced in oceanography by Bretherton et al. (1976). The simplest form of objective analysis requires that the data being mapped have zero mean. Given that oceanographic fields typically consist of a large scale signal combined with signals at the mesoscale and smaller scales, most observational data sets do not satisfy this condition. Bretherton et al. (1976) expanded the basic objective analysis method to estimate a constant mean, and Bretherton and McWilliams (1980) analyzed the

case where a spatially variable but perfectly known mean field is removed from the data. LeTraon (1990) further developed this technique to simultaneously estimate a large scale signal and a small scale field. To achieve this multiscale mapping, the procedure combines the objective function fitting technique given by Davis (1985) with conventional objective analysis. One significant advantage of this method is that the associated error estimates fully account for the uncertainties in both the large and small scale signals. This method has been applied to a wide variety of oceanographic data (e.g., Gruber and Sarmiento, 1997; Key et al., 2004; Kwon and Riser, 2004; Frankignoul et al., 2011; Ren et al., 2011; Pelland et al., 2013; Thomas et al., 2013).

In both traditional objective analysis and the multiscale method described by LeTraon (1990), the accuracy of the resulting mapped field depends on the validity of the specified covariance of the signal (the small scale component in the multiscale case). Often the statistics of the small scale field are not known a priori, and thus an educated guess is made for the shape of the covariance function as well as the decorrelation length scale and variance. If the chosen function happens to correctly represent the true covariance, the mapped field will be optimal. However, the accuracy of the selected covariance function is not typically assessed. To address this problem, the method presented here objectively estimates the required covariance function directly from the data using iterative generalized least squares (IGLS). This multiscale optimal analysis technique, which is an extension of the LeTraon (1990) method, is the first to implement this iterative procedure in an oceanographic context (although Bretherton et al. (1976) briefly touch on the basic idea). Gray and Riser (2014) used this method to produce global absolute geostrophic velocity fields from Argo data; in this paper we give a detailed description and discussion of the technique, along with the results of validation tests.

In addition to stipulating the covariance of the small scale signal, the optimal analysis method described here requires the choice of a set of complete basis functions to

use in fitting the large scale field. For small domains that can be adequately projected into Cartesian coordinates, many such functional sets exist (e.g.,$\{x^n\}$, $\{\sin(nx), \cos(nx)\}$, Legendre polynomials). Due to the advent of global ocean observing systems such as the Argo array of profiling floats (Roemmich et al., 2004), as well as concurrent increases in computing capabilities, mapping data over larger regions is increasingly common. In cases where the Earth's spherical geometry must be taken into account, only a few sets of basis functions are suitable. Spherical harmonics, the solutions to Laplace's equation on the surface of a sphere, are used extensively to model data in a wide variety of scientific fields including geophysics, atmospheric sciences, and astronomy (MacRobert and Sneddon, 1967). When applied to basin scale or global fitting, however, spherical harmonics suffer from a number of disadvantages. The periodic nature of these functions can lead to unrealistic oscillations, especially in areas with poor data coverage. Because spherical harmonics have global support, a change in the data at one location will affect the fit everywhere in the domain, giving an unphysical response.

In contrast, spherical radial basis functions (SRBFs; Fasshauer and Schumaker, 1998; Freeden et al., 1998) satisfy the necessary requirements for least squares approximation on the sphere and avoid both of these problems, thereby providing a reliable technique that is also exceptionally effective for interpolating scattered bivariate data (Franke, 1982). The main disadvantage of using these functions for approximation is that the user must make several choices when specifying the SRBFs, some of which can require additional computation. Proper design of the SRBFs is necessary to avoid ill-conditioned linear systems that produce inaccurate results (Narcowich and Ward, 1991). While SRBFs have been used in geophysics and other fields for many years (e.g., Hardy, 1990; Tuch, 2004; Tsai and Shih, 2006; Klees et al., 2008), the method presented in this paper highlights their application in fitting oceanographic data.

In the following, we begin by describing the IGLS procedure used to determine the covariance of the small scale signal directly from the data and subsequently compute

a multiscale estimate of the field. Next the use of SRBFs in fitting the large scale component of the field is discussed. Finally, this method is applied to three test cases: (1) simulated dynamic height fields, (2) high resolution model output, and (3) absolute geostrophic velocities computed using observations from the Argo array.

2.2 Iterative generalized least squares

Consider a set of N observations of a field d at positions $\mathbf{x}_n$: $\tilde{d}(\mathbf{x}_n)(n = 1, \cdots, N)$. For simplicity we first present the case where the observations are simultaneous and d is a scalar quantity. This method is also particularly well-suited for non-simultaneous data, which will be discussed further in Section 2.4.1. In addition, it can be adapted for analyzing vector data and for mapping fields related to the observations through linear operators, following the procedures detailed by Bretherton et al. (1976) and LeTraon (1990) for each of those cases.

Assume the field d consists of two components which have distinct spatial scales, so that $d(\mathbf{x}) = \{d(\mathbf{x})\} + d'(\mathbf{x})$. The smoothing operator $\{\cdot\}$ denotes the large scale (low wavenumber) signal, and the prime signifies the small scale signal, which is simply the anomaly from the large scale field. An observation $\tilde{d}(\mathbf{x}_n)$ can thus be decomposed into three parts

$$\tilde{d}(\mathbf{x}_n) = d(\mathbf{x}_n) + \varepsilon_d(\mathbf{x}_n) = \{d(\mathbf{x}_n)\} + d'(\mathbf{x}_n) + \varepsilon_d(\mathbf{x}_n) \quad , \tag{2.1}$$

where the noise $\varepsilon_d(\mathbf{x}_n)$ combines both measurement error and smaller unresolvable scales of d. The scale separation is strictly statistical and therefore does not necessarily correspond to different physical processes.

The large scale field is estimated using the objective function fitting procedure of Davis (1985), which corresponds to the standard statistical technique of generalized least squares (GLS). Unlike ordinary least squares, GLS does not require that the residuals from the fit be uncorrelated with each other and have equal variance. For most oceanographic data sets, we fully expect that the residuals, i.e., the small scale

anomalies, will be correlated. According to the Gauss-Markov theorem, GLS gives the best linear unbiased estimate under such conditions (Kariya and Kurata, 2004). Furthermore, the large scale component of a typical oceanographic field has neither zero mean nor known (or even clearly definable) covariance. GLS is thus usually preferable to standard objective analysis for determining the large scale signal (Davis, 1985). For more details about objective function fitting and GLS in general, the reader is referred to Davis (1985) and Kariya and Kurata (2004).

In objective function fitting, the data are fit to a set of M functions $F_m(\mathbf{x})(m = 1, \cdots, M)$, which form a subset of a complete set of basis functions. The selected functions have spatial scales larger than a specified cutoff, which should be chosen to retain the large scale elements of the field and eliminate small scale features. Accordingly, the smoothing filter $\{\cdot\}$ is defined to pass these M functions and reject all others. The estimate of the large scale component $\{\hat{d}(\mathbf{x})\}$ is found by minimizing the mean squared error associated with the large scale signal

$$\{e^2(\mathbf{x})\} = \langle [\{d(\mathbf{x})\} - \{\hat{d}(\mathbf{x})\}]^2 \rangle \tag{2.2}$$

subject to the zero bias constraint

$$\langle \{d(\mathbf{x})\} - \{\hat{d}(\mathbf{x})\} \rangle = 0 \quad . \tag{2.3}$$

Here $\langle \cdot \rangle$ is an average over an ensemble of realizations of the field d, in which the small scale component fluctuates but the large scale signal does not necessarily vary. In the ensemble average the small scale anomalies, which are assumed to be statistically homogeneous, and the noise term must both have zero mean and must be uncorrelated with each other, so that

$$\langle d'(\mathbf{x}) \rangle = 0 \,, \qquad \langle \varepsilon_d(\mathbf{x}) \rangle = 0 \,, \qquad \langle d'(\mathbf{x}) \varepsilon_d(\mathbf{x}) \rangle = 0 \qquad \text{for any } \mathbf{x} \quad . \tag{2.4}$$

These conditions ensure that the averaging operator acts identically to the smoothing operator in removing the small scale signal and isolating the large scale component.

Throughout the remaining discussion, matrix notation will be used in order to succinctly present the computations in an approach that can be easily implemented in common programming languages. Accordingly, $\tilde{\mathbf{d}}_n$ denotes the vector of observations $[\tilde{d}(\mathbf{x}_1)\cdots\tilde{d}(\mathbf{x}_N)]^{\mathrm{T}}$, where $[\cdot]^{\mathrm{T}}$ indicates the transpose.

Given a set of R locations $\mathbf{x}_r(r=1,\cdots,R)$, the estimates of the large scale signal at those locations $\{\hat{\mathbf{d}}\}_r = [\{\hat{d}(\mathbf{x}_1)\}\cdots\{\hat{d}(\mathbf{x}_R)\}]^{\mathrm{T}}$ are formed from a linear combination of the large scale basis functions evaluated at $\mathbf{x}_r$,

$$\{\hat{\mathbf{d}}\}_r = \mathbf{F}_{rm}\mathbf{b}_m \quad . \tag{2.5}$$

Here $\mathbf{b}_m$ is a vector of weights, and $\mathbf{F}_{rm}$ is the matrix of the M basis functions evaluated at the R mapping locations, with elements $F_{ij} = F_j(\mathbf{x}_i)(i=1,\cdots,R; j=1,\cdots,M)$. To determine the weights the mean squared error (2.2) is minimized subject to the constraint (2.3) using Lagrange multipliers, which yields

$$\mathbf{b}_m = (\mathbf{F}_{nm}^{\mathrm{T}}\mathbf{A}_{nn}^{-1}\mathbf{F}_{nm})^{-1}\mathbf{F}_{nm}^{\mathrm{T}}\mathbf{A}_{nn}^{-1}\tilde{\mathbf{d}}_n \quad , \tag{2.6}$$

where $[\cdot]^{-1}$ indicates the matrix inverse. In this expression, $\mathbf{F}_{nm}$ is the matrix of the M basis functions evaluated at the N data locations, and $\mathbf{A}_{nn}$ is the $N\times N$ matrix containing the small scale covariances for all pairs of data. The small scale anomalies $\tilde{\mathbf{d}}'_n$ are defined as $\tilde{\mathbf{d}}_n - \{\mathbf{d}\}_n = \mathbf{d}'_n + \boldsymbol{\varepsilon}_d$, which gives

$$\mathbf{A}_{nn} = \langle\tilde{\mathbf{d}}'_n\tilde{\mathbf{d}}'^{\mathrm{T}}_n\rangle = \langle\mathbf{d}'_n\mathbf{d}'^{\mathrm{T}}_n\rangle + \langle\boldsymbol{\varepsilon}_d\boldsymbol{\varepsilon}_d\rangle \quad . \tag{2.7}$$

The noise covariance matrix $\langle\boldsymbol{\varepsilon}_d\boldsymbol{\varepsilon}_d\rangle$ is simply a constant E multiplied by the $N\times N$ identity matrix $\mathbf{I}_{nn}$.

The covariance of the small scale signal is used to determine both the large scale component, as evidenced by (2.5)-(2.7), and the small scale field, as described below. To be computationally feasible, the covariance must be modeled analytically as a function D of the separation between two points,

$$D(\Delta\mathbf{x}) = \langle d'(\mathbf{x}_i)d'(\mathbf{x}_j)\rangle \quad , \tag{2.8}$$

where $\Delta\mathbf{x} = \mathbf{x}_j - \mathbf{x}_i$. Typically the user selects a particular function, such as a Gaussian, and values for the decorrelation length scale and variance. Often these choices are somewhat subjective. In contrast, the optimal analysis technique described here uses an IGLS procedure to objectively determine the analytic covariance function directly from the data. IGLS has been well documented in the statistical literature (e.g., Goldstein, 1986; del Pino, 1989; Goldstein, 2011) and has been employed in a wide variety of fields including economics, sociology, medicine, and geology. If the data are multivariate normal, the IGLS result is equivalent to the maximum likelihood estimate (Goldstein, 1986).

The IGLS procedure implemented in the present method consists of three basic steps: 1) make an initial estimate of the large scale signal and compute the associated small scale anomalies; 2) using those anomalies determine the covariance function of the small scale signal; 3) using that covariance function, make a new estimate of the large scale signal and calculate the associated small scale anomalies. The second and third steps are then iterated until the covariance function converges.

In the first step, the large scale signal is estimated by fitting the data to the functions F_m assuming that the small scale anomalies are uncorrelated, i.e., $\mathbf{A}_{nn} = E\mathbf{I}_{nn}$. With this stipulation, the problem reduces to an ordinary least squares fit. Accordingly the large scale field is determined using (2.5) with initial weights $\mathbf{b}_m^{(0)}$ given by

$$\mathbf{b}_m^{(0)} = (\mathbf{F}_{nm}^{\mathrm{T}}\mathbf{F}_{nm})^{-1}\mathbf{F}_{nm}^{\mathrm{T}}\tilde{\mathbf{d}}_n \quad . \tag{2.9}$$

The small scale anomalies are then calculated as the difference between the observations and the initial estimate of the large scale field at the data locations,

$$\tilde{\mathbf{d}}_n^{\prime(0)} = \tilde{\mathbf{d}}_n - \{\hat{\mathbf{d}}\}_n^{(0)} = \tilde{\mathbf{d}}_n - \mathbf{F}_{nm}\,\mathbf{b}_m^{(0)} \quad . \tag{2.10}$$

In the second step, the anomalies $\tilde{\mathbf{d}}_n^{\prime(k)}$ are used to estimate the analytic covariance function $D^{(k)}(\Delta\mathbf{x})$ (where k indicates the iteration number). To accomplish this, the empirical covariance can be directly calculated from all pairwise products of the

anomalies, as in (2.8), and then an analytic function can be fit to the result. Alternatively, the semivariogram (also called the structure function in Bretherton et al. (1976)) can be used to determine the covariance function. The semivariogram $\gamma(\Delta\mathbf{x})$, defined as half the average squared difference between points separated by a distance $\Delta\mathbf{x}$, is calculated empirically according to

$$\hat{\gamma}(\Delta\mathbf{x}) = \frac{1}{2|N(\Delta\mathbf{x})|} \sum_{N(\Delta\mathbf{x})} [d'(\mathbf{x}_i) - d'(\mathbf{x}_j)]^2 \quad . \tag{2.11}$$

In this expression, $N(\Delta\mathbf{x})$ is the set of all pairwise points such that $\mathbf{x}_j - \mathbf{x}_i = \Delta\mathbf{x}$, and $|N(\Delta\mathbf{x})|$ is the number of distinct pairs in $N(\Delta\mathbf{x})$. In practice, the distances are partitioned into bins of a given size, and then $N(\Delta\mathbf{x})$ and the average separation distance for each bin are determined accordingly. Once the empirical semivariogram has been computed the result is fit to an appropriate analytic function, typically via weighted least squares. The covariance function is subsequently derived from the analytic semivariogram using

$$D(\Delta\mathbf{x}) = \sigma^2 - \gamma(\Delta\mathbf{x}) \quad , \tag{2.12}$$

with the variance σ^2 calculated as $\lim_{\Delta\mathbf{x}\to\infty} \gamma(\Delta\mathbf{x})$.

When determining a covariance function from data, computing the semivariogram instead of directly calculating the covariance has several advantages . The empirical semivariogram tends to be smoother than the empirical covariance function and is thus better suited for fitting an analytic function. In addition, because the semivariogram is formed from differences between data pairs, it is not affected by unknown trends, unlike the covariance which depends on products of data pairs. An extensive literature describes the semivariogram, its statistical properties, and its estimation; see Cressie (1993) or Chiles and Delfiner (1999) for more details.

In the third step, the fitted analytic function $D^{(k)}(\Delta\mathbf{x})$ is used to make a new estimate of the large scale signal. The matrix $\mathbf{A}_{nn}$ is first calculated from $D^{(k)}(\Delta\mathbf{x})$ according to (2.7). Using that value of $\mathbf{A}_{nn}$, the weights $\mathbf{b}_m^{(k+1)}$ are computed from

(2.6) and subsequently used in (2.5) to determine the large scale estimate $\{\hat{\mathbf{d}}\}_r^{(k+1)}$. New small scale anomalies $\tilde{\mathbf{d}}_n^{'(k+1)}$ are subsequently calculated using an expression analogous to (2.10). The process of determining the covariance function and then estimating the large scale field and small scale anomalies is repeated until the covariance function converges, i.e., $|D^{(k+1)}(\Delta\mathbf{x}) - D^{(k)}(\Delta\mathbf{x})| \leq \delta$, where δ is the chosen tolerance level.

Convergence of the IGLS procedure results in an optimal estimate for the small scale covariance function $D(\Delta\mathbf{x})$, together with the corresponding large scale signal $\{\hat{\mathbf{d}}\}_r$ and small scale anomalies $\tilde{\mathbf{d}}_n^{'}$. Next, conventional objective analysis (Bretherton et al., 1976) is used to determine the small scale component of the field from $D(\Delta\mathbf{x})$ and $\tilde{\mathbf{d}}_n^{'}$. Specifically, the estimates of the small scale signal at the R mapping locations, $\hat{\mathbf{d}}_r^{'}$, are calculated from $\mathbf{A}_{nn}$ and the covariance between the small scale signal at the mapping locations $\mathbf{d}'_r$ and the small scale anomalies at the data locations $\tilde{\mathbf{d}}_n^{'}$ according to

$$\hat{\mathbf{d}}_r^{'} = \mathbf{C}_{rn}\mathbf{A}_{nn}^{-1}\tilde{\mathbf{d}}_n^{'} \quad , \tag{2.13}$$

where

$$\mathbf{C}_{rn} = \langle \mathbf{d}'_r \tilde{\mathbf{d}}'^{\mathrm{T}}_n \rangle = \langle \mathbf{d}'_r \mathbf{d}'^{\mathrm{T}}_n \rangle \quad . \tag{2.14}$$

Finally, the total estimates $\hat{\mathbf{d}}_r$ are given by $\{\hat{\mathbf{d}}\}_r + \hat{\mathbf{d}}'_r$. If the data are multivariate normal, the total estimates given by this method are identical to those produced by a maximum profile likelihood approach (Severini, 2000).

The mean squared errors associated with the total estimate, $\mathbf{e^2}_r$, are determined from

$$\mathbf{e^2}_r = \mathrm{diag}[\mathbf{\Sigma^2}_r - \mathbf{C}_{rn}\mathbf{A}_{nn}^{-1}\mathbf{C}_{rn}^{\mathrm{T}} + (\mathbf{F}_{rm} - \mathbf{C}_{rn}\mathbf{A}_{nn}^{-1}\mathbf{F}_{nm})(\mathbf{F}_{nm}^{\mathrm{T}}\mathbf{A}_{nn}^{-1}\mathbf{F}_{nm})^{-1}(\mathbf{F}_{rm} - \mathbf{C}_{rn}\mathbf{A}_{nn}^{-1}\mathbf{F}_{nm})^{\mathrm{T}}], \tag{2.15}$$

where $\mathbf{\Sigma^2}_r$ is an $R \times R$ matrix with the variances at the mapping locations, $\sigma^2(\mathbf{x}_r)$, on the diagonal. The first two terms in (2.15) are the mean squared errors associated with standard objective analysis, while the last term gives the errors associated with

the large scale GLS fit as well as the errors in the small scale signal introduced by the uncertainty on the large scale field.

2.3 Spherical radial basis functions

As discussed in section 2.1, SRBFs provide an excellent choice for the large scale basis function F_m when the mapping domain is large enough that the spherical geometry of the Earth must be taken into consideration. Radial basis functions, whether on the sphere or in Euclidean spaces, have received a great deal of interest in recent decades in applied mathematics (Fasshauer and Schumaker, 1998; Buhmann, 2003, and references therein). In general, a SRBF can be defined as a univariate function of the form

$$F_m(\mathbf{x}) = \phi(s(\mathbf{x}, \mathbf{x_m})) \quad , \tag{2.16}$$

where s is the geodesic distance between a given location $\mathbf{x}$ and the center of the SRBF $\mathbf{x}_m$. Data are then fit by taking a linear combination of SRBFs, as in (2.5). The number of centers M, and thus the number of SRBFs F_m, determines the degree to which the data are interpolated exactly (for $M =$ the number of observations N) or fit approximately (for $M < N$).

For mapping oceanographic data on a large domain, one of the most attractive choices for ϕ is the spherical reciprocal multiquadric (also called the multiquadric biharmonic), which was first suggested by Hardy and Göpfert (1975) for mapping geophysical data. In addition to being infinitely differentiable, this function is strictly positive definite on the sphere. If the centers correspond to a subset of the data locations, this condition ensures that the matrix $\mathbf{F}_{nm}$ has full rank and thus the weights $\mathbf{b}_m$ given by (2.6) are unique (Fasshauer and Schumaker, 1998; Fasshauer, 2007). For data on the Earth's surface, the spherical reciprocal multiquadric is written as

$$\phi(s) = (1 + h^2 - 2h \cos \frac{s}{r_E})^{-1/2}, \quad 0 < h < 1 \quad . \tag{2.17}$$

In this expression, r_E is the Earth's radius and h is an adjustable "shape" parameter that determines the scale of ϕ. Selecting an appropriate value for h guarantees that the large scale basis functions have scales greater than a chosen cutoff, as required by the method discussed here. The value of h together with the number and location of the centers $\mathbf{x}_m$ governs not only the scale of the estimate but also the rank and condition of $\mathbf{F}_{nm}$. Therefore an appropriate balance among these factors must be found to ensure that the resulting least squares approximation is both well-posed and well-conditioned and also produces an estimate with the desired scales.

The specific number and locations of the centers are determined from the number and distribution of the observations. According to the results of Quak et al. (1993) and Sivakumar and Ward (1993) (as discussed in Fasshauer (2007)), for certain radial basis functions including reciprocal multiquadrics, least squares approximation is well-posed (i.e., $\mathbf{F}_{nm}$ has full rank) provided that two conditions are met. First, the centers should be fairly well distributed throughout the domain. Second, the data locations should be clustered around the centers sufficiently evenly, with the inter-cluster distances relatively large compared to the intra-cluster distances. Although these results were derived for radial basis functions on Euclidean spaces, similar results are expected to apply on the sphere (Fasshauer and Schumaker, 1998). In practice, a cluster analysis technique such as hierarchical clustering (Hartigan, 1975) can be used to partition the data locations into a specified number of clusters so that the intra-cluster distances are minimized and the inter-cluster distances are maximized. The appropriate measure of distance in this case is the geodesic distance. Then the centroid of each cluster, defined as the point that minimizes the sum of the distances between that location and all the data in the cluster, provides a center for each SRBF.

2.4 Application

2.4.1 Simulated data

The optimal analysis method presented in this study is first demonstrated by mapping data sampled from a series of simulated dynamic height fields. Combining a single large scale field with twelve different small scale realizations produced an ensemble of twelve fields on a 1000 by 2000 km Cartesian grid with 10 km resolution. The large scale signal consists of a smooth dome merged with a zonal jet centered at $y = 250$km, with the amplitude varying from 29.5 to 100 dyn cm (where 1 dyn cm = 10 m^2 s^{-2}). For the small scale signal, twelve isotropic, homogeneous, stationary Gaussian fields were generated using the algorithm of Kroese and Botev (2013). The covariance of the field $D(\Delta\mathbf{x})$ was specified to be

$$D(\Delta\mathbf{x}) = \sigma^2 \exp(-\frac{||\Delta\mathbf{x}||^2}{2L^2}) \quad , \tag{2.18}$$

where $||\cdot||$ denotes Euclidean distance. The decorrelation length scale L was set to 100 km and the signal variance σ^2 was set to 400 dyn cm^2. One of the resulting dynamic height fields is shown in Figure 2.1a.

To characterize how the performance of this technique depends on sample size, each realization of the field was sampled twenty different times at N randomly generated locations, where $N = (50, 100, 250, 500, 1000)$, to produce twenty data sets for each N. Randomly generated sampling locations were used instead of a gridded array to more closely resemble the sampling scheme of instruments such as floats and drifters. A random error taken from a normal distribution with zero mean and variance of 20 dyn cm^2 (5% of the small scale signal variance) was added to each sample.

The method described above was used to map each data set onto a grid with 10 km resolution. Because the data were given in Cartesian coordinates, the radial basis functions used in this case were reciprocal multiquadrics in two-dimensional Euclidean

space centered at $\mathbf{x}_m = (x_m, y_m)$,

$$F_m(\mathbf{x}) = (1 + h^2 \, ||\Delta \mathbf{x}_m||^2)^{-1/2} \quad , \tag{2.19}$$

where $\Delta \mathbf{x}_m = \mathbf{x} - \mathbf{x}_m$. The shape parameter h was chosen so that the e-folding scale of the functions F_m was 5 times the e-folding scale of the fitted small scale covariance function. The locations of the centers $\mathbf{x}_m$ were determined using a hierarchical clustering algorithm, with the number of centers equal to 5% of the number of samples in the data set.

Each data set consisted of $12N$ samples taken from different realizations, which can be thought of as instances of the field at different times. To account for this, the basic procedure was modified slightly following LeTraon (1990). Essentially, when the data are non-simultaneous the large scale field, now the low wavenumber and low frequency component, is computed using all the data, while the small scale signal for each of the different time periods is determined using only data from that particular time. If the data were collected at times $t_\tau (\tau = 1, \cdots, T)$, then the covariance matrix $\mathbf{A}_{nn}$ is constructed using all the data as

$$\mathbf{A}_{nn} = \begin{bmatrix} \mathbf{A}(t_1) & (0) & \cdots & (0) \\ (0) & \mathbf{A}(t_2) & \cdots & (0) \\ \vdots & \vdots & \ddots & \vdots \\ (0) & (0) & \cdots & \mathbf{A}(t_T) \end{bmatrix} \quad , \tag{2.20}$$

where each $\mathbf{A}(t_\tau)$ represents a submatrix of the form given by (2.7) containing only covariances between the data points from time t_τ. This is equivalent to setting the covariance between data taken at different times to zero,

$$\langle \tilde{d}'(\mathbf{x}_i, t_i) \tilde{d}'(\mathbf{x}_j, t_j) \rangle = \begin{cases} \langle \tilde{d}'(\mathbf{x}_i) \tilde{d}'(\mathbf{x}_j) \rangle, & \text{if } t_i = t_j \\ 0, & \text{if } t_i \neq t_j \end{cases} \quad . \tag{2.21}$$

Using this expression for $\mathbf{A}_{nn}$, the large scale signal is computed from (2.5) and (2.6), where now the vector of observations $\tilde{\mathbf{d}}_n$ is composed of all the data grouped

according to time. For each time t_τ, the small scale signal and mean squared error are then calculated using the same procedure given above in (2.13)-(2.15). For the non-simultaneous case, however, all elements of the matrix $\mathbf{C}_{rn}$ corresponding to data not taken at time t_τ must be set to zero, analogous to (2.21). Using both temporal and spatial information generally gives an improved separation of the large and small scale signals, as the two usually have different frequencies. Moreover, if enough data are available to allow for sufficient separation in time, the requirement that the two fields have distinct spatial scales becomes less stringent.

In mapping the simulated dynamic heights, the empirical semivariogram $\hat{\gamma}$ was computed from (2.11) using only simultaneous pairs of data and grouping the data pairs by separation distance $||\Delta\mathbf{x}||$ into 10 km bins. The resulting curve was then fit to a Gaussian semivariogram of the form

$$\gamma(||\Delta\mathbf{x}||) = E + \sigma^2[1 - \exp(-\frac{||\Delta\mathbf{x}||^2}{2L^2})] \tag{2.22}$$

to find the estimated signal variance $\hat{\sigma^2}$, decorrelation length scale $\hat{L}$, and noise variance $\hat{E}$. For each data set, the procedure was iterated until the covariance function converged, using a tolerance level δ of $10^{-5}\max(\gamma)$.

As an example of the results, Figure 2.1b gives the mapped estimate of the field shown in Figure 2.1a, for one data set with $N = 250$. The map of the difference between the two (Figure 2.1c) demonstrates that the mapped field reproduces the features of the true field quite well. For the sake of comparison, the same field was mapped using the same sample configuration and assuming a reasonable set of covariance parameters ($L = 250$ km and $\sigma^2 = 200$ dyn cm^2). From the resulting estimate (Figure 2.1d) and corresponding differences from the true field (Figure 2.1e), it is apparent that using the fitted covariance parameters produces a more accurate estimate than does using the assumed parameters. Of course, if the assumed covariance function is close to the actual covariance, then the estimate made with the fitted parameters will not be appreciably better and may even be worse if the data are

sparse. However, very often the accuracy of the assumed covariance function can not be ascertained a priori. IGLS is highly valuable in these cases because it provides an objective method for estimating the covariance directly from the data.

Unsurprisingly, the average fitted covariance parameters are found to depend on the number of samples N (Figure 2.2). For this example, the accuracy of the fitted parameters increases nonlinearly with N. In addition, the dependence on the specific sampling locations, as indicated by the standard deviation of the twenty sets of parameters, decreases as the number of samples increases. These results underscore the importance of a sufficiently large data set when using IGLS.

2.4.2 Model output

In the second application of this optimal analysis method, we map salinities taken from the output of the Hybrid Coordinate Ocean Model (HyCOM) (Bleck, 2002). The global model runs used here (experiments 90.2 and 90.3, using HyCOM 2.2) have surface forcing given by the Navy Operational Global Atmospheric Prediction System model and assimilate data from all available observational platforms. The horizontal resolution is $1/12^\circ$. For more details about the model and the specific runs used in this study, see `https://hycom.org/hycom/documentation`.

Daily 1000 m salinity fields from 2007 were sampled in randomly generated locations dispersed evenly throughout the South Atlantic, with approximately 24 samples taken per day. A random normally distributed error with standard deviation of 0.01 PSU was added to each sample. The resulting data set consisted of 8,814 samples.

These data were mapped using the non-simultaneous procedure described above in section 2.4.1. In this case, the data within each month were considered to be simultaneous even though they were sampled on different days. The large scale signal was computed using all of the data, and twelve different small scale fields were estimated, corresponding to each month of the year. Spherical reciprocal multiquadrics of the form given in (2.17) were used for the large scale basis functions, with the shape pa-

rameter h set to give an e-folding scale of 3000 km. The number of functions M was chosen to be 300, and the locations of the centers was determined using a hierarchical clustering technique (Hartigan, 1975). The data were mapped onto a $1^\circ \times 1^\circ$ grid.

A two-dimensional semivariogram, which depended separately on zonal and meridional separation distances, was used in order to permit anisotropic but symmetric covariance in the data. The pairwise squared differences were partitioned by both zonal and meridional separation distance into 25 km wide bins ranging from 0 to 3000 km and then averaged. The resulting empirical semivariogram was fit to an anisotropic Gaussian semivariogram with zonal and meridional decorrelation length scales, L_x and L_y,

$$\gamma(||\Delta\mathbf{x}||) = E + \sigma^2\{1 - \exp[-\frac{1}{2}(\frac{dx^2}{L_x^2} + \frac{dy^2}{L_y^2})]\} \quad , \tag{2.23}$$

using the weighted least squares method proposed by Cressie (1985). In that formulation, the weights $w(||\Delta\mathbf{x}||)$ are given by

$$w(||\Delta\mathbf{x}||) = \frac{|N(\Delta\mathbf{x})|}{2\gamma^2(||\Delta\mathbf{x}||)} \quad . \tag{2.24}$$

After five iterations the covariance estimation converged, using a tolerance of $10^{-3}\max(\gamma)$. At this depth, the covariance was found to be isotropic, with $\hat{L}_x = 84.0$ km and $\hat{L}_y = 85.4$ km, and the 95% confidence bounds given by [79.5 88.4] and [80.9 89.9] respectively. The standard deviation of the small scale signal $\hat{\sigma}$ was determined to be 0.03488 PSU with 95% confidence bounds equal to [0.03483 0.03493]. Figure 2.3 shows the mapped salinity field for the month of July together with the average of the daily HyCOM fields for the same month and the difference between the two. Although the mapped estimate misses some of the small scale features of the true field, especially in the energetic and highly variable Brazil-Malvinas Confluence, it performs well overall.

The twelve resulting maps were compared with the monthly averages of the HyCOM output linearly interpolated to the same grid as the mapped estimates. The root mean squared error (RMSE) was computed from the difference between the two

sets of fields. The same samples were also mapped using a variety of assumed length scales (50, 300, 500 and 750 km) and then the RMSE for each of the resulting sets of maps was calculated. The results of the IGLS procedure gave the minimum RMSE (Table 2.1), indicating that in this case the covariance function determined using IGLS produces more accurate fields than do any of the assumed covariance functions.

2.4.3 Argo data

Finally, to illustrate the use of this method with actual oceanographic observations, global absolute geostrophic velocities were estimated from data collected by the Argo array of profiling floats (Roemmich et al., 2004). The data set used here, the same as in Gray and Riser (2014), spans the period from December 2004 to November 2010. It consists of 485,457 temperature and salinity profiles of the upper 2000 decibars (dbar) and 442,211 estimates of velocity at 900 dbar computed from the trajectories of the floats. Details of the data set, including the quality control procedures, the protocol for estimating the deep velocity from the trajectory information, as well as the temporal and spatial distribution of the data, are found in Gray and Riser (2014).

Using this data set, absolute geostrophic velocities in the upper 2000 dbar were estimated for the period December 2004 to November 2010. The basic procedure used in Gray and Riser (2014) was implemented here as well. Essentially, dynamic heights referenced to 900 dbar were computed on 29 pressure levels using the temperature and salinity observations. These data were then mapped onto a $1^\circ \times 1^\circ$ grid with the optimal analysis technique described in this study. Relative velocities referenced to 900 dbar were also determined at each level from partial derivatives of dynamic height. Next, the estimates of reference velocity at 900 dbar and the corresponding geostrophic streamfunction were mapped onto the same grid. Lastly, simple addition of the relative and reference velocity fields produced absolute geostrophic velocities at each of the 29 pressure levels. Gray and Riser (2014) give a thorough description of all aspects of this method.

For all of these data, the optimal analysis method for non-simultaneous data outlined in section 2.4.1 was used to produce monthly maps. A large scale field was computed for each month of the year using all data from that month regardless of year, resulting in a large scale seasonal cycle. Small scale fields were then determined for each individual month of the study period. The same basic IGLS method used by Gray and Riser (2014) has been employed here as well, but the estimates have been recomputed with two slight improvements to the mapping technique. First, whereas Gray and Riser (2014) calculated the empirical covariance from products of data pairs and fit that to an isotropic analytical function, this study computes the empirical semivariogram and fits that to an anisotropic Gaussian of the form given in (2.23), following the procedure given in section 2.4.2. Using this type of function allows for the possibility of anisotropy in the data, instead of forcing the covariance to be isotropic. When mapping velocities, the anisotropic covariances and corresponding semivariograms between the components of the velocity vectors were determined from (2.23) following Gille (2003a). Second, 500 SRBFs, in the form of spherical reciprocal multiquadrics (2.17) with an e-folding scale of 3000 km, were used as the large scale basis functions in place of the spherical harmonics used in the previous work. The center locations were determined with a hierarchical clustering algorithm (Hartigan, 1975). This change resulted in an estimate with smaller uncertainties that is more reliable in areas with sparse data coverage.

As an example, the absolute geostrophic streamfunction at 200 dbar averaged over the study period along with the associated uncertainty is shown in Figure 2.4. The geostrophic flow at this level exhibits prominent anticyclonic subtropical gyres in all basins, a strong eastward flow in the Southern Ocean associated with the Antarctic Circumpolar Current, and cyclonic subpolar gyres in the North Pacific and North Atlantic. The updated estimates of Absolute Geostrophic Velocities from Argo (AGVA 2.0) are available at `http://flux.ocean.washington.edu/agva`.

In conclusion, the multiscale optimal analysis method described here provides an

efficient and objective way to estimate fields comprised of signals with varying spatial and temporal scales. Because the covariance of the small scale signal is estimated directly from the data, this technique is recommended when a priori knowledge of the statistics of the field is insufficient. In addition, the use of SRBFs in fitting the large scale signal offers a number of advantages compared to other choices of basis functions, especially for basin scale or global domains.

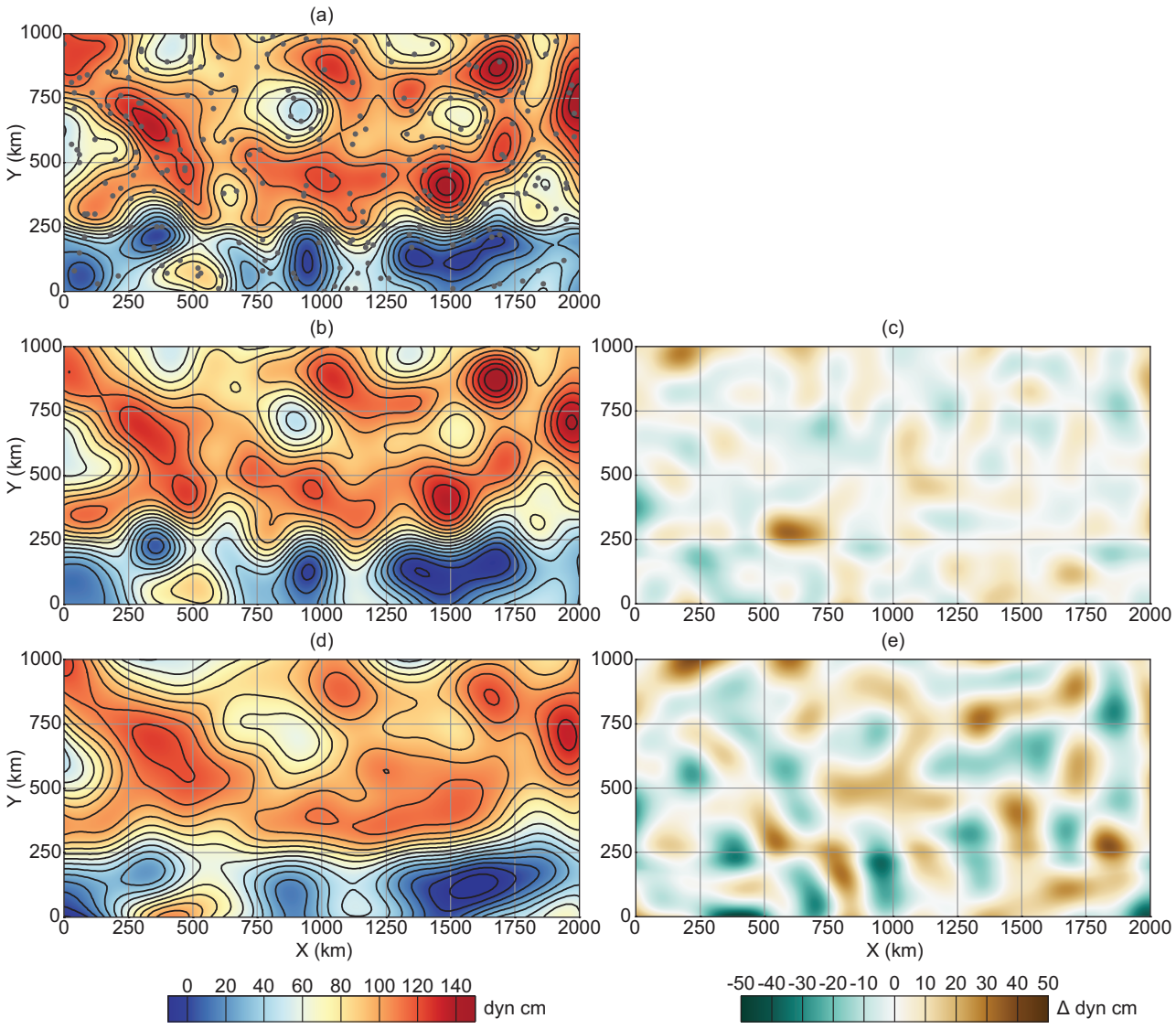

Figure 2.1: (a) One realization of simulated dynamic height field, with gray dots showing locations of the samples taken from this realization; (b) the same field mapped with covariance parameters determined using IGLS ($\sigma^2 = 405$ dyn cm^2, $L = 101.9$ km); (c) difference between (a) and (b); (d) the same field mapped with assumed covariance parameters ($\sigma^2 = 200$ dyn cm^2, $L = 250$ km); (e) difference between (a) and (d).

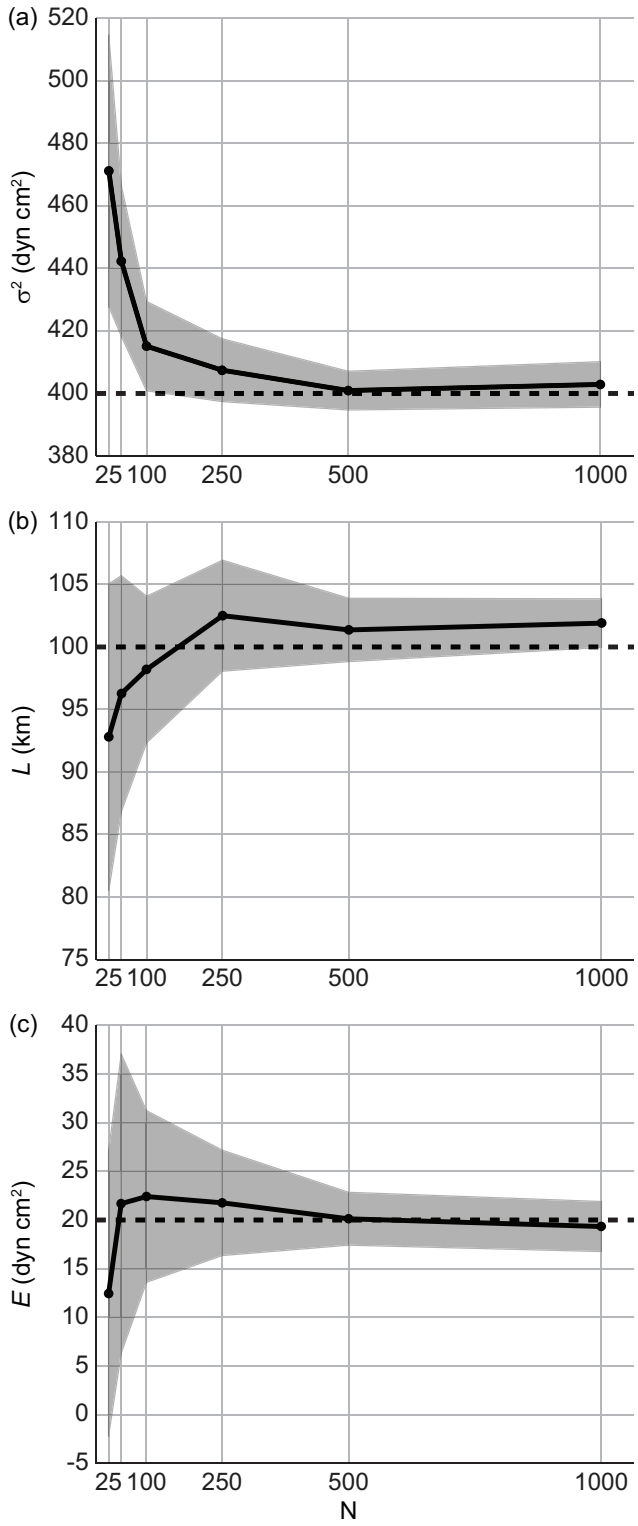

Figure 2.2: Fitted covariance parameters (solid line) for simulated dynamic height data, as a function of the number of samples N, and true covariance parameters (dashed line). Shaded area shows one standard deviation, based on 20 different sets of samples for each N. (a) Signal variance σ^2; (b) decorrelation length scale L; and (c) error variance E.

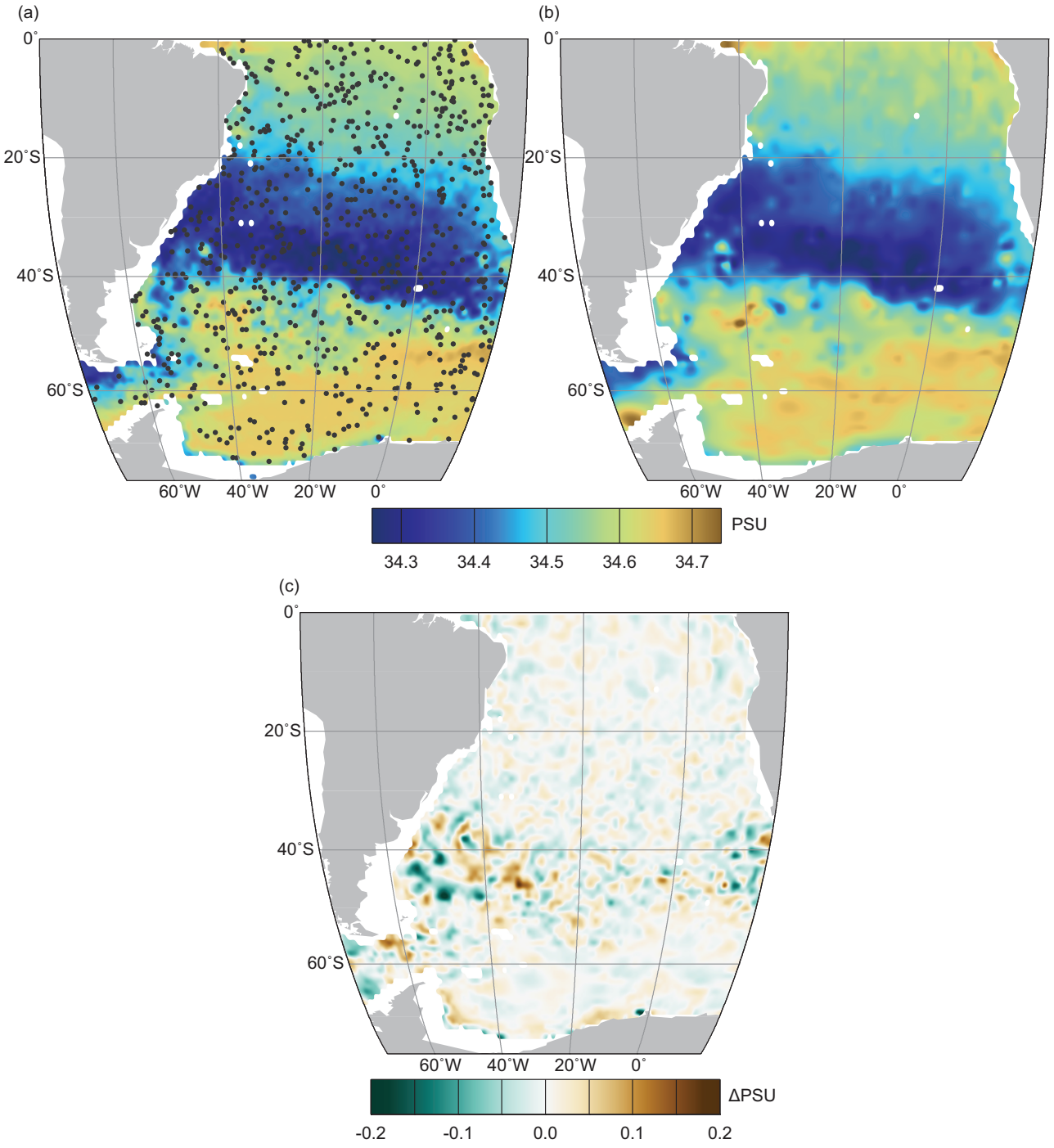

Figure 2.3: (a) Average July 2007 salinity at 1000 m from HyCOM with July sample locations shown by black dots; (b) mapped estimate of July 2007 salinity at 1000 m; (c) difference between (a) and (b).

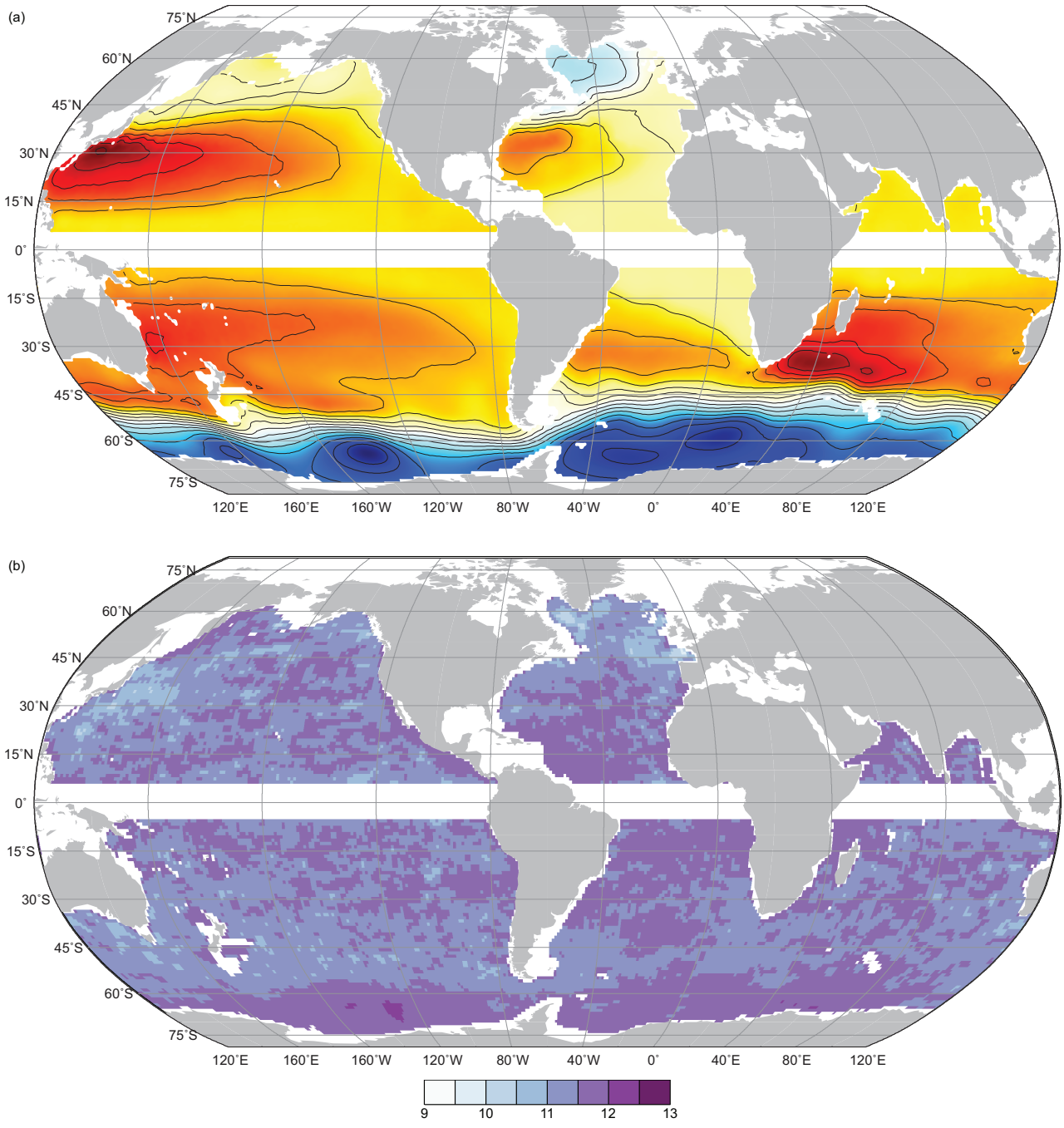

Figure 2.4: (a) Mean absolute geostrophic streamfunction at 200 dbar from Argo data for Dec 2004-Nov 2010. Contour interval is 10 dyn cm (1 dyn cm = 10 m^2 s^{-2}). Highs (lows) are shown in red (blue). (b) Uncertainty in the mean geostrophic velocity at 200 dbar, given as a percentage of the standard deviation of the mean geostrophic velocity.

Table 2.1: Root mean squared error (RMSE) between true monthly averaged salinity fields from HyCOM and mapped fields, as a function of covariance length scale.

Length scale (km)	RMSE (PSU)
Determined with IGLS	
$L_x = 84.0$, $L_y = 85.4$	0.0299
Assumed	
50	0.0300
300	0.0403
500	0.0329
750	0.0305

Chapter 3

A GLOBAL ANALYSIS OF SVERDRUP BALANCE USING ABSOLUTE GEOSTROPHIC VELOCITIES FROM ARGO[1]

Using observations from the Argo array of profiling floats, the large-scale circulation of the upper 2000 decibars (db) of the global ocean is computed for the period December 2004 to November 2010. The geostrophic velocity relative to a reference level of 900 db is estimated from temperature and salinity profiles, and the absolute geostrophic velocity at the reference level is estimated from the trajectory data provided by the floats. Combining the two gives absolute geostrophic velocities on 29 pressure surfaces spanning the upper 2000 db of the global ocean. These velocities, together with satellite observations of wind stress, are then used to evaluate Sverdrup balance, the simple canonical theory relating meridional geostrophic transport to wind forcing. Observed transports agree well with predictions based on the wind field over large areas, primarily in the tropics and subtropics. Elsewhere, especially at higher latitudes and in boundary regions, Sverdrup balance does not accurately describe meridional geostrophic transports, possibly due to increased importance of the barotropic flow, nonlinear dynamics, and topographic influence. Thus while it provides an effective framework for understanding the zeroth-order wind-driven circulation in much of the global ocean, Sverdrup balance should not be regarded as axiomatic.

---

[1]Published as Alison R. Gray and Stephen C. Riser, 2014: A global analysis of Sverdrup balance using absolute geostrophic velocities from Argo. *J. Phys. Oceanogr.*, 44, 1213–1229.

3.1 Introduction

The general circulation of the ocean plays a central role in the global transport of heat, freshwater, carbon, oxygen, nutrients, and other constituents. The ocean's large-scale circulation strongly influences the distribution of these important quantities and thus shapes both global climate and patterns of marine biological production. A fundamental zeroth-order theory of the large-scale circulation, Sverdrup balance (Sverdrup, 1947) directly relates meridional geostrophic transport to wind stress. Despite its key role in our understanding of ocean dynamics, the extent to which this tenet quantitatively describes observed global ocean circulation has received surprisingly little investigation.

One of the most likely causes for the lack of analyses of Sverdrup balance is the dearth of subsurface velocity observations. Subsurface measurements have traditionally been limited in both space and time because of the resource-intensive nature of shipboard observations and the sheer magnitude of the world's oceans. In his seminal series, Reid (1989, 1994, 1997, 2003) compiled over six decades of hydrographic and tracer data to estimate the mean geostrophic circulation of the Atlantic, Pacific, and Indian Oceans. His analysis relied on somewhat subjective choices for constraints on the total transport and reference velocities and also assumed that both the flow and mixing take place along isopycnal surfaces. Several other studies (Macdonald and Wunsch, 1996; Macdonald, 1998; Ganachaud and Wunsch, 2000; Ganachaud, 2003) have used hydrographic sections from the World Ocean Circulation Experiment (WOCE) in conjunction with inverse box models to produce quantitative estimates of global ocean circulation. Such estimates, however, are sensitive to particular assumptions concerning the accuracy of the conservation equations used to constrain the flow. Although these analyses represent considerable progress in our ability to determine subsurface geostrophic flow, the spatial and temporal coverage of the data used in these estimates remains relatively narrow.

In contrast, the Argo array of more than 3,000 autonomous profiling floats (Roemmich et al., 2004) offers an abundance of hydrographic and velocity observations with unprecedented resolution in both space and time. These instruments provide velocity estimates and measure temperature and salinity in the upper 2000 db of the ocean, relaying the data to shore-based data centers in real time. Argo floats have been deployed throughout the global ocean with a nominal horizontal spacing of 300 km. Each float collects hydrographic profiles at regular intervals, typically ten days. In this study, absolute geostrophic velocities are determined by combining these hydrographic profiles with the direct estimates of velocity provided by the float trajectories. The resulting quantitative estimate of the large-scale circulation has significant advantages, including vastly improved spatial and temporal data coverage and no *ad hoc* assumption regarding the reference velocity.

The goals of this work are to (1) compute the absolute geostrophic velocity in the upper 2000 db of the global ocean during the period 1 December 2004 to 30 November 2010 using observations from the Argo array of profiling floats and (2) use the resulting velocity estimate, together with satellite observations of wind stress, to examine the validity of Sverdrup balance on a global point-by-point basis. Given that this highly-simplified theory of wind-driven circulation is not expected to correspond exactly to the observed ocean everywhere, determining if and when it quantitatively predicts geostrophic circulation is valuable. Investigating where Sverdrup balance succeeds and where it fails, and understanding why, will also help further our knowledge of the dynamics that dominate different ocean regimes. Section 3.2 gives a brief derivation of Sverdrup balance and reviews relevant results from previous work. The data and methods used to compute the gridded velocities and evaluate Sverdrup balance are discussed in sections 3.3 and 3.4, respectively. Section 3.5 presents the absolute geostrophic velocity fields followed by an analysis of the validity of Sverdrup balance and the implications of these findings. Lastly, section 3.6 reviews the conclusions of this study.

3.2 Background

Since Sverdrup (1947) first outlined the elegant formulation of the wind-driven circulation now known as Sverdrup balance (hereafter SB), it has become a canonical part of circulation theory. The derivation of SB is based on the linear vorticity equation connecting meridional geostrophic velocity v_g to the vertical gradient of vertical velocity w,

$$\beta v_g = f\frac{\partial w}{\partial z} \quad . \tag{3.1}$$

Following standard notation f is the Coriolis parameter and β its meridional gradient. The validity of (3.1) requires steady flow as well as small Rossby and Ekman numbers. Integrating vertically from a depth $z = h$ to the base of the Ekman layer (denoted as $z = 0$) gives

$$\int_h^0 \beta v_g \, dz = \beta V_g = f[w(z=0) - w(z=h)] \quad , \tag{3.2}$$

where V_g is the meridional component of the geostrophic transport. Basic Ekman theory provides that the vertical velocity at the base of the Ekman layer is related to the wind stress vector $\boldsymbol{\tau} = (\tau^x, \tau^y)$ through

$$w(z=0) = w_E = \mathbf{k} \cdot \nabla \times (\frac{\boldsymbol{\tau}}{\rho f}) \quad , \tag{3.3}$$

where ρ is density. Next we make the critical assumption that $w(z = h) = 0$. Given this, (3.2) and (3.3) can be combined to produce

$$V_g = \frac{f}{\beta}\mathbf{k} \cdot \nabla \times (\frac{\boldsymbol{\tau}}{\rho f}) \quad . \tag{3.4}$$

Expanding the right-hand side of (3.4) gives a useful partition in terms of the meridional component of Ekman transport V_E and what is commonly thought of as the Sverdrup transport V_{Sv},

$$V_g = V_{Sv} - V_E = (\frac{1}{\rho\beta}\mathbf{k} \cdot \nabla \times \boldsymbol{\tau}) - (\frac{-\tau^x}{\rho f}) \quad . \tag{3.5}$$

This statement of SB separates V_g from the wind-derived transport $V_{Sv} - V_E$, while also showing that the total meridional transport $V = V_g + V_E$ equals V_{Sv}. The form

of SB provided by (3.5) is directly tested in this study, using observations provided by the Argo array.

Relatively few studies have attempted to assess the validity of SB using observational data, and those that have are mostly limited to fairly narrow regions. Leetmaa et al. (1977) first explored a zonally-integrated form of SB in the North Atlantic. Using a hydrographic transect across 25°N and assuming a level of no motion, they found that the zonally-integrated southward transport was consistent with SB. Wunsch and Roemmich (1985), however, identified several issues with this study that called this conclusion into question. These included the extrapolation of a level of no motion through the Gulf Stream recirculation, contrary to the evidence there; inconsistency with the meridional heat transport needed to produce a substantial quantity of deep water at high latitudes; and a contradiction between the sign of the bottom w obtained by integrating (3.1) downward from a surface Ekman pumping velocity and the bottom w expected based on continuity and the slope of the seafloor. At the same latitude, Schmitz et al. (1992) subsequently concluded that the simple balance between southward interior geostrophic transport and northward Gulf Stream transport assumed in the Leetmaa study was not supported by water mass characteristics.

In the North Pacific, Qiu and Joyce (1992) determined that interannual variations in Sverdrup transport were strongly correlated with the transport of the Kuroshio and the North Equatorial Currents. Hautala et al. (1994) found good agreement between the zonally-integrated meridional geostrophic transport inferred from a hydrographic section across 24°N and that computed from wind data according to SB. Using altimetric data, Vivier et al. (1999) examined a time-dependent topographic SB, in which the integral in (3.2) is computed from the seafloor at $z = H$ to the sea surface and $w(z = H)$ is given by continuity ($w(z = H) = \mathbf{u} \cdot \nabla H$). They found that this version of SB explained variations in sea surface height in much of the North Pacific and the subtropical South Pacific.

More recently, Wunsch (2011) carried out a global quantitative analysis of SB

using the ocean state estimate produced by the ECCO-GODAE project from general circulation models least-squares fit to global-scale data sets available after 1992. On a point-by-point basis, the form of SB given by (3.2) was tested by integrating the meridional velocity, averaged over 16 years, from the depth where $|w| < 10^{-8}$ m s^{-1} to the surface. This transport was then compared to $f/\beta\ w(z = -117$ m), where $w(z = -117$ m) was assumed to be the Ekman pumping velocity. Using that formulation, SB was found to be reasonably accurate over much of the interior subtropical and tropical oceans. In this study, we provide another global assessment of the validity of SB, based solely on data obtained as part of the ongoing Argo program together with satellite wind stress observations.

3.3 Data

3.3.1 Oceanographic data

The oceanographic data in this study were collected by the Argo array of autonomous profiling floats and consist of upper ocean profiles of temperature T and salinity S as a function of pressure p, along with float trajectories determined by satellite positioning. The Argo array is comprised of several different types of quasi-Lagrangian profiling floats. While the individual float types vary in terms of their specific components, all floats used here were equipped with a buoyancy engine, a satellite antenna for positioning and transmission, and an instrument package containing a conductivity-temperature-depth (CTD) sensor. To ensure high quality, nearly all of the data included in our study (99.9% of the total profiles) were collected by floats with SeaBird CTDs, with the remaining small quantity of data from a selected subset of floats with FSI CTD sensors.

Each float repeatedly executed a mission cycle that consisted of four phases: (1) descent to the predefined "parking pressure" p_{park}; (2) subsurface drift at p_{park} for a predetermined length of time; (3) ascent to the surface with concurrent measurements

of T, S, and p; and (4) surface drift with transmission of the hydrographic data and position fixes to a satellite. The data transmitted from the floats were compiled at two onshore Global Data Assembly Centers (GDACs) and were made publicly available usually within 24 hours. More details regarding the technical aspects and operation of the floats as well as the processing of the data are given by Roemmich et al. (2004) and the Coriolis GDAC at IFREMER, France (`www.coriolis.eu.org/cdc/argo.htm`).

All data used in this study were obtained from the Coriolis GDAC. Only data that had undergone thorough quality control testing and were designated as *delayed-mode* were included. In addition, data from floats with known problems (i.e., those on the "graylist" compiled by the GDACs) were discarded. Data from marginal seas, such as the Gulf of Mexico and the Indonesian Seas, were also excluded. The time period for this analysis spanned 1 December 2004 to 30 November 2010. Prior to this time period, global Argo data coverage was sparse, and complete global delayed-mode data were not available for later years at the time of preparation.

Profiles

A total of 485,704 T and S profiles from 5,027 Argo floats were used in this study. The profiles had variable vertical resolution, with observations typically at 5 or 10 db increments near the surface and gradually increasing to 100 db increments below 1500 db. Only profiles extending to 870 db or deeper were included in this data set. The data are for the most part evenly-distributed in space (Figure 3.1a), although the edges of the basins are not as well-covered as the interior. The temporal distribution of the data is skewed towards the later part of the study period (Figure 3.1b) because the Argo array did not reach full coverage until early 2007.

At each profile location, T, S, and p were used to compute (1) a profile of dynamic height D as a function of p; (2) profiles of potential temperature θ, S, and p as a function of potential density σ_θ; and (3) maximum p, average θ, and average S of the mixed layer. To determine D, specific volume anomalies $\delta(S,T,p) = 1/\rho\,(S,T,p) -$

$1/\rho\,(35, 0, p)$ were calculated and then integrated with respect to pressure according to

$$D\,(p) = \int_{p_0}^{p} \delta \,\mathrm{d}p \quad . \tag{3.6}$$

The reference pressure p_0 was set to 900 db to allow easy combination with the velocity data derived from the float trajectories. D was computed at 29 regular pressure levels spanning the upper 2000 db. Extrapolation of the D profile beyond the pressure range of the original T and S profiles was limited to less than 28 db at the bottom of the profile and less than 4 db at the top.

The integral in (3.6) was calculated by interpolating the δ profile with a piece-wise polynomial composed of cubic Hermite basis functions (Fritsch and Carlson, 1980) and then analytically integrating the interpolant. This form of interpolating polynomial was chosen because it efficiently produces a smooth function that is monotonic on each interval and is therefore shape-preserving with no superfluous "bumps" or "wiggles". The resulting interpolated profiles were visually appealing and had minimal introduced density inversions. To further ensure the quality of the profile data, we manually inspected all interpolated profiles. Profiles that contained gaps of more than 400 db, density inversions ≥ 0.02 kg m^{-3} db^{-1}, or unrealistic interpolations (as determined by comparison to nearby profiles) were either corrected by removing a portion of the data or discarded entirely if correction was not possible.

The deepest p of the mixed layer along with the average mixed layer θ and S were computed for each profile using the density algorithm of Holte and Talley (2009). Profiles for which the algorithm failed to produce a mixed layer p, such as those that did not include any $p < 20$ db, were excluded, resulting in a dataset of 476,319 mixed layer data points. σ_θ was computed for each profile, and then θ, S, and p were interpolated onto regular σ_θ levels, again using a piecewise cubic Hermite polynomial without extrapolation. To span the full range of the Argo profiles used here, the σ_θ levels ranged from 22.4 to 27.95 kg m^{-3} and were linearly spaced with decreasing intervals from 0.25 to 0.01 kg m^{-3}.

Trajectories

Trajectory data for each float were used to estimate the drift velocity at the parking pressure $\mathbf{u}(p_{park})$ for each cycle. Only floats with a nominal $p_{park} \geq 800$ db were included in this study. Drift velocities were computed from the time the float began its descent t_{des} and the time it reached the surface at the end of the subsequent ascent t_{asc}, together with the corresponding diving location $\mathbf{x}_{des}$ and surfacing location $\mathbf{x}_{asc}$,

$$\mathbf{u}(p_{park}) = \frac{\mathbf{x}_{asc} - \mathbf{x}_{div}}{t_{asc} - t_{des}} \quad .$$

The t and $\mathbf{x}$ of the velocity estimate were taken as the average of t_{asc} and t_{des} and the average of $\mathbf{x}_{asc}$ and $\mathbf{x}_{des}$, respectively. This analysis only used subsurface drifts for which 5 days $\leq (t_{asc} - t_{des}) \leq 25$ days. Shorter cycles do not adequately measure geostrophic velocity due to a stronger influence from high frequency fluctuations, while longer cycles result in excessive smoothing in space and time.

For each cycle along the float trajectory, $\mathbf{x}_{des}$ and $\mathbf{x}_{asc}$ were determined with one of two methods depending on the type of satellite positioning system used by the float, the Argos System (96.6% of the data used here) or Global Positioning System (GPS, 3.4%). For Argos floats, which remain at the surface for 6-12 hours while obtaining multiple position fixes of varying accuracy, the procedure followed that detailed by Park et al. (2005). Both $\mathbf{x}_{asc}$ and $\mathbf{x}_{des}$ are generally unknown because a variable amount of time elapses between t_{asc} and the first position fix and between the last position fix and t_{des}. The float experiences much stronger currents at the surface than at p_{park}, and thus the accuracy of $\mathbf{u}(p_{park})$ is greatly improved if $\mathbf{x}_{asc}$ and $\mathbf{x}_{des}$ are estimated taking into account the surface drift and the elapsed time (Park et al., 2005). To accomplish this, t_{des} and t_{asc} are needed. These times were either obtained directly from the GDAC when available or estimated from the float meta-data and/or surface fixes using the protocols given in Park et al. (2005). When it was not possible to calculate t_{asc} and t_{des} from the available data for a particular cycle (37.6% of the data), they were approximated by computing the average Δt between t_{asc} and the

first surface fix and the average Δt between t_{des} and the last surface fix for all other cycles of the float and then adding these to the first and last fixes, respectively. In the small number of cases where we were unable to estimate t_{asc} and/or t_{des} by any of these means (3.8%), the times of the first and last surfaces fixes were used instead.

Next $\mathbf{x}_{asc}$ and $\mathbf{x}_{des}$ were estimated via a least-squares fit of the surface fixes from each cycle to a theoretical trajectory $\mathbf{x}(t)$, derived from a linear velocity $\mathbf{U_L}$ and an inertial oscillation of magnitude U_I and phase ϕ,

$$\mathbf{x}(t) = \mathbf{x}(t_0) + \mathbf{U_L} \times (t - t_0) + \int_{t_0}^{t} U_I \sin(f\tau + \phi)\ d\tau \quad ,$$

where t_0 is the time of the first fix. Each surface fix was weighted by $1/\epsilon^2$, where ϵ is the standard deviation of the fix (150, 350, and 1000 m for Argos fixes of level 3, 2, and 1 respectively). The fitted trajectory was then extrapolated to t_{des} and t_{asc} to give $\mathbf{x}_{des}$ and $\mathbf{x}_{asc}$. Park et al. (2005) showed that this method produces velocities that are more accurate and less biased than simple linear extrapolation of the surface fixes. The total uncertainty of each velocity estimate computed in this manner is on the order of 0.2 cm s^{-1} (Park et al., 2005).

Floats using GPS positioning obtain a single surface fix with much higher accuracy (10 m) and remain on the surface for a significantly shorter period of time (typically < 30 minutes). In these cases, $\mathbf{x}_{asc}$ and $\mathbf{x}_{des}$ for each cycle were both taken as the sole position fix, and t_{des} and t_{asc} set to the corresponding time.

The mean of the p measurements recorded along the drift track gave the measured p_{park} for each cycle. If no *in situ* p values were reported, p_{park} was assumed to be the preprogrammed nominal p_{park}. Only cycles for which 780 db $\leq p_{park} \leq$ 2020 db were included in this data set. Data were manually inspected if the difference between the nominal p_{park} and the measured p_{park} exceeded 100 db. When it appeared that the float had shoaled, the pressure sensor had failed, or the float had come into contact with the seafloor (as determined by comparing the float trajectory with available

bathymetric maps), the affected data were discarded. Any cycles flagged by the GDACs for likely grounding of the float were also removed from the data set.

After estimating p_{park} and $\mathbf{u}(p_{park})$, any outlying velocity estimates more than 10 standard deviations from the mean over the whole data set were excluded from further analysis. To combine the velocity data with the dynamic height data, the $\mathbf{u}(p_{park})$ estimates were adjusted to the common reference pressure p_0 (900 db). The geostrophic shear between p_{park} and p_0 was calculated by interpolating the mapped D fields (described below in section 3.4) to the location of $\mathbf{u}(p_{park})$. $\mathbf{u}(p_0)$ was then computed by adding this shear to $\mathbf{u}(p_{park})$. Data for which the magnitude of the velocity adjustment was greater than 20 cm s^{-1} were eliminated from the data set. The discarded data were all located within 5° of the equator, where the assumption of geostrophy becomes unreliable as the Rossby number grows as $1/f$.

The resulting velocity data set, consisting of 442,211 estimates of $\mathbf{u}(p_0)$ from 4,799 floats, provides a representative sample of the geostrophic velocity at p_0. The distribution in space (not shown) and time (Figure 3.1b) is comparable to that of the profile data, although there are slightly fewer estimates due to differences in the quality and requirements of each data set.

3.3.2 Wind stress data

Wind stress data needed to compute the Sverdrup and Ekman transports in (3.5) were derived from observations from the NASA SeaWinds scatterometer onboard QuikSCAT. These data were obtained from the Centre de Recherche et d'Exploitation Satellitaire (CERSAT), at IFREMER, Plouzané (France). A gridded product was used that gave global monthly 10 m wind fields at 0.5° x 0.5° resolution, spanning August 1999 to October 2009. Wind stress magnitude and direction as well as wind stress curl were provided.

3.4 Methods

3.4.1 Geostrophic velocity

Using the Argo dynamic height and velocity data, monthly absolute geostrophic velocities in the Atlantic, Pacific, Indian, and Southern Oceans were computed on 29 pressure surfaces spanning the upper 2000 db for the period December 2004 to November 2010. The procedure consisted of three basic steps. First, the D data were gridded on each p surface to produce 1° x 1° maps of both D and velocity relative to p_0 $\mathbf{u}_{rel}$, which is derived from D according to

$$\mathbf{u}_{rel}\left(x,y,p\right)=\mathbf{u}\left(x,y,p\right)-\mathbf{u}\left(x,y,p_0\right)=\frac{1}{f}\mathbf{k}\times\nabla D\left(x,y,p\right). \tag{3.7}$$

Second, the $\mathbf{u}(p_0)$ estimates were mapped onto the same spatial and temporal grid. A geostrophic streamfunction ψ_0 was computed simultaneously, where ψ_0 is defined here as

$$\mathbf{u}\left(x,y,p_0\right)=\frac{1}{f}\mathbf{k}\times\nabla\psi_0\left(x,y,p_0\right) \quad . \tag{3.8}$$

Third, simple addition of the two fields gave monthly gridded absolute geostrophic velocities at each p level, as shown by summing (3.7) and (3.8). Similarly, the streamfunction for the absolute geostrophic flow $\psi(p)$ was found by combining ψ_0 and $D(p)$ at each level.

All mapping was carried out using a variation of the method put forth by LeTraon (1990). Essentially this technique maps a large-scale signal using the objective function fitting procedure developed by Davis (1985) and a small-scale signal using the conventional objective analysis described by Bretherton et al. (1976). The two signals are characterized by different scales in both space and time. This procedure has the advantage of requiring no *a priori* knowledge of the statistics of the large-scale field; however, the statistics of the small-scale signal must be specified. Rather than simply assuming a decorrelation length scale, as is typically done, the present study uses a novel iterative approach to determine the statistics of the small-scale signal directly

from the data. Full details of the mapping procedure including the iterative scheme are given in the Appendix. For all p levels, mapping was restricted to areas where the depth of the seafloor $H \geq 1000$ m, as determined from a box average of ETOPO1 bathymetric data (Amante and Eakins, 2009). Additional grid points were excluded for p levels > 1000 db if $p \geq H$.

Uncertainties in the gridded velocities arise from a number of sources including array bias, measurement errors, and sampling errors (Katsumata and Yoshinari, 2010). The mapping procedure used here has the distinct advantage of producing at each grid point a quantitative estimate of the mean squared error e^2. This error estimate combines the usual errors in the large- and small-scale signals with the error arising in the small-scale field due to uncertainty in the large-scale signal (LeTraon, 1990). The total error in the absolute velocity was given by the sum of the e^2 associated with the relative and reference velocity.

The gridded absolute velocities described here (Absolute Geostrophic Velocities from Argo), together with accompanying error estimates, are available for use by the oceanographic community and can be obtained from `http://flux.ocean.washington.edu/agva`.

3.4.2 Density

Assuming hydrostatic balance, volume transport can be written as the integral of velocity between two pressure surfaces p_1 and p_2 (with $p_1 < p_2$),

$$\mathbf{U} = \int_{p_1}^{p_2} \frac{\mathbf{u}}{g\rho} \, \mathrm{d}p \quad , \tag{3.9}$$

where g is acceleration due to gravity. Since this expression requires estimates of *in situ* ρ in addition to $\mathbf{u}$, monthly maps of θ, S, and p on σ_θ surfaces were produced using the iterative two-step mapping technique presented above. These quantities were mapped on σ_θ surfaces instead of p surfaces due to the significant spurious anomalies that are introduced by averaging θ and S on p surfaces (Lozier et al., 1994).

Mixed layer p, θ, and S were also mapped with the same method. The gridded θ, S, and p on σ_θ surfaces, together with the mixed layer maps, were used to compute monthly 1° x 1° maps of ρ and σ_θ as a function of p. Mean squared errors were also calculated for each mapped quantity. The gridded θ and S, vertically interpolated onto the same p levels as the **u** fields, are also available at the website listed above.

3.4.3 Sverdrup balance

To assess the extent to which SB accounts for global meridional geostrophic transport, the two sides of (3.5) were computed. There is some question as to what time period is appropriate for testing SB. In other words, does SB hold over synoptic time scales, or does it only apply when the wind stress and geostrophic velocities are averaged over a longer time scale? Sverdrup (1947) and most oceanographic textbooks imply that SB should emerge after averaging over a long interval but do not specify a particular length. Instead of averaging, some authors (e.g., Niller and Koblinksy, 1985; Vivier et al., 1999) chose to discuss a time-dependent SB. Similar to Wunsch (2011), this study will examine the longest averaging periods permitted with the data sets used here, namely 6 years for the Argo data and 10 years for the QuikSCAT data, with an overlap between the two of almost 5 years.

The wind-derived transport in (3.5) was calculated using the zonal wind stress and wind stress curl derived from QuikSCAT together with the mixed layer ρ computed from the mean mapped mixed layer θ and S. Monthly maps of wind-derived transport were produced for the entire QuikSCAT era (August 1999 to October 2009) and then interpolated onto the same 1° x 1° horizontal grid as the mapped Argo data. These were then averaged over the whole time period and over the period contemporaneous with the Argo data (December 2004 to October 2009).

To evaluate the geostrophic transport in (3.5), the mapped meridional geostrophic velocity v and ρ were used to compute the V_g according to (3.9). In practice the integration was carried out by first finding the mean over the study period (December

2004 to November 2010) of $v(p)$, $\theta(\sigma_\theta)$, $S(\sigma_\theta)$, $p(\sigma_\theta)$, and the mixed layer properties. The mean was also calculated for the period overlapping with the QuikSCAT data. Using these mean values, $\langle\rho(p)\rangle$ was constructed for each grid point (where the angle brackets denote the mean). Next $\langle v\rangle$ and $\langle\rho\rangle$ were interpolated to common p levels with piece-wise cubic Hermite polynomials. The resulting interpolants were used to calculate $\langle v\rangle/g\langle\rho\rangle$, which was then integrated analytically. While in principal $\langle v\rangle/g\langle\rho\rangle$ is not exactly equal to $\langle v/g\rho\rangle$, the difference here is considered negligible as $\langle 1/\rho\rangle \approx 1/\langle\rho\rangle$.

Of critical importance to any analysis of SB is the choice of h, the bottom boundary of the transport integral in (3.2). One approach is to inquire as to the expected depth of the wind-driven circulation. The ventilated thermocline theory of Luyten et al. (1983) suggests that the wind-driven transport extends to the densest outcropping isopycnal in a given basin. Rhines and Young (1982) identify the depth of potential vorticity homogenization as the base of the wind-driven circulation. Motivated by these considerations and the observations of Talley (1988), Hautala et al. (1994) selected the depth of 26.5 σ_θ and 27.0 σ_θ in the eastern and central subtropical North Pacific, respectively. Other authors have integrated velocity from the surface to a fixed depth (e.g., Leetmaa et al., 1977). The most straightforward idea, namely that h should be the depth where w goes to zero, arises directly from the derivation of SB. Although historical observations of w are generally unsuitable for practical application of this concept, the ocean state estimate used by Wunsch (2011) did allow h to be defined in this way.

Here, we have evaluated SB using two different methods of determining h. The first choice for h is the depth of the maximum isopycnal outcropping in wintertime along the line of zero average wind-stress curl, which was prompted by ventilated thermocline theory. In the second approach, instead of selecting an *a priori* value for h, at each grid point the depth and corresponding pressure were found that gave the best fit to SB. If the meridional geostrophic transport agrees with the transport

predicted by SB, then this depth should also be the location in the water column where w is approximately zero. Although the existence of such a depth does not by itself guarantee that SB is satisfied, this value will be used as a starting point for further analysis. In both cases, the mean maps of θ, S, p, and mixed layer properties were used to determine the desired limits of integration.

The uncertainty associated with the computed geostrophic transport was derived from the error estimates for v, θ, S, and p using a Monte Carlo simulation with 500 iterations. The standard error around the mean was calculated for each quantity using the uncertainties on the monthly maps. In each iteration, $\langle v \rangle$, $\langle \theta \rangle$, $\langle S \rangle$, $\langle p \rangle$, and the mean mixed layer properties were individually perturbed by an amount randomly drawn from a uniform distribution on the interval $(-e, e)$, and the transport was calculated as described above. The error in $\langle v \rangle$ was decomposed into the error associated with $\langle v(p_0) \rangle$ and that associated with $\langle v_{rel} \rangle$, and these were varied separately. At each grid point, the errors in each variable were assumed to be correlated vertically but independent of the errors in the other quantities. The variance of the resulting series of 500 transport values provided an uncertainty on the computed geostrophic transport.

3.5 Results and discussion

3.5.1 Absolute geostrophic velocities

We first present the mean absolute velocity fields at four representative pressure levels, 5 db, 200 db, 1000 db, and 1500 db (Figures 3.2-3.5). In each of these plots, $\psi(p)$ is contoured at the intervals specified in the captions. Colors indicate highs in $\psi(p)$ in red and lows in blue; as (3.8) shows, these represent anticyclonic and cyclonic flows respectively. All estimates at latitudes $\leq 5°$N/S are discarded since the geostrophic assumption becomes problematic in this region. In addition, results are only plotted where the uncertainty in the geostrophic velocity $e_{|\mathbf{u}|} < \sigma_{|\mathbf{u}|}/8$, where $\sigma_{|\mathbf{u}|}$ is the

standard deviation of **u**.

At the shallow, near-surface level (Figure 3.2), the dominant features are the anticyclonic subtropical gyres found in all basins except the North Indian, the eastward-flowing Antarctic Circumpolar Current (ACC) south of approximately 40°S, and the cyclonic subpolar gyres in the North Pacific and North Atlantic. Eastward flow is observed in the northern tropical Pacific and Atlantic, associated with the North Equatorial Counter Current in each basin. While the long-term mean flow in the North Indian Ocean is weak, an analysis of the annual cycle (not shown) reveals a strong seasonal signal likely associated with monsoonal forcing. At this p level, the geostrophic flow shown here makes up only a part of the total velocity field, with Ekman flow constituting a significant portion, especially at lower latitudes.

At 200 db (Figure 3.3), the subtropical gyres have all shifted poleward compared to their locations at 5 db. In the South Pacific, the subtropical gyre now has two distinct lobes, one to the east of New Zealand and one at about 25°S. Strong velocities are still found in the western boundary current regions and the ACC, while the circulation in the tropical regions is substantially weaker compared to the near-surface level.

In the mean flow at 1000 db (Figure 3.4), the North Pacific subtropical gyre has become smaller and weaker relative to the upper levels. A generally southward flow is observed in the North Atlantic subtropics. The subpolar gyres, while somewhat reduced in strength, continue to occupy the entire North Atlantic and North Pacific north of approximately 45°N. This observation agrees well with the fact that the flow at higher latitudes is known to be less baroclinic than the flow in the subtropics (Talley et al., 2011b). In the Southern Hemisphere, the subtropical gyres are shifted even further poleward, with a strong recirculation east of southern Africa associated with the Agulhas Retroflection. Anticyclonic flows south of Australia, in the Tasman Sea, and east of New Zealand appear connected, indicative of a supergyre structure (Ridgway and Dunn, 2007). The ACC continues to be quite vigorous at this pressure level, but elsewhere mean flow is relatively weak.

Lastly, the mean velocity field at 1500 db (Figure 3.5) is similar in structure to the flow at 1000 db but exhibits more small-scale features, probably influenced by the smaller signal-to-noise ratio here. The increased southward flow along the western edge of the North Atlantic is suggestive of a deep western boundary current. A relatively strong southward flow along the east coast of South America is also present. In the Southern Hemisphere the ACC dominates the flow at this level, with significant anticyclonic flows persisting east of southern Africa and New Zealand and in the Tasman Sea.

The results presented here are broadly consistent with modern ideas of the large-scale circulation of the upper ocean. The most comprehensive observation-based description of the subsurface circulation up to this point was given by Reid (1989, 1994, 1997, 2003), which relied on decades of hydrographic and tracer data. Contrasting our results with these syntheses shows a high degree of similarity at the upper pressure levels in many areas of the global ocean, especially the North Pacific and North Atlantic. In the Southern Hemisphere, where the historical data set was more sparse, more differences between our results and Reid's are apparent. For example, several small-scale undulations in the Agulhas Retroflection and in the Pacific sector of the ACC (between 140°E and 165°E and also between 160°W and 120°W) stand out in our maps, where Reid's analyses show purely zonal flows. Deeper in the water column, more substantial disagreement is found. For instance, at 1000 db and 1500 db the Southern Hemisphere subtropical gyres are oriented predominantly zonally in our results, whereas Reid gives a stronger meridional component at these pressures. In general, the results from Reid show a smoother and more coherent flow at the deeper levels than is seen in the maps computed from Argo observations.

One might expect there to be dissimilarities between Reid's results and the circulation estimates in this study due to the difference in the time periods over which the data were collected. While our estimates span December 2004 to November 2010, the data compiled by Reid for his studies were collected from 1932 to 1991. Another

major difference is the amount of data used in this study (over 480,000 Argo profiles) compared to Reid (5,932 ship-based stations). In addition, our results employ a direct estimate of the absolute velocities at the reference level, whereas Reid relied on a subjective examination of tracer data to estimate absolute flow.

3.5.2 Sverdrup balance

The wind-derived transport ($V_{Sv} - V_E$ in (3.5)), averaged over the entire QuikSCAT period, exhibits the expected large-scale pattern of equatorward flow in the subtropics and tropics and poleward flow in the high latitudes (Figure 3.6). The line of zero wind transport is approximately aligned with the axes of the Kuroshio and Gulf Stream Extensions in the Northern Hemisphere and with the ACC in the Southern Hemisphere. The largest mean wind-derived transports are located in the higher latitudes, but there are local maxima in the eastern parts of most gyres. All of the following results will use wind transport averaged over August 1999 to October 2009 and Argo velocities averaged over December 2004 to November 2010. The longer averaging periods were adopted because they offered a slight reduction in the uncertainties and using the shorter contemporaneous periods produced only negligible differences.

The results of our first test of SB, using *a priori* estimates of the bottom boundary of the wind-driven circulation, are shown in Figure 3.7. The maximum wintertime mixed layer σ_θ values along the line of zero-Sverdrup transport, computed from the mapped mixed layer θ and S, are 26.24, 27.24, and 27.25 kg m^{-3} for the North Pacific, Southern Hemisphere and North Indian, and North Atlantic, respectively. Because the zero-Sverdrup transport line in the Southern Hemisphere was located in the circumpolar ACC, the same value was used for all basins there. The normalized difference between the two sides of (3.5) was determined as

$$\Delta = \frac{V_g - (V_{Sv} - V_E)}{|V_g| + |(V_{Sv} - V_E)|} \tag{3.10}$$

with V_g computed from the mean Argo-derived velocity and density fields and $V_{Sv} - V_E$

from the QuikSCAT wind stress fields. Δ defined in this way is zero where SB is exactly correct and bounded by ± 1. Figure 3.7 gives the minimum Δ after factoring in the uncertainty on V_g. Yellow indicates perfect agreement, while those areas where the designated isopycnal was not found in the mean are shown in dark gray. Overlaid on the normalized difference are contours of ψ at 5 db.

Using these three isopycnals, we infer that SB provides a quantitative description of meridional transport for a large fraction of the global ocean, primarily in the subtropics and tropics. However, SB fails to accurately represent meridional transports in almost all of the ACC and subpolar North Pacific and North Atlantic for this choice of h. In the North Pacific subpolar gyre, the wind-derived transport predicts more poleward flow than is found in the integrated geostrophic transports, which is perhaps not too surprising given that σ_θ 26.24 was chosen based on a ventilated thermocline model of the subtropical gyre. Using σ_θ 27.24, the northward geostrophic transport in the North Atlantic Current region is larger than the wind-derived transport, but north of this area the discrepancy reverses (at least in the part of the subpolar gyre where this isopycnal is present). For the most part, we find more poleward geostrophic transport than wind-derived transport in the northern part of the ACC and less in the southern part. Furthermore, meridional transports in the western boundary areas and the boundary current extensions do not adhere to SB. The poleward wind-derived transport is generally much smaller than the observed geostrophic transport in these regions. Lastly, the eastern boundary regions in the Pacific and Atlantic also exhibit poor agreement with SB.

Examining SB in a different way, we find the minimum p that produces agreement between the two sides of (3.5), within one standard deviation of V_g (Figure 3.8). Regions where no p was found that satisfied SB, within the depth range of these velocity fields (2000 db), are shown in dark gray. While the existence of a p that satisfied (3.5) does not prove per se that SB is valid, it does indicate areas that are suitable candidates for SB. Although the results are somewhat noisy, the same picture

emerges as in the first test: potentially good agreement with SB in the subtropics and tropics and poorer agreement elsewhere. Where agreement is possible, the wind-driven circulation appears to be confined to shallower pressure levels in lower latitudes than in higher latitudes, although small-scale features are prevalent, as expected for an average over 6 years (Wunsch, 2010).

Even if there exists a value for h that balances the two sides of (3.5), is that enough to claim that SB is accurate on anything more than a purely mathematical level? Sverdrup's original derivation assumes a flat-bottom ocean, entirely wind-driven, above a quiescent abyss. While in reality the deep velocity certainly is not zero due to local thermohaline and topographic forcing, we expect that for SB to be valid, the wind-driven circulation must be sufficiently isolated from the deep circulation. To ensure this, we impose as an additional condition needed to satisfy SB that v_g, within $\pm e_v$, is zero for some depth range below h. Since v is related to $\partial w/\partial z$ through (3.1) and $w(z = h) = 0$ when SB is satisfied, this criterion guarantees that $w \approx 0$ in this depth range and thus that the wind-driven layer is well-separated from the deeper circulation. The range chosen here corresponded to 200 db, which is arbitrary, although the results changed insignificantly for any choice from about 150 to 500 db. Stipulating this additional condition substantially decreases the area where SB provides an accurate description of meridional geostrophic transport (Figure 3.9). For the most part, the regions where SB fails under this stricter definition are in higher latitudes and western boundary regions, as well as areas in the central North Atlantic and South Indian subtropical gyres.

These findings align reasonably well with the results of Wunsch (2011), who used a 16-year average of data-assimilated model output to test the form of SB given by (3.2), with w_E given by $w(z = -117$ m). In that analysis roughly 40% of the world's oceans was found to agree with SB. The agreement was largely restricted to the interior subtropical gyres and the tropics, similar to what is presented here, although differences between those results and ours are apparent in the small-scale features.

Considering the different data sets and methods of testing SB, the overall agreement suggests that these results are robust.

Given the evaluation of SB offered by Figures 3.7-3.9, the question that arises is why does SB succeed in some regions and not others? One obvious reason for an apparent mismatch between the observed geostrophic and wind-derived transports in this study is that w may reach 0 at a depth deeper than 2000 db, the limit of the geostrophic velocity data set used here. Similarly, if w never actually vanishes, (3.2) is typically integrated from $z = 0$ to the seafloor so that a kinematic constraint on the flow at the bottom, $w(z = H) = \mathbf{u} \cdot \nabla H$, can be used. This is likely a contributing factor to the lack of agreement in the high latitudes and the ACC, where the flow is more barotropic. At the points in these regions where SB is found to be valid, h is typically closer to 2000 db than is generally the case in the subtropics and tropics.

One potential reason that w might not become sufficiently small is that there are strong vertical motions associated with flow over topography. A simple test comparing the mean depth and bottom slope between the grid points where SB succeeds, as defined by the test shown in Figure 3.9, and those where no agreement is found results in statistically significant differences (p-value < 0.001) between the two groups. Places where SB is valid are on average deeper and flatter than those where SB is inaccurate. While this result does not demonstrate causality, it does validate our notion that SB is most accurate for a deep, flat-bottom ocean, much as Sverdrup originally envisioned.

Another possible reason for disagreement in the high latitudes is that this study uses velocities averaged over 6 years, whereas the transit time for a first baroclinic Rossby wave is much longer in the high latitudes due to the reduction in the Rossby deformation radius (Chelton et al., 1998). While it is unknown whether a considerably longer time average would improve SB in the high latitudes, given the variability of the wind stress and other factors, the time needed for linear baroclinic adjustment there would certainly preclude the 6 year time period used here. Furthermore, many high latitude currents, such as the North Atlantic Current, are forced by both wind

and buoyancy gradients. In these cases, we would expect that a separate wind-driven layer can not reasonably be isolated from other elements of the circulation. Lastly, in the western boundary currents and their extensions, nonlinear dynamics likely play an important role. Because SB is derived from the linear vorticity balance given in (3.1), which neglects such effects, the lack of agreement in these regions is hardly surprising.

3.6 Conclusions

In this study, we have exploited the fact that the Argo array of profiling floats provides an exceptional tool for the estimation of large-scale absolute geostrophic velocities in the upper 2000 db of the ocean with unparalleled spatial and temporal resolution. The maps of global mean geostrophic velocities presented here correspond well with what has been previously reported based on traditional hydrographic data in the upper depth range, while at deeper pressures a more variable and complicated flow is observed. Limitations of the gridded velocity fields stem from the sparse coverage of the Argo array in some regions, specifically the inability to resolve boundary currents. As a purely data-based analysis, these velocity fields make an important contribution to our knowledge of the detailed circulation of the global upper ocean and should be useful for initializing and validating models and state estimations. These fields can also provide the foundation for observational analyses of meridional heat and freshwater transport and help further our understanding of the role of ocean circulation in influencing these important climatic quantities. As long as the Argo array is maintained, these fields can be continually augmented with more data and expanded to cover a longer time period.

The absolute geostrophic velocities presented here have been used to assess the extent to which Sverdrup balance, a simple but ubiquitous theory of the relationship between wind-forcing and ocean circulation, accurately predicts observed geostrophic transports on a point-by-point basis. We find that within the uncertainties there is

good agreement over large regions of the world's oceans, namely the subtropics and tropics away from the boundaries. Thus for a substantial part of the global ocean, Sverdrup balance provides a reasonable quantitative picture of the observed circulation. However, the depth of the wind-driven circulation, defined as the location where the wind-derived transport matches the meridional geostrophic transport, has considerable geographic variability. While the simple model described by Sverdrup balance is a useful starting point for a theoretical treatment of the large-scale circulation, the results presented here imply that it should not be unreservedly accepted as truth.

3.7 Appendix: Objective mapping of Argo data

The technique used in this study to map the quantities of interest (D, $\mathbf{u}(p_0)$, θ, S, p, and mixed layer properties) closely follows that developed by LeTraon (1990). This method estimates both large-scale and small-scale signals from scattered data. The large-scale component, for which statistics are not known and perhaps not even clearly definable, is computed using the objective function fitting procedure of Davis (1985, 2005). A set of functions with spatial scales greater than a given limit, chosen from a complete set of functions, are fit to the data, subject to a zero-bias constraint. The large-scale signal is then removed from the data to produce small-scale anomalies which are objectively mapped following the conventional techniques of Bretherton et al. (1976).

In this study, the large-scale and small-scale signals were defined by different spatial and temporal scales. Spatially, the basis functions chosen to represent the large-scale field were spherical harmonics up to order 15. Thus the large-scale component was the part of the signal with scales $\gtrsim 24^\circ$ latitude/longitude. This order was chosen for the spherical harmonic basis functions to accurately depict the large-scale signal and avoid overlap with the mesoscale field. Temporally, the large-scale signal was computed as a mean monthly annual cycle over the 6 year study period. All data from each month, regardless of year, were used to compute a large-scale field accord-

ing to the protocol outlined by LeTraon (1990) for non-simultaneous data, whereby the covariance between data from different years was set to zero. The small-scale signal, in contrast, was mapped separately for each individual month. It is important to note that separation into large- and small-scale signals is strictly statistical and thus does not necessarily correspond to distinct physical processes.

The statistics of the small-scale signal, i.e., the autocovariance of the anomalies, must be specified *a priori* and are used in estimating both the small-scale field and the large-scale field (for which the least-squares fit to the given basis functions takes into account the correlation of the anomalies). A Gaussian form for the spatial autocovariance was used here, although other forms were tried and did not substantially affect the results. The autocovariance was assumed to depend only on separation distance s according to

$$C(s) = C_0 \exp(-\frac{s^2}{2L^2}) \quad , \tag{3.11}$$

for variance C_0 and decorrelation length scale L.

While typical analyses chose a value for L somewhat arbitrarily, we employ a novel method that determines C_0 and L in an iterative fashion directly from the data for each p or σ_θ level. An initial guess for C_0 and L was used to first estimate the large-scale signal via objective function fitting and remove that signal from the data. Here we used $C_0 = 1$, $L = 250$ km, but testing showed that the final parameters were insensitive to the choice of initial values. The resulting anomalies were then used to calculate the observed autocovariance $\mathcal{C}$ using all pairs of data collected in the same month and separated by spatial lag s,

$$\mathcal{C}_{D'}(s) = \langle D'(\mathbf{x})\, D'(\mathbf{x}+s) \rangle \quad , \tag{3.12}$$

where the brackets denote an ensemble mean taken over all valid pairs of data, and the prime denotes anomalies from the large-scale signal. (3.12) is written for D, but analogous equations were used for all scalar properties being mapped. All data pairs were grouped according to separation distance into 25 km bins and averaged to give

a mean autocovariance curve. Next, a least-squares fit of the observed mean autocovariance curve to (3.11) gave both C_0 and L. The data at the smallest separation distances ($\leq$ 25 km) were excluded from the fit due to probable space-time aliasing. Using the fitted autocovariance parameters, the mapping of the large-scale signal and calculation of the autocovariance were then repeated. This procedure was iterated until the parameter values converged. This novel iterative approach has been tested and validated using both analytically constructed fields and output from a high-resolution model, the results of which can be found in Gray and Riser (2014, submitted).

To maximize the number of data pairs included in the autocovariance estimation and hence the degrees of freedom, the autocovariance is assumed to be isotropic. While this is not strictly true, Davis (1998) found that in the South Pacific the variability is generally isotropic except within about 5° of the equator. Thus the assumption of isotropy most likely introduces significant errors only in the equatorial region, where the validity of the geostrophic relationship is already questionable.

Once the covariance parameters were determined for each p or σ_θ level, the large-scale and small-scale signals were both mapped onto a 1° x 1° horizontal grid at the above-mentioned temporal resolution. Observational error and sub-grid-scale noise were specified to account for an additional 50% of the measured variance in the data; this value was chosen to be reasonably conservative, following Gille (2003a).

To map $\mathbf{u}_{rel}$ and $\mathbf{u}(p_0)$, slight adjustments were made to the basic procedure. LeTraon (1990) and Bretherton et al. (1976) outline methods for mapping multivariate data and for determining fields related to the data through linear operators. As (3.7) and (3.8) show, the relative and reference components of the velocity are related linearly to the D and ψ_0, respectively. Using partial derivatives of both the autocovariance function (3.11) and the spherical harmonic basis functions allowed us to map $\mathbf{u}_{rel}$ from the D data and ψ_0 from the $\mathbf{u}(p_0)$ data. In addition, since the $\mathbf{u}(p_0)$ data were vectors, a simple application of (3.12) was not possible. These data were first multiplied by f to account for the latitudinal dependence of (3.8). Then for each

pair of velocities the vectors were decomposed into longitudinal and transverse components, which are aligned parallel and perpendicular to the axis between the two data points, respectively. Longitudinal and transverse autocovariance curves were computed following Batchelor (1970), who showed that these can be derived from the covariance function describing the velocity streamfunction given that the statistics of the field are isotropic, homogeneous, and stationary. Lastly, a least-squares method was used to simultaneously fit the mean observed longitudinal and transverse curves to the analytical forms of those functions.

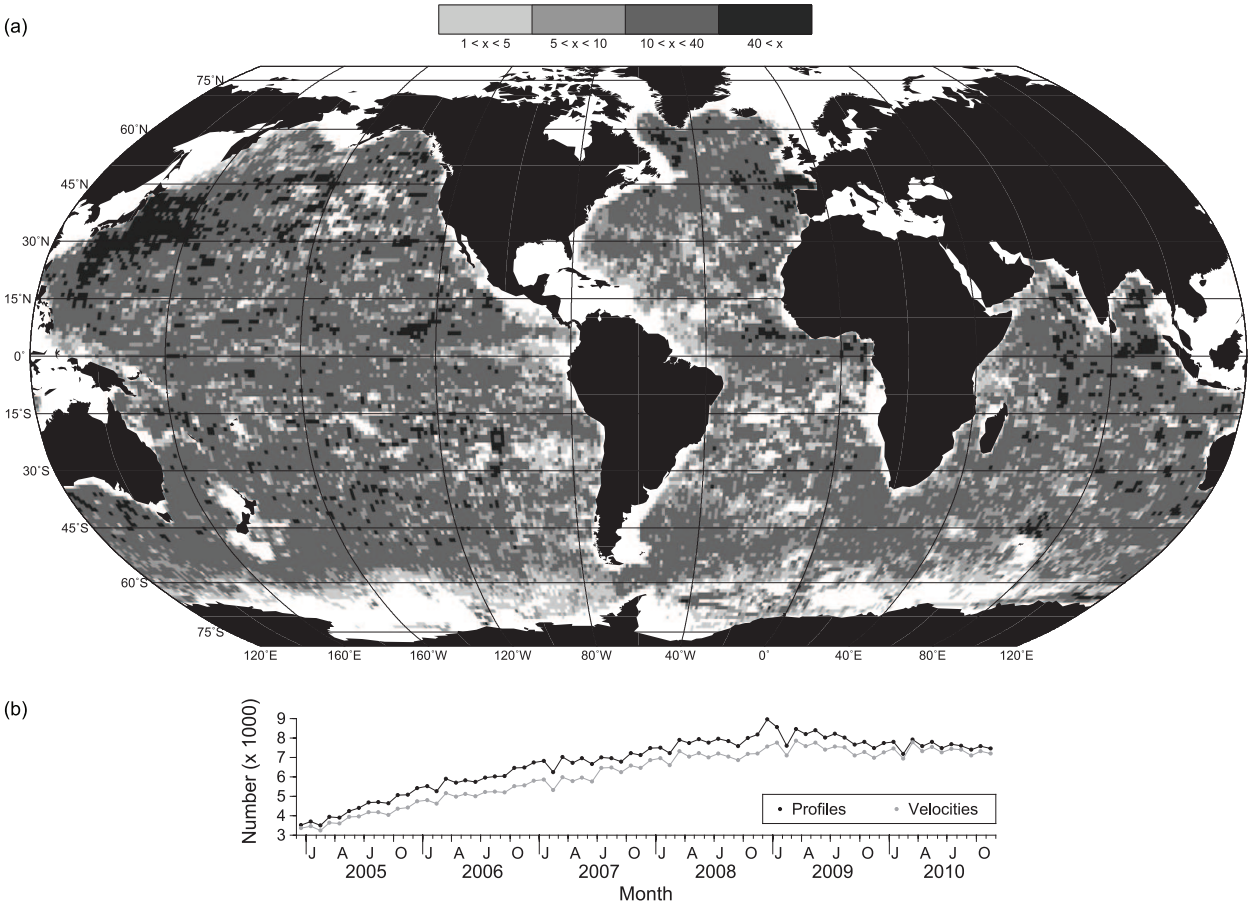

Figure 3.1: (a) Spatial distribution of all profile data, shown as the number of profiles in each 1° x 1° box and (b) temporal distribution of both profile and velocity data shown as number of data in each month during the study period. The spatial distribution of the velocity data is very similar to that shown in (a).

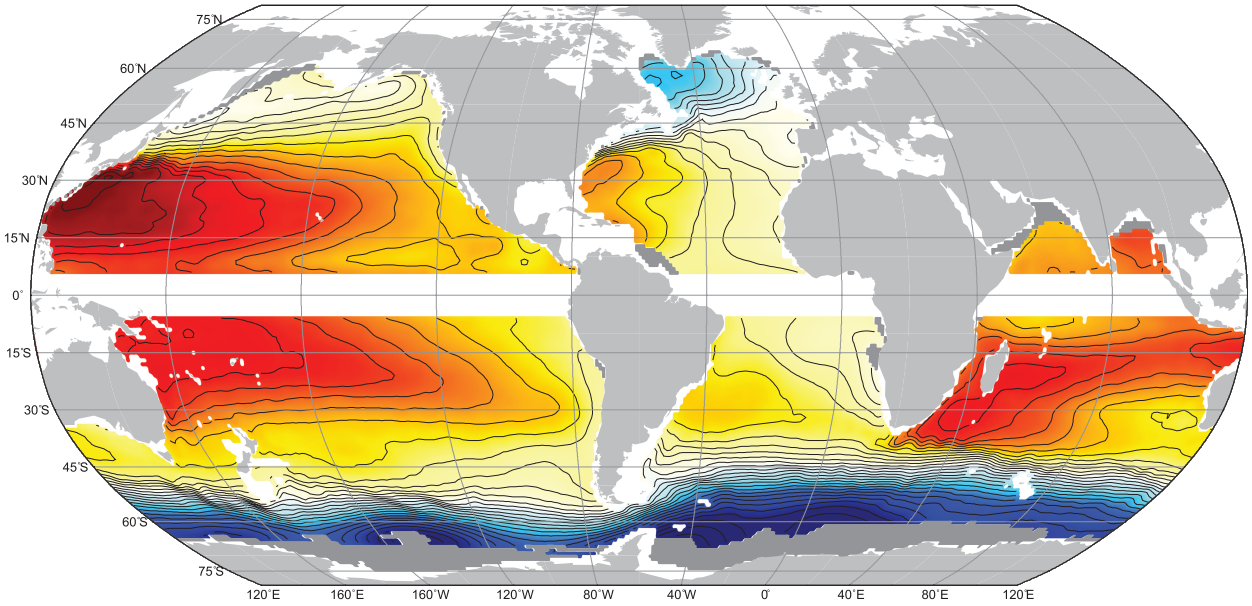

Figure 3.2: Mean absolute geostrophic streamfunction at 5 db from Argo data for Dec 2004 - Nov 2010. Contour interval is 10 dyn cm (1 dyn cm = 10 m^2 s^{-2}). Highs (lows) are shown in red (blue). Dark gray areas indicate where e associated with $|\mathbf{u}|$ was greater than $\sigma_{\mathbf{u}}/8$.

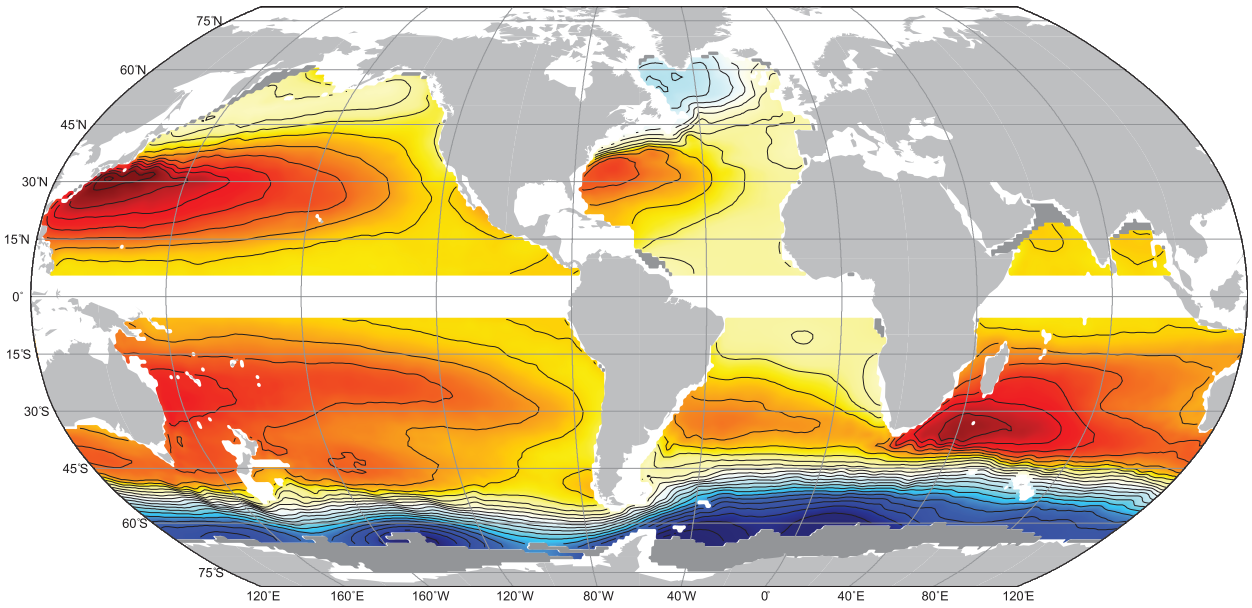

Figure 3.3: Mean absolute geostrophic streamfunction at 200 db from Argo data for Dec 2004 - Nov 2010. Contour interval is 10 dyn cm. Colors as in Figure 3.2.

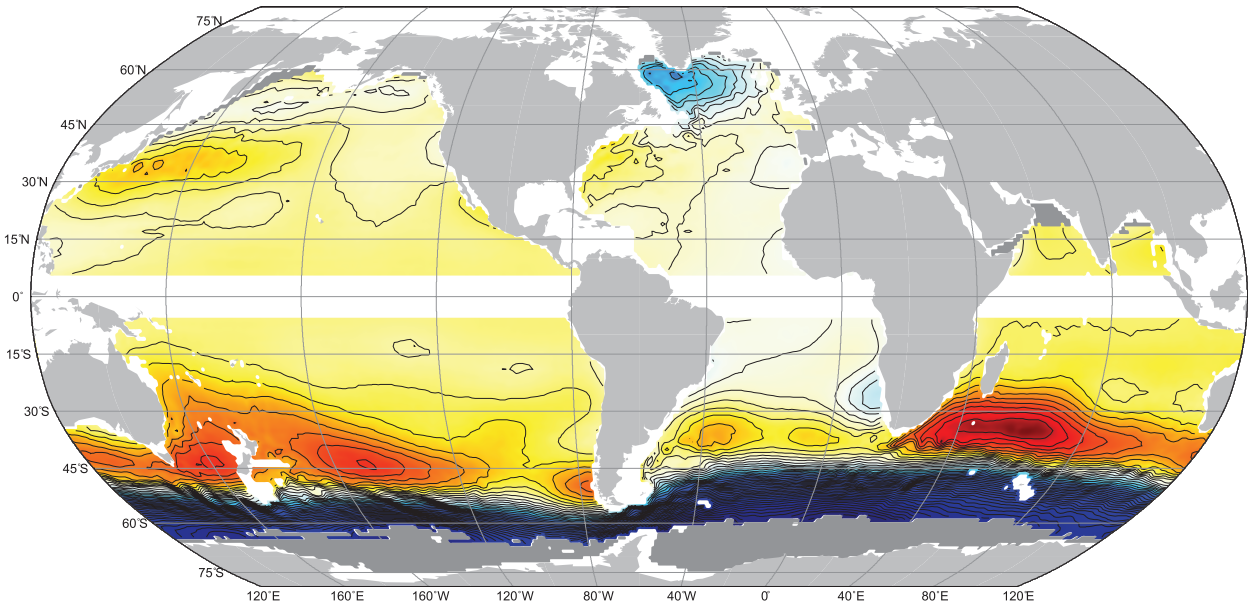

Figure 3.4: Mean absolute geostrophic streamfunction at 1000 db from Argo data for Dec 2004 - Nov 2010. Contour interval is 5 dyn cm. Colors as in Figure 3.2.

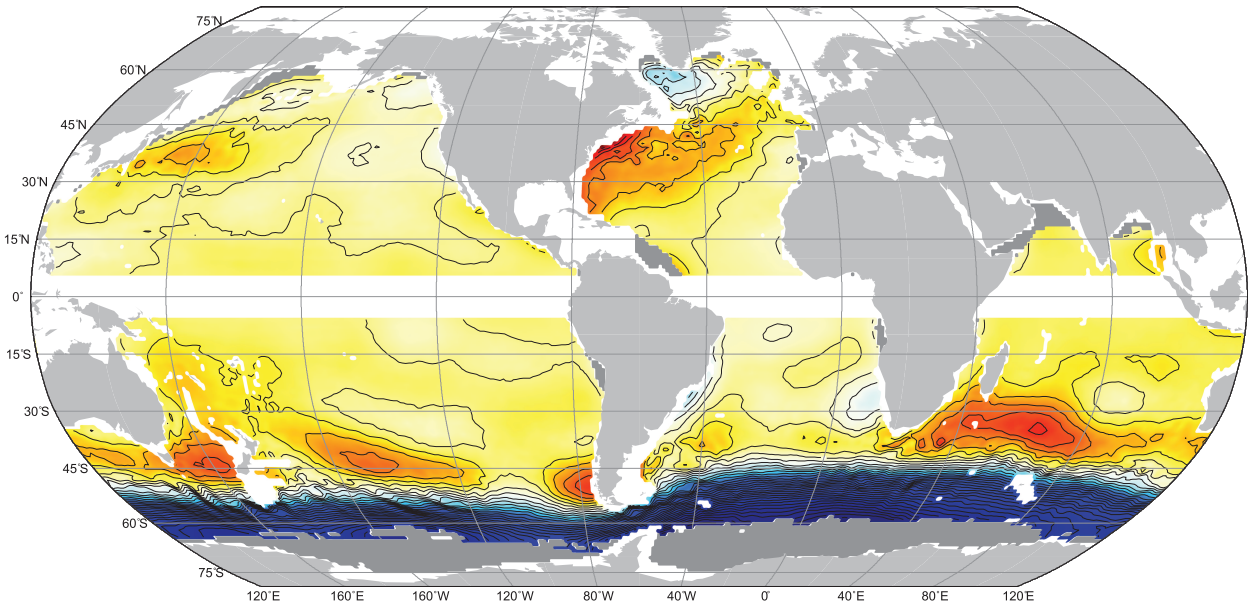

Figure 3.5: Mean absolute geostrophic streamfunction at 1500 db from Argo data for Dec 2004 - Nov 2010. Contour interval is 2.5 dyn cm. Colors as in Figure 3.2.

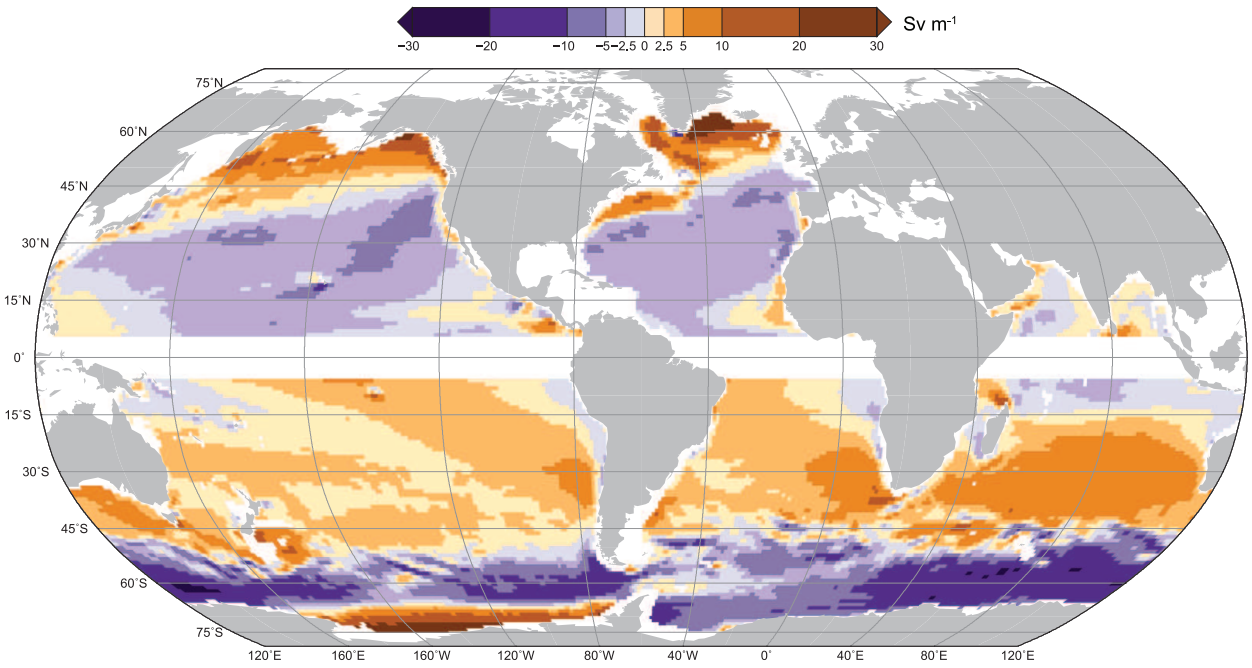

Figure 3.6: Mean wind-derived transport ($V_{Sv} - V_E$) from QuikSCAT in Sv m^{-1}, averaged over Aug 1999 - Oct 2009.

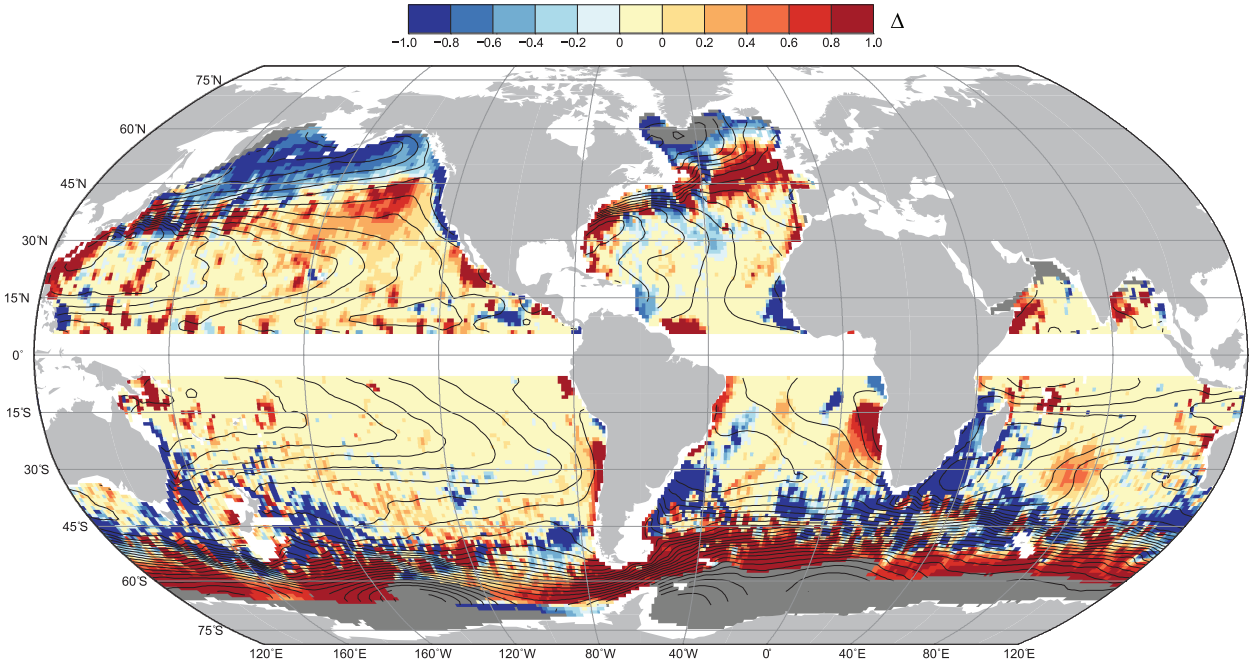

Figure 3.7: Normalized difference Δ between meridional geostrophic transport V_g and wind-derived transport, as defined by Equation (3.10). V_g is computed using the h that corresponds to σ_θ 26.24, 27.24, and 27.25 for the North Pacific, Southern Hemisphere and North Indian, and North Atlantic basins. Δ is the minimum difference taking into account the uncertainty on V_g, with yellow indicating exact agreement. Areas where the given isopycnals were not present in the mean are shown in dark gray. The mean 5 db geostrophic streamfunction is contoured in black at 10 dyn cm intervals.

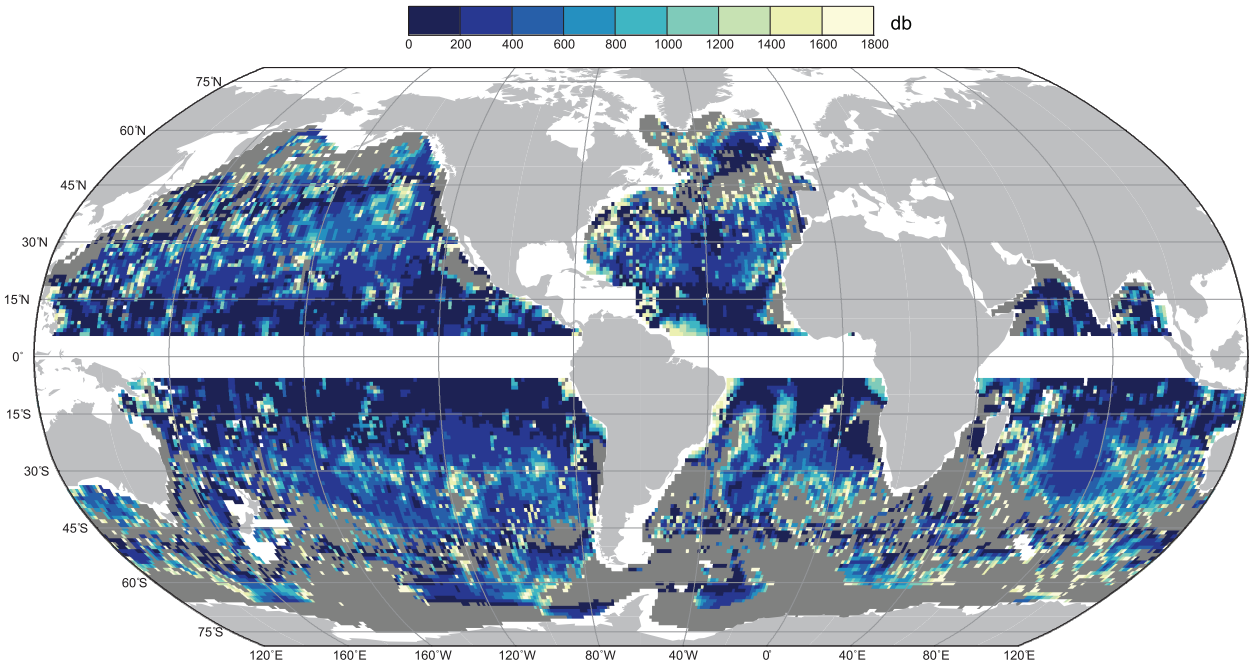

Figure 3.8: Pressure in db used as bottom boundary to give $V_g = V_{Sv} - V_E$. Value shown is minimum given the uncertainty of V_g. In the dark gray areas, no agreement was found in the upper 2000 db.

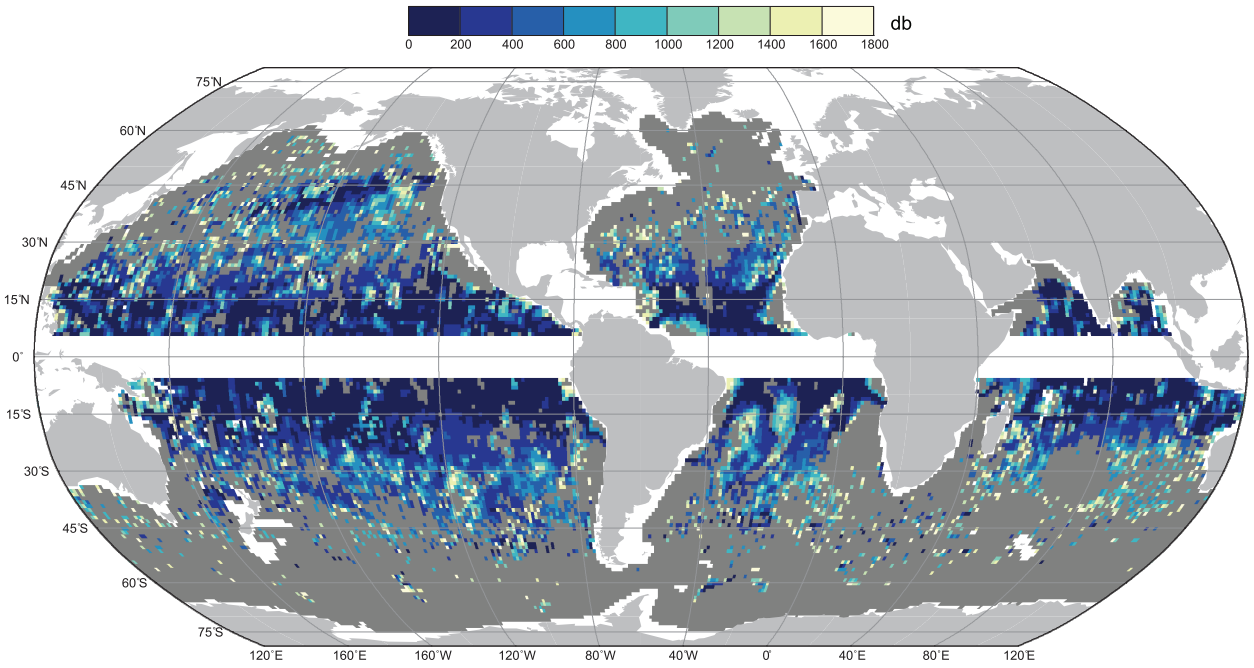

Figure 3.9: Pressure in db used as bottom boundary to give $V_g = V_{Sv} - V_E$, subject to the criterion that $v_g \pm e_v = 0$ over a range of at least 200 db. In the dark gray areas, no agreement was found in the upper 2000 db.

Chapter 4

OBSERVATIONS OF THE MERIDIONAL OVERTURNING CIRCULATION IN THE SOUTHERN OCEAN

4.1 Introduction

The meridional overturning circulation (MOC) of the global ocean is a fundamental component of the climate system, responsible for maintaining the stratification of the ocean, transporting heat and freshwater, and shaping global cycles of carbon, oxygen, and nutrients. The downwelling branch of the deep MOC is driven by air-sea fluxes of heat and freshwater as well as ice formation, both of which create convection and mixing that lead to the formation of dense deep and bottom waters. These processes, which are localized to a small number of regions in the high latitude North Atlantic and around the Antarctic coast, are fairly well characterized. In contrast, the nature and location of the upwelling branch of the MOC are not as fully understood. This part of the MOC, in which dense water must return to the upper ocean and gain oyoyancy, is thought to regulate communication between the deep and shallow oceans, thereby exerting a large influence on the climate system. Therefore, the exact upwelling pathways and the dynamical mechanisms governing those processes have long been a topic of great interest in oceanography.

In one suggested pathway, all of the required upwelling occurs as a result of uniform diapycnal mixing across the thermocline (Munk, 1966; Munk and Wunsch, 1998). However, the widespread large vertical diffusivities necessitated by this scenario have not been observed, leading to the so-called "missing mixing paradox" (Ledwell et al., 1998; Kunze et al., 2006; Ledwell et al., 2011). Recent work has pointed to the

importance of upwelling in the Southern Ocean for closing the MOC (Marshall and Speer, 2012, and references therein). In this framework, two circulation cells exist that are largely adiabatic, thereby avoiding the need for large thermocline diffusivities. In the upper cell, dense waters sink to mid-depths in the North Atlantic to form North Atlantic Deep Water (NADW). This water then advects southward, mixing with Circumpolar Deep Water (CDW) along the way, eventually upwelling along the tilted isopycnals that intersect the surface in the Antarctic Circumpolar Current (ACC). From there, as wind forcing drives the water northward, it gains buoyancy through air-sea fluxes of heat and freshwater. In the lower cell, dense water formed around Antarctica sinks to the bottom and spreads northward through all of the ocean basins as Antarctic Bottom Water (AABW). This water becomes less dense through mixing and other bottom boundary layer processes, thereby rising to mid-depths where it flows southward again as part of the CDW. As with the upper cell, this southward flowing deep water upwells nearly adiabatically in the ACC, completing the overturning circulation. The importance of Southern Ocean upwelling in the global climate system is supported by both theoretical and numerical models (e.g., Döös and Webb, 1994; Toggweiler and Samuels, 1995, 1998). Furthermore, changes to Southern Ocean upwelling are thought to play a central role in both glacial-interglacial cycles (Watson and Naveira Garabato, 2006; Siani et al., 2013) and in the response of the present-day climate to anthropogenic forcing (Caldeira and Duffy, 2000; Sabine et al., 2004; Le Quéré et al., 2007)

Despite its fundamental role in the global circulation of the ocean, previous observational estimates of the southern limb of the MOC have been limited and indirect. Tracer distributions provided the basis for several inferences of Southern Ocean upwelling, starting with Sverdrup (1933) who first proposed a Southern Ocean meridional overturning cell. Based on salinity and other properties, Deacon (1937) deduced a shallow northward flow across the ACC returned by a deep southward flow. Later observational studies of the large-scale circulation of the Southern Ocean focused on

water mass distributions (McCartney, 1977; Piola and Georgi, 1982) and the major fronts of the ACC (Nowlin and Klinck, 1986; Orsi et al., 1995). More recently, basin-scale quantitative estimates of the Southern Ocean branch of the MOC have been computed using inverse methods together with hydrographic data collected primarily through the World Ocean Circulation Experiment (Sloyan and Rintoul, 2001; Talley, 2003; Lumpkin and Speer, 2007) and with a combination of hydrographic and float drift data (Katsumata et al., 2013). Additionally, zonal-average estimates of the Southern Ocean overturning circulation have been constructed from observations of air-sea fluxes (Speer et al., 2000) and from satellite measurements of sea surface height together with climatological wind and density fields (Karsten and Marshall, 2002). However, in situ observations have until recently been relatively sparse and strongly biased towards summer, and detailed observational estimates of the Southern Ocean MOC are still lacking. Furthermore, although many theoretical and numerical models (e.g., McWilliams et al., 1978; deSzoeke and Levine, 1981; Johnson and Bryden, 1989; Marshall and Radko, 2003; Karsten et al., 2002; Olbers and Visbeck, 2005; Hallberg and Gnanadesikan, 2006) indicate that eddies play a leading-order role in the overturning of the Southern Ocean and the associated balances of heat, momentum, and vorticity, their effects are usually parameterized (Marshall, 1981; Danabasoglu and McWilliams, 1995). Southern Ocean eddy fluxes have been estimated from current meter data (Johnson and Bryden, 1989; Phillips and Rintoul, 2000), satellite altimetry (Keffer and Holloway, 1988; Stammer, 1998), and hydrographic observations in conjunction with inverse models (Macdonald and Wunsch, 1996; Sloyan and Rintoul, 2000; Ganachaud and Wunsch, 2000). More recently, Sallee et al. (2011) computed surface eddy diffusivities in the Southern Ocean using satellite altimetry and Trani et al. (2014) computed surface eddy statistics and heat flux from drifter data. Using float observations, the function of eddies in the Southern Ocean has been examined at 900 m by Gille (2003b), who estimated eddy heat and momentum fluxes across the ACC. At this pressure level, the total poleward eddy heat flux was inferred to be 5 to

10 kW m−2 (depending on the mean field used), with significant geographic variation. However, the role of eddies in the Southern MOC has not been fully characterized with direct observations to date.

The data collected by the Argo array of autonomous profiling floats (Roemmich et al., 2004) can now help address these issues, allowing for a more direct and complete observational estimate of the Southern Ocean overturning circulation than previously available. Since 2003, these instruments have been deployed throughout the global ocean, measuring profiles of temperature and salinity in the upper 2000 db and recording trajectory information that can be used to directly estimate the velocity at depth. These data, which are relayed to shore-based data centers in real time, form a data set with global coverage and unprecedented spatial and temporal resolution. Using the hydrographic and velocity data provided by the Argo array, this study computes the mean absolute geostrophic circulation in the Southern Ocean and estimates the effects of eddies on the overturning circulation. Together with observations of wind stress, these analyses further our understanding of the time- and zonal-mean meridional overturning circulation in the upper portion of the Southern Ocean. The resulting picture of the southern limb of the MOC has important advantages, including direct calculations of eddy fluxes that do not rely on parameterization, no ad hoc assumption regarding a reference velocity, and greatly improved data coverage in both space and time.

The goals of this work are to attempt to 1) examine the upper portion of the Southern Ocean meridional overturning circulation using direct observations collected by the Argo array of profiling floats as well as wind stress data, 2) evaluate the contributions of the time-mean and eddy-induced overturning circulations, and 3) investigate the spatial distribution of the eddy-driven component of the MOC. In the following, section 4.2 gives an outline of the dynamical framework used to evaluate the MOC in the Southern Ocean. Detailed descriptions of the data sets and methods used here are provided in sections 4.3 and 4.4, respectively. Section 4.5 presents

the resulting analysis of the different components of the Southern Ocean MOC. We discuss the implications of these findings and give our conclusions in section 4.6.

4.2 Background

The theoretical basis for understanding the MOC in the Southern Ocean has been developed over the last few decades by a number of authors, including deSzoeke and Levine (1981), Johnson and Bryden (1989), Ivchenko et al. (1996), Marshall et al. (1993) and Marshall and Radko (2003). Conceptually, a westerly wind stress τ, which varies in strength meridionally, acts on the ACC to drive a mean eastward flow. Through basic Ekman dynamics, this wind field induces a mean meridional overturning circulation, $\overline{\Psi}$, consisting of net northward flow in the shallow layers. This equatorward transport is returned southward through topographic form drag at depths where the current interacts with significant bottom topography (Munk and Palmén, 1951; Olbers, 1998). Convergence and divergence of the Ekman transport, due to the curl of the wind field, results in downwelling and upwelling, respectively. The resulting meridional overturning circulation, known as the Deacon cell (Döös and Webb, 1994), tends to overturn the isopycnals by mechanically tilting them towards the vertical. This process, combined with large buoyancy forcing at the surface due to air-sea fluxes, produces a strong frontal region across the ACC. The mean available potential energy associated with the resulting horizontal density gradients is released through baroclinic instability, leading to widespread eddy generation throughout the region. The eddies communicate the wind stress from the surface to the bottom where it can be dissipated by topographic stress and simultaneously induce an overturning circulation, Ψ^*, that tends to flatten out the isopycnals. The residual circulation, Ψ_{res}, is given by the net sum of the mean and eddy components of the circulation,

$$\Psi_{res} = \overline{\Psi} + \Psi^* \quad . \tag{4.1}$$

In regions with significant eddy activity, it is the residual circulation that advects tracers, not the Eulerian mean circulation (Marshall and Speer, 2012). The Southern Ocean is unique in that it is the only place in the global ocean where the flow is circumpolar (and thus more closely resembles atmospheric circulation). Furthermore, a substantial portion of the water column is found above the sill depth of region, located at the Scotia Ridge just downstream of Drake Passage. Thus in the upper part of the ACC, the input of momentum to the ocean by the significant wind forcing in the area cannot be balanced by zonal pressure gradient forces. Eddies, through the forces associated with eddy form-drag, are therefore expected to play a leading-order role in driving the meridional overturning circulation of the Southern Ocean (Vallis, 2006).

To estimate the Southern Ocean MOC from observations, this study uses the residual mean framework given by Marshall and Radko (2003) and Radko and Marshall (2006), which is based on the transformed Eulerian mean theory developed for the atmosphere by Andrews and McIntyre (1976). In this formulation, the circulation is considered in a two-dimensional zonally-averaged sense, which provides a compact description of the physical mechanisms controlling the overturning. Given an arbitrary fluid variable $F(x, y, z, t)$ (which depends zonally on x, meridionally on y, vertically on depth z, and on time t), we assume that it can be separated into a time-mean component, $\overline{F}$, and a fluctuation, F', which represents the transient eddy component. The time-mean part of the field can be further divided into a time- and zonal-mean, $\langle\overline{F}\rangle$, and a departure from that mean, $\overline{F}^{+}$, which represents the standing eddy component. The zonal-mean along a closed path is computed as

$$\langle\overline{F}\rangle = \frac{1}{L_x}\oint \overline{F}\,\mathrm{d}x \tag{4.2}$$

where L_x is the length of the zonal integration path. Accordingly, the full field is given by the sum of the time- and zonal-mean, the standing eddy component, and

the transient eddy component,

$$F = \langle \overline{F} \rangle + \overline{F}^{+} + F' \quad . \tag{4.3}$$

Consider the meridional velocity, v, in an isopycnal layer of thickness h. Averaging in isopycnal layers instead of at fixed depths more accurately reveals the essential dynamics of the Southern Ocean MOC because the ocean interior is largely adiabatic (McDougall and McIntosh, 2001; Viebahn and Eden, 2012). Using the definitions above, the time- and zonal-mean meridional transport in the layer, $\langle \overline{vh} \rangle$, can be separated into three components via simple Reynolds averaging, so that

$$\langle \overline{vh} \rangle = \langle \overline{v} \rangle \langle \overline{h} \rangle + \langle \overline{v}^{+} \overline{h}^{+} \rangle + \langle \overline{v'h'} \rangle \quad . \tag{4.4}$$

The first term gives the Eulerian mean component of the isopycnal transport, the second term is the contribution of the standing eddies to the mean transport, and third term, which is also known as the "bolus transport", represents the contribution due to transient eddies. Although the individual eddy components of velocity, v^{+} and v', and thickness, h^{+} and h', must by definition be zero in the time- and zonal-mean, the correlation between them does not necessarily vanish. In fact, the mean eddy fluxes, $\langle \overline{v}^{+} \overline{h}^{+} \rangle$ and $\langle \overline{v'h'} \rangle$, have a significant impact on the total mean isopycnal transport in highly-eddying areas.

As discussed by McDougall and McIntosh (2001) and Viebahn and Eden (2012), a time-mean isopycnal meridional overturning streamfunction, $\psi(y, b)$, can be determined by integrating the time- and zonal-mean meridional transport $\langle \overline{vh} \rangle$ in isopycnal coordinates. The resulting isopycnal streamfunction can then be mapped to depth coordinates using the mean isopycnal heights, which produces Ψ_{res} to first-order (McIntosh and McDougall, 1996; Vallis, 2006). The derivatives of the residual overturning streamfunction $\Psi_{res} \cong \psi[y, \langle \bar{b}(y, z) \rangle]$ give the meridional and vertical components of the residual velocity, v_{res} and w_{res}, according to

$$(-\frac{1}{L_x}\frac{\partial \Psi_{res}}{\partial z}, \frac{1}{L_x}\frac{\partial \Psi_{res}}{\partial y}) = (v_{res}, w_{res}) \quad . \tag{4.5}$$

The residual velocity is the velocity that, when advecting the mean isopycnal thickness, results in the total mean isopycnal transport (Vallis, 2006); accordingly $\langle\overline{vh}\rangle$ can be expressed in terms of v_{res} and the mean thickness $\langle\overline{h}\rangle$ as

$$\langle\overline{vh}\rangle = v_{res}\langle\overline{h}\rangle \quad . \tag{4.6}$$

Combining this expression for v_{res} with (4.4) gives

$$v_{res} = \frac{\langle\overline{vh}\rangle}{\langle\overline{h}\rangle} = \langle\overline{v}\rangle + \frac{\langle\overline{v}^{+}\overline{h}^{+}\rangle}{\langle\overline{h}\rangle} + \frac{\langle\overline{v'h'}\rangle}{\langle\overline{h}\rangle} \quad , \tag{4.7}$$

which shows that the residual velocity is equivalent to the thickness-weighted mean velocity.

In the theoretical model of Marshall and Radko (2003) and subsequent work, wind forcing drives the Eulerian mean circulation. Wind stress applied at the surface results in a time- and zonal-mean meridional ageostrophic velocity, $\langle\overline{v_a}\rangle$, through Ekman dynamics. Thus, in the surface Ekman layer the mean meridional transport due to wind-forcing is proportional to the time- and zonal-mean zonal wind stress $\langle\overline{\tau}^{x}\rangle$ according to

$$\langle\overline{V}_{Ek}\rangle = \langle\overline{v_a h}\rangle = -\frac{\langle\overline{\tau}^{x}\rangle}{\rho_0 f} \tag{4.8}$$

where f is the Coriolis parameter (< 0 in the Southern hemisphere). If the mean meridional velocity $\langle\overline{v}\rangle$ also has a component due to geostrophic circulation (i.e., $\langle\overline{v_g}\rangle \neq 0$), then (4.8) is simply the Ekman component of the total Eulerian mean meridional transport.

An important practical aspect of any analysis of the zonally-averaged MOC is the choice of the path for the zonal integration. In the Southern Ocean, the ACC exhibits a number of permanent meanders along its path (i.e., standing eddies) that are associated with topographic features. Integrating along time-mean streamlines of the flow as opposed to latitude circles gives the net transport across the path of the ACC, providing a more natural and illuminating view of the Southern Ocean MOC and its associated physical budgets (Marshall et al., 1993). Using a numerical model

of the ACC, Ivchenko et al. (1996) found that integrating around lines of latitude obfuscates important dynamics of the circulation, giving an incomplete picture of the MOC. Similarly, Treguier et al. (2007) showed that integrating around latitude circles produced a widespread southward surface flow in a high-resolution model of the Southern Ocean, contrary to established knowledge of the circulation in the region (Rintoul et al., 2001). Marshall et al. (1993), and later Marshall and Radko (2003), argue that using a streamwise coordinate system in which zonal averages are computed along time-mean streamlines of the flow completely eliminates the contribution of both the cross-stream geostrophic velocity and the standing eddies, leaving transient eddies solely responsible for all cross-stream fluxes. However, the validity of this assertion depends on how exactly the streamwise coordinates system is defined, since in general the flow is vertically sheared with some rotation of the time-mean velocity vectors with depth (Ivchenko et al., 1996). The standing eddy contribution can be significantly reduced with an appropriate choice of streamlines, thereby resulting in a zonal-mean MOC that is more consistent with the physical understanding of the Southern Ocean circulation Viebahn and Eden (2012). The zonal integration paths used in this study are discussed in more detail in section 4.4. Here we simply note that the zonal-mean in (4.2) and all subsequent equations is actually an average along streamlines of the flow. Furthermore, throughout the remainder of this study the terms zonal and meridional will be used to refer to the along-stream and cross-stream directions.

4.3 Observations

4.3.1 Oceanographic data

The primary data set used in this study consists of hydrographic and trajectory data collected by the Argo array of autonomous floats. The quasi-Lagrangian profiling floats that comprise this array are distributed throughout the major ocean basins with a nominal spacing of 3000 km. Each float executes a mission cycle in which it descends

to a preprogrammed parking pressure, drifts with the predominant currents at that level for a specified amount of time (typically 9 days), then ascends to the surface while recording profiles of temperature T and salinity S as a function of pressure p in the upper 2000 db. At the surface the floats upload their data and obtain a fix of their location via positioning satellites, which can be used to determine the velocity at depth. Gray and Riser (2014) give more complete details of this data set, including technical aspects of the floats and the quality control procedures that were implemented. The portion of the global data set used in this study includes all data south of 40°S within the 6 year period from 1 December 2004 to 30 November 2010, which consists of 102,618 T and S profiles and 94,048 velocity estimates from 1,311 individual floats. Figure 4.1 shows the data distribution in space and time.

Profiles of the specific volume anomaly $\delta(S, T, p)$ were calculated from the T and S profiles, and then dynamic height D was computed according to

$$D = \int_{p_0}^{p} \delta dp \tag{4.9}$$

where the reference pressure p_0 was set to 900 db to allow for easy combination with the trajectory data. Dynamic height was calculated at 29 regular pressure levels in the upper 2000 db. Profiles of potential temperature θ, S, and p as a function of potential density σ_θ were constructed using regularly-spaced σ_θ levels ranging from 22.4 to 27.95 kg m^{-3}. The deepest p and average θ and S of the mixed layer were determined using the density algorithm of Holte and Talley (2009). In addition, the trajectory information from each float was used to estimate the average velocity at the parking depth during each cycle following the techniques given in Gray and Riser (2014). As described in that paper, each velocity estimate was adjusted to the common reference pressure p_0 using the geostrophic shear between the parking depth and p_0 that was determined from the mapped D fields (described below in section 4.4).

4.3.2 Wind stress data

Two observational estimates of wind stress were used to estimate the Ekman contribution to the Eulerian mean overturning circulation given in (4.8). The first was derived from observations from the NASA SeaWinds scatterometer onboard QuikSCAT. These data, hereafter QuikSCAT winds, were obtained from the Centre de Recherche et dExploitation Satellitaire (CERSAT), at IFREMER, Plouzané (France). A gridded product was used that gave monthly 10 m wind stress magnitude and direction at 0.5° horizontal resolution for the period August 1999-October 2009. The second wind stress data set used here was the climatology from the National Oceanography Centre, hereafter NOC winds (Josey et al., 2002). These gridded wind stress estimates were constructed from in situ meteorological observations spanning the period 1980-93 and have 1° horizontal resolution.

4.4 Methods

The theoretical model of the Southern Ocean MOC given in section 4.2 was evaluated using observations from the Argo floats together with the wind stress data. Each of the components of the meridional transport given in (4.4) was computed separately. The individual consitutents were then combined and analyzed in order to characterize the mean meridional overturning circulation in the Southern Ocean.

4.4.1 Streamwise coordinate system

Constructing a zonal-mean picture of the overturning circulation in the Southern Ocean first requires a choice of the integration path for computing zonal averages. Given the advantages discussed above in section 4.2 for choosing streamlines of the flow instead of latitude circles, using these contours is highly desirable. However, previous studies have used a number of different derivations of such streamlines, including the time-mean barotropic streamfunction (Ivchenko et al., 1996; Treguier et al., 2007),

time-mean surface geostrophic streamfunction derived from altimetry (Karsten and Marshall, 2002), the Montgomery potential in each isopycnal layer (MacCready and Rhines, 2001; Hallberg and Gnanadesikan, 2001), contours of the Bernoulli potential (Polton and Marshall, 2007), and depth-averaged potential temperature (deSzoeke and Levine, 1981; Abernathey and Cessi, 2014). Viebahn and Eden (2012) report an extensive analysis of the impacts of the choice of streamline on the contribution of the standing eddy component to the meridional overturning circulation using an idealized high-resolution numerical model of the Southern Ocean. They find that in general, the standing eddy part of an isopycnal streamfunction vanishes exactly only when the zonal integration takes place along depth-dependent horizontal isolines of time-mean buoyancy. If the flow is perfectly depth-independent and horizontally non-divergent everywhere, the Eulerian mean and standing eddy streamfunctions will also be identically zero when integrating around time-mean horizontal streamlines. When those conditions are not met, using depth-dependent horizontal streamlines leads to a significantly reduced standing eddy streamfunction but also requires a nonorthogonal curvilinear coordinate system that introduces considerable technical complexity. However, according to the conclusions of Viebahn and Eden (2012), using geostrophic streamlines from a fixed depth in the surface layer (the "contour depth") results in a substantially reduced standing eddy component and also has the practical simplification of providing an orthogonal coordinate system. To evaluate the sensitivity of the resulting MOC to the choice of contour depth, the meridional overturning circulation was computed in this study by integrating along time-mean absolute geostrophic streamlines at two different levels, 5 db and 1000 db. In the following, the results using the 1000 db contour depth are given, and any significant differences with the results using the 5 db contour depth are discussed where appropriate.

To determine the time-mean streamlines of the flow that served as the depth-independent curvilinear coordinate system for the rest of the analysis, gridded estimates of absolute geostrophic velocity in the upper 2000 db of the Southern Ocean

were constructed from the Argo data set. At each of the 29 pressure levels, the D data were mapped to a 1° horizontal grid on monthly timescales using the optimal multiscale iterative technique described in Gray and Riser (2014) and Gray and Riser (2014, submitted). Using that fact that horizontal derivatives of D at any p are proportional to the geostrophic shear between p and p_0, the velocity on each pressure surface relative to the velocity at p_0 was also computed. Next, the estimates of absolute velocity at p_0 were mapped onto the same spatial and temporal grid, producing gridded velocity fields along with an associated geostrophic streamfunction. Summing the relative velocity on each pressure surface with the reference velocity at p_0 then gave absolute geostrophic velocities throughout the upper 2000 db on monthly timescales. For both D and the velocity at p_0, gridded estimates were computed for the entire world ocean using a global Argo data set (see Gray and Riser, 2014, for full details); the portion of the fields in the Southern Ocean were then selected for this study. The resulting absolute geostrophic streamfunction was averaged over the entire study period (Dec 2004-Nov 2010) to provide the time-mean geostrophic circulation in the Southern Ocean.

For each contour depth, the time-mean geostrophic streamfunction at that pressure level was used to find streamlines that formed closed circumpolar paths in the Southern Ocean. For the 5 db streamfunction, the selected streamlines spanned a range of 97.5 dyn cm and were spaced 2.5 dyn cm apart (where 1 dyn cm = 10 m^2 s^{-2}). Because the flow is weaker at 1000 db, the range of circumpolar streamlines used for that contour depth was 41 dyn cm with 1 dyn cm spacing. For each set of streamlines, we normalized the streamline values so that the southernmost streamline was at 0 dyn cm and calculated the length L_x of each streamline using (4.2). The mapping procedure used to construct the absolute geostrophic streamfunction did not provide estimates at grid points where the mean bottom depth was less than 900 m. The small portion of the interpolated streamlines that crossed these regions ((1.5% of the total streamline length, mainly from the Argentine shelf and the Crozet and

Kerguelen Plateaus) were excluded from all zonal averages.

4.4.2 Eulerian mean circulation

The Eulerian mean meridional transport $\langle\overline{v}\rangle\langle\overline{h}\rangle$ was calculated from (4.4) and (4.8) using the Argo observations and wind stress data. If the time-mean streamlines at each depth are used as the streamwise coordinate system, then the time-mean cross-stream geostrophic velocity is identically zero everywhere. However, this study takes horizontal streamlines from only one depth as the coordinate system at all depths for the reasons discussed in section 4.4.1. In areas where the mean flow rotates with depth, this choice of a depth-invariant coordinate system will result in a non-zero time-mean cross-stream velocity. Therefore both components of the time-mean cross-stream velocity, $\langle\overline{v_g}\rangle$ and $\overline{v}^+$, were calculated explicitly for this analysis. The gridded absolute geostrophic velocities computed from float data, described in the previous section, provided estimates of geostrophic velocity, $\mathbf{u}_g(p)$. In order to compute an isopycnal streamfunction and to determine the layer thicknesses, the profiles of $p(\sigma_\theta)$ were also mapped on σ_θ surfaces using the same optimal analysis procedure used for the dynamic height and reference velocity mapping. Gridded estimates of the mixed layer p, θ, and S were also constructed. Using these mapped fields, the monthly absolute geostrophic velocities in the upper 2000 db were converted to isopycnal coordinates. Using discrete σ_θ layers spanning 24.55 to 27.9 kg m^{-3}, the mean velocity in each isopycnal layer was computed. Although this study uses only potential density layers, the overturning circulation should also computed using neutral density layers (Jackett and McDougall, 1997) because the resulting circulations can potentially differ significantly (McIntosh and McDougall, 1996). Next, the pressures and velocities were averaged in time over the six-year period and interpolated horizontally to the streamline coordinates. The velocities were then rotated into along-stream and cross-stream components, and the time-mean isopycnal layer thickness $\overline{h}(\sigma_\theta)$ and associated depth $\overline{z}(\sigma_\theta)$ were determined.

The time-mean values $\overline{h}(\sigma_\theta)$, $\overline{v_g}(\sigma_\theta)$, and $\overline{z}(\sigma_\theta)$ were averaged along each streamline to produce $\langle\overline{h}\rangle$, $\langle\overline{v_g}(\sigma_\theta)\rangle$, and $\langle\overline{z}(\sigma_\theta)\rangle$. For each streamline, zonal averages were computed only for those isopycnal layers that were fully resolved at all times in the upper 2000 db, the vertical limit of the Argo data set, which ranged from 27.78 kg m^{-3} at the southernmost streamline to 27.71 kg m^{-3} at the northernmost. Next, the time- and zonal-mean meridional velocities and isopycnal thicknesses were multiplied together with L_x to give the Eulerian mean meridional transport in each isopycnal layer and for each streamline, s. This estimate of meridional transport was mapped to depth coordinates using the time- and zonal-mean depth of each isopycnal $\langle\overline{z}(s,b)\rangle$, calculated from the gridded estimates of $\overline{p}(\sigma_\theta)$ assuming that the fluid is Bousinessq with $\rho_0 = 1030$ kg m^{-3}. A final coordinate transformation from streamline coordinates to equivalent latitude coordinates was then carried out, where the equivalent latitude, $y(s)$, is that which encloses the same area as the streamline s (McDougall and McIntosh, 2001).

The wind-driven part of the Eulerian mean circulation was determined using the QuikSCAT and NOC wind stress data. The two different estimates allow us to test the sensitivity of the study to the exact wind product used. For each data set, the zonal and meridional wind stresses were averaged in time and then interpolated to the locations of the time-mean geostrophic streamlines for each contour depth. After rotation into along-stream and cross-stream directions, the time-mean meridional Ekman transport was computed as $\overline{\tau}^x/(\rho_0 f)$ with $\rho_0 = 1030$ kg m^{-3} as above. The time-mean Ekman transport was then integrated along each streamline to produce the total Ekman transport across each streamline, $L_x\langle\overline{V}_{Ek}\rangle$. As was done with the geostrophic component, this transport was converted to equivalent latitude coordinates to give $L_x\overline{V}_{Ek}(y)$, the Ekman component of the Eulerian mean meridional transport. Lacking knowledge of the detailed structure of the Ekman velocity within the wind-driven layer, the isopycnal at which the Ekman value was reached was assumed to be the mean mixed layer density along each streamline. For each streamline, only isopy-

cnal layers above the shallowest bottom depth along that streamline were included in this analysis; Ekman velocities in the bottom boundary layer were therefore not represented.

4.4.3 Eddy circulation

Both the standing eddy and transient eddy contributions to the Southern Ocean MOC were estimated in this study using the Argo observations of velocity and density. The standing eddy circulation is often assumed to be zero given a coordinate system that follows the flow of the ACC. However, as our analysis uses time-mean streamlines from one depth as the contours for zonal integration, that assumption is not accurate (Viebahn and Eden, 2012). Therefore the standing eddy component of the MOC is calculated expressly using the gridded $\overline{v_g}(\sigma_\theta)$ and $\overline{h}(\sigma_\theta)$ fields described above. For each isopycnal layer, subtraction of the time- and zonal-mean gave the standing eddy part of each field according to

$$\overline{v}^+ = \overline{v_g} - \langle \overline{v_g} \rangle, \qquad \overline{h}^+ = \overline{h} - \langle \overline{h} \rangle \quad . \tag{4.10}$$

Multiplication of $\overline{v}^+$ and $\overline{h}^+$, followed by averaging along each streamline, gave $\langle \overline{v}^+ \overline{h}^+ \rangle$, which was then integrated vertically with buoyancy to produce the isopycnal streamfunction $\psi^+(s,b)$. Using the same procedure that was used for the Eulerian-mean streamfunction, $\psi^+(s,b)$ was converted to depth and equivalent latitude coordinates to give $\Psi^+(y,z)$, the standing eddy overturning streamfunction.

As discussed in section 4.2, transient eddy fluxes are thought to be of first-order importance to the overturning circulation in the Southern Ocean above the level of interaction with the bottom topography. Therefore any observational study of the Southern Ocean MOC must account for these fluxes in some way in order to be complete. Observational estimates of transient eddy fluxes have previously been parameterized based on sea surface height variability (Stammer, 1998; Karsten and Marshall, 2002) or calculated directly from moored current meters (Wunsch, 1999). The

data used in these methods, however, have limited coverage in either the vertical (for satellite methods) or the horizontal (for mooring-based techniques). Here we estimate transient eddy thickness fluxes, $v'h'$, using the individual Argo float measurements, following the procedure described by Gille (2003b).

The central idea of this technique is that each individual measurement recorded by an Argo float is considered to be an instantaneous measurement. The velocity estimate and the profiles collected during one mission cycle of a float were considered as concurrent measurements and were collocated at the point in space and time at the midpoint in the float's drift. Using the direct estimate of the float's velocity at the reference level p_0, along with the geostrophic shear implied by the monthly mapped dynamic height fields, a profile of instantaneous velocity was estimated for each float cycle. In addition, the T and S profiles were used to compute an instantaneous profile of isopycnal thickness $h(\sigma_\theta)$ and to convert the velocity profile from p coordinates to σ_θ layers. The velocity profiles were then rotated into along-stream and cross-stream components. To estimate the transient eddy meridional velocity and isopycnal thickness, the time-mean fields calculated in section 4.4.2 were subtracted from each instantaneous profile according to

$$v'(t) = v(t) - \overline{v}, \qquad h'(t) = h(t) - \overline{h} \quad . \tag{4.11}$$

A total of 32,323 pairs of velocity and thickness profiles were found within the region of circumpolar streamlines during the 6-year study period.

Next, the pairs of profiles were multiplied together to give individual estimates of $v'h'$ in each isopycnal layer. The float-derived eddy fluxes do not adequately capture the high frequency component of the eddy variability, due to the approximately 10-day measurement period. Gille (2003b) examined this issue in detail using current meters moored in the Southern Ocean, followed by a similar analysis in Chinn and Gille (2007) using observations in the North Atlantic. By comparing eddy fluxes calculated from the moored records with the same fluxes low-pass filtered, Gille (2003b) found

that eddy heat fluxes calculated using a 10-day measurement period accounted for 88% of the total eddy heat flux, which the results of Chinn and Gille (2007) confirmed. Because eddy isopycnal thickness fluxes are comparable to eddy buoyancy fluxes (since $v'h' \sim v'b'/\overline{b_z}$, Vallis (2006)), we expect that a similar scaling is suitable for the thickness fluxes computed in this study. Therefore, the eddy fluxes presented here were scaled by a factor of 1/88%. Future work, however, should use moored current meter records in the Southern Ocean to directly determine the appropriate scaling for eddy fluxes of isopycnal thickness calculated using the methods described here, which will provide a more accurate correction for the temporal under-sampling by the Argo floats.

Lastly, the scaled eddy thickness fluxes in each layer were interpolated onto the locations of the streamlines. Several different averaging and interpolation techniques were tested, including a box average in streamwise coordinates and a simple objective analysis estimation (Bretherton et al., 1976). The results given here, which are representative of the overall pattern that was consistently found, were obtained using a spherical radial basis function approximation technique (Gray and Riser, 2014, submitted) to fit a surface to all of the available data. The particular radial basis used here was the spherical inverse multiquadric (Hardy and Göpfert, 1975) with a 30 km e-folding scale, although length scales of 20 km, 60 km, and 120 km were also tested. All available data from the study period were used together to form a mapped estimate of the time-mean eddy thickness flux $\overline{v'h'}$. These fields were then averaged along each streamline to produce estimates of the mean meridional transport due to transient effects in each isopycnal layer, $\langle\overline{v'h'}\rangle$. Integrating this transport over the isopycnal layers above the mean mixed layer density gave an estimate of the total transient eddy transport in the surface layer. Due to the uncertainties associated with the eddy thickness fluxes, integration of the meridional transports over larger depth ranges did not provide statistically meaningful results.

This methodology, although based on earlier work by Gille (2003b) and Chinn and

Gille (2007), is a new application of profiling float observations. Thus, the question of how well these data resolve the eddy fluxes is of central importance to the validity and accuracy of the results, and several significant caveats exist. While the float-derived "instantaneous" velocity is actually an average over approximately 10 days, the thickness profile is calculated from the T and S measurements taken over a few hours, and the geostrophic shear used to extend the velocity estimate from the parking pressure to the rest of the water column represents a monthly mean value. The resulting mis-match between the temporal and spatial scales of the v and h profiles may considerably affect the resulting fluxes. Furthermore, it remains to be demonstrated that the sampling density of the floats in the Southern Ocean is capable of resolving eddy flux fields that may be both strongly localized in space and episodic in time, with large outliers that can potentially skew the mean (Chinn and Gille, 2007). Future work should verify and validate the eddy thickness fluxes computed with the techniques described here using a variety of approaches. These include comparisons with float-based observations of absolute velocity at 12-hour intervals collected by EM-APEX floats (Sanford et al., 2005) and with surface velocities derived from satellite altimetry. In addition, a detailed analysis of a high-resolution eddy-resolving model simulation that has been sampled in an Argo-like fashion should be conducted in order to determine both how well the Argo observations measure eddy fluxes and how accurate the monthly mapped dynamic height, T, S, and reference velocity fields are. Such work could potentially provide a correction to account for some of the missing small-scale components in the eddy flux estimates. Lastly, as Gille (2003b) showed, the particular mean field used to calculate eddy fluxes can greatly affect the result, so different mean fields should also be assessed.

4.5 Results and Discussion

4.5.1 Eulerian mean circulation

The mean geostrophic circulation of the Southern Ocean over the period Dec 2004-Nov 2010 (Figure 4.2) is dominated by the eastward-flowing ACC, which decreases in strength with depth. The mean absolute geostrophic streamfunctions at 5 db and 1000 db reveal the presence of permanent meanders in the otherwise predominantly zonal flow, which are associated with flow over the main topographic features of this region such as the Kerguelen Plateau at about 70°E, Macquarie Ridge at 145°E, the Pacific-Antarctic Ridge at about 150°W, and Drake Passage (Figure 4.3). Although the near-surface geostrophic streamfunction shown in Figure 4.2 corresponds well overall with the time-mean geostrophic streamfunction obtained using TOPEX/Poseidon altimetry data by Karsten and Marshall (2002), the Argo-dervied flow exhibits sharper gradients in many places and more significant meridional excursions than the altimetry-based streamfunction. In many regions, the magnitude of the velocity decreases with depth but the direction of the flow is approximately the same at all depths in the upper 2000 db, suggesting that some areas of the ACC may be equivalent barotropic. However, in other regions, particularly around large topographic features, the velocity vectors exhibit significant veering or backing with depth, indicating the presence of larger vertical velocities. Because the flow in the ACC is in general not depth-independent, the use of time-mean geostrophic streamlines from one contour depth for zonally averaging is expected to lead to reduced, but not vanishing, Eulerian mean and standing eddy overturning circulations, based on the findings of Viebahn and Eden (2012). In the remaining discussion, the results from the analysis using the 1000 db contour depth are shown, and any significant differences between these results and those obtained using the 5 db contour depth are noted.

The strong eastward flow in the ACC is apparent in the time- and zonal-mean

zonal velocity (Figure 4.4a), which was isopycnally averaged and then mapped to depth coordinates using the mean depths of the buoyancy surfaces, $\langle \overline{z}(s,b) \rangle$. Above the maximum time-mean mixed layer depth found along each streamline (shown by the thick gray line), the zonal velocities decrease towards the surface, which stems from the isopycnal averaging process because the shallowest isopycnals are not present year-round. Overall, mean zonal speeds were found to range from 2.3 to 11 cm s^{-1} in the isopycnal layers resolved by the Argo data set. In contrast, the time- and zonal-mean meridional velocity (Figure 4.4b) is two orders of magnitude smaller, with a maximum value of 0.11 cm s^{-1}. Using the average error estimate associated with the mapped geostrophic velocities in this region, the standard error on the mean for the zonal- and time-mean velocity was determined to 0.04 cm s^{-1}. Given that uncertainty limit, only the mean meridional velocities in the southern portion of the ACC are statistically different from zero. In this region, a northward mean flow is found extending throughout the upper water column. The time-mean velocities (not shown) indicate that this feature arises from topographic blocking by the Kerguelen Plateau, which causes the time-mean streamlines to rotate with depth. This rotation of the mean flow results in a non-zero mean cross-stream velocity in the depth-invariant coordinate system used here.

The meridional isopycnal transport due to the Eulerian mean geostrophic flow (Figure 4.5) is fairly weak, corresponding to the small magnitude of $\langle \overline{v_g} \rangle$. Regardless of the choice of contour depth, the net meridional transports associated with this component were less than 1.1 x 10^6 m^2 s^{-1} at any depth in the upper water column. The uncertainty limits on this component of the MOC, derived by propagating the average errors associated with the mapped fields, indicates that the net geostrophic transport between 55.8°S and 52.3°S is statistically significant.

As Figure 4.6 shows, the mean wind stress pattern is predominantly along-stream, with some notable deviations around topographic features where the mean ACC flow becomes more meridional. The total Ekman contribution to the MOC (Figure 4.7)

shows net northward meridional transport in the Ekman layer across the range of the ACC, in line with our physical understanding of this region Rintoul et al. (2001). In the QuikSCAT satellite observations, increasing meridional transports with latitude, implying upwelling, are found over the entire range of the circumpolar region considered here. The NOC winds also show a positive meridional gradient over most of the region, with a small shift to negative values north of 51.4°S. The net difference across the circumpolar streamlines was 10.4 Sv for the QuikSCAT winds and 5.7 Sv for the NOC winds. In an Eulerian mean overturning cell, this divergence in the mixed layer would result in the same amount of net upwelling across the area, necessitating average vertical velocities of 2.9-5.3 x 10^{-5} cm s^{-1}. Both net Ekman transport values are comparable to the earlier calculation of net Ekman transport across the ACC by Karsten and Marshall (2002), which used NOC winds and the Hellerman and Rosenstein data set but time-mean geostrophic streamlines derived from altimetric measurements of sea surface height.

4.5.2 Eddy circulation

The meridional transport due to the standing eddies (Figure 4.8) is small for both choices of contour depth, with absolute values < 0.8 x 10^6 m^2 s^{-1} everywhere. Using the 1000 db time-mean streamlines produces northward transport in the shallowest layers and southward transport just above the maximum mixed layer depth. However, the uncertainty estimates, which are computed by propagating the average errors associated with the mapped fields, are larger than the net meridional transport everywhere for this component of the MOC. Thus the standing eddy circulation is indistinguishable from zero, for either choice of time-mean streamlines. This fact, combined with the relatively small contribution of the geostrophic Eulerian mean circulation to the total overturning circulation for most of the ACC region, indicates that our choice of streamwise coordinates is adequate for this data set.

Turning to the transient eddy contribution to the MOC, first consider the merid-

ional transport in the surface layer. The mean eddy thickness fluxes integrated above the mean mixed layer isopycnal along each streamline is shown in Figure 4.7. The error bars are obtained by assuming an uncertainty in the instantaneous velocities and pressures of 0.5 cm s^{-1} and 2 db, respectively, and propagating those through the calculations. Over most of the ACC the eddy activity results in a net southward transport in the mixed layer, in the direction of a down-gradient flux of buoyancy, with large southward transports found on the equatorward flank of the ACC, north of 51.6°S. The difference across the entire width of the ACC implies a net subduction of approximately 22±11 Sv due to eddy fluxes. This value is in line with the approximately 24 Sv of total near-surface eddy-induced downwelling determined by Karsten and Marshall (2002) using eddy fluxes parameterized from satellite sea surface height variability. However, in our results the subduction is strongly localized to a narrow region on the equatorward flank of the ACC, instead of fairly evenly distributed across the width of the ACC as Karsten and Marshall (2002) found.

The mean meridional isopycnal transport due to transient eddies (Figure 4.9), which is several times larger than either of the time-mean components of the transport, exhibits two prominent features. First, strong northward along-isopycnal fluxes are observed on the equatorward flank of the ACC between σ_θ 26.85 and 27.1 kg m^{-3}, the lightest part of the density range of Antarctic Intermediate Water (AAIW) in this region. These results indicate that eddy fluxes are responsible for a significant portion of the export of water in the AAIW density class equatorward out of the ACC. The maximum and mean mixed layer depths for each streamline (shown by the two gray lines in Figure 4.9) suggests that this water is transported northward both in the mixed layer and after it subducts. Just above this region of large northward eddy fluxes, significant southward eddy fluxes are found in the density range associated with Subantarctic Mode Water (SAMW), which agrees with the analysis of the residual overturning circulation in Karsten and Marshall (2002). The sense of the overturning implied by these fluxes agrees with our expectations of an eddy-induced

circulation associated with baroclinic instability and the slumping of tilted isopycnals. Second, in the waters denser than σ_θ 27.6 kg m^{-3}, the eddy transports are found to be predominantly southward. This isopycnal forms the approximate boundary between AAIW and Upper Circumpolar Deep Water, and thus these results demonstrate that eddy fluxes play an important role in transporting UCDW southward along tilted isopycnals towards the surface. In the isopycnal layers between these two regions, meridional eddy transports are weak and in general are not statistically different from zero.

To investigate the spatial distribution of the eddy fluxes, cumulative eddy transports integrated around the Southern Ocean starting from 0°E along several streamlines are given in Figure 4.10 for two different isopycnal layers that are associated with significant eddy thickness fluxes. In the layer centered on σ_θ 27.01 kg m^{-3}, the majority of the total northward eddy transport arises in the southeast Pacific, between about 150°W and Drake Passage. Given that this isopycnal is within the density range of AAIW, this finding is particularly interesting because there has been a long-standing disagreement as to whether AAIW is primarily formed in the Southeast Pacific or across the whole longitude range of the ACC. This analysis suggests that the export of AAIW due to eddy fluxes occurs predominantly in the Southeast Pacific. In the σ_θ 27.67 kg m^{-3} layer, a pronounced staircase pattern is found in the integrated eddy flux, especially for the more northern streamlines. Large changes in total eddy transport in this isopycnal layer are seen downstream of the Kerguelen Plateau, Macquarie Ridge, Pacific-Antarctic Ridge, and Drake Passage. A recent study by Abernathey and Cessi (2014) used both an idealized numerical model and a quasi-geostrophic analytical model to show that transient cross-stream eddy fluxes are enhanced downstream of topographic features due to the effects of the standing waves induced by those features. Thompson and Naveira Garabato (2014) came to a similar conclusion using a realistic high-resolution model of the Southern Ocean. Such dynamics appear to provide a likely explanation for the results of our observational

analysis.

4.5.3 Residual mean circulation

Summing the Eulerian mean circulation (using NOC winds) and the transient eddy circulation leads to an estimate of the residual mean overturning circulation in the upper part of the ACC. The standing eddy circulation has been excluded because it is not statistically different from zero anywhere. In the surface layer (Figure 4.7), these components nearly balance at the equatorward flank of the ACC, with a small southward residual transport of 3.2±10 Sv, where the error bars come from the transient eddy estimate. Therefore, in this region we observe a leading-order balance between the wind-driven circulation and that induced by the eddies, in agreement with the model results of Karsten et al. (2002). Over much of the rest of the ACC, however, the transient eddy transport is a factor of two smaller than the Ekman transport, resulting in 13.3 Sv to the north at the poleward flank of the ACC and even larger northward transports between 53.4 and 52.2°S. This result suggests that buoyancy forcing plays a leading-order role south of 52.2°S. The net difference in the northward residual transport across the two sides of the ACC is found to be 16.5 Sv, which corresponds to the subduction associated with the Antarctic Convergence. As Figure 4.7 shows, this subduction is occurring in a narrow region on the equatorward side of the ACC, between 52.2 and 51.5°S. Outside of the surface layer, the meridional transport due to transient eddies given in Figure 4.9 dominates the total transport, although the uncertainties in the estimated eddy fluxes precludes a quantitative estimate of the overturning streamfunction itself. While the eddy transport can be quite localized in space, as shown in Figure 4.10, the Ekman transport is much more uniformly distributed across the whole of the ACC (Figure 4.6). This finding supports the idea that the regions where the winds impart available potential energy to the ocean are broad and spread along the whole path of the ACC, but the regions where this energy is released through baroclinic instability are very localized in space, primarily to areas

just downstream of bathymetric features (Thompson and Naveira Garabato, 2014).

4.6 Conclusions

This study attempts to use observations from the Argo array of profiling floats to compute a data-based estimate of the Southern Ocean MOC, including direct estimates of the subsurface eddy-induced meridional transport. Zonally-averaging along streamlines of the time-mean geostrophic flow at a constant depth was found to provide an adequate method for computing a zonal-mean estimate of the MOC. Transient eddies were seen to play an important role in driving the overturning circulation in the Southern Ocean, as expected based on the numerous theoretical and numerical models of the region that have been advanced over the past few decades. Transient effects were found to be enhanced downstream of major topographic features, as observed in numerical models. However, the methods used in this study to compute eddy transports from Argo data require additional validation using other observations and numerical models in order to verify that this data set can sufficiently resolve eddy flux fields in this region. Future work will seek to rigorously test these techniques, which have the potential to dramatically improve our ability to measure eddy fluxes throughout the global upper ocean. In addition, expanding the data set used here to include additional data collected since 2010 will help refine these estimates by reducing the uncertainties associated with the calculations of transient eddy fluxes. The study presented here serves as an excellent foundation for this research, which should help to further our understanding of the mechanisms that control the southern branch of the global meridional overturning circulation.

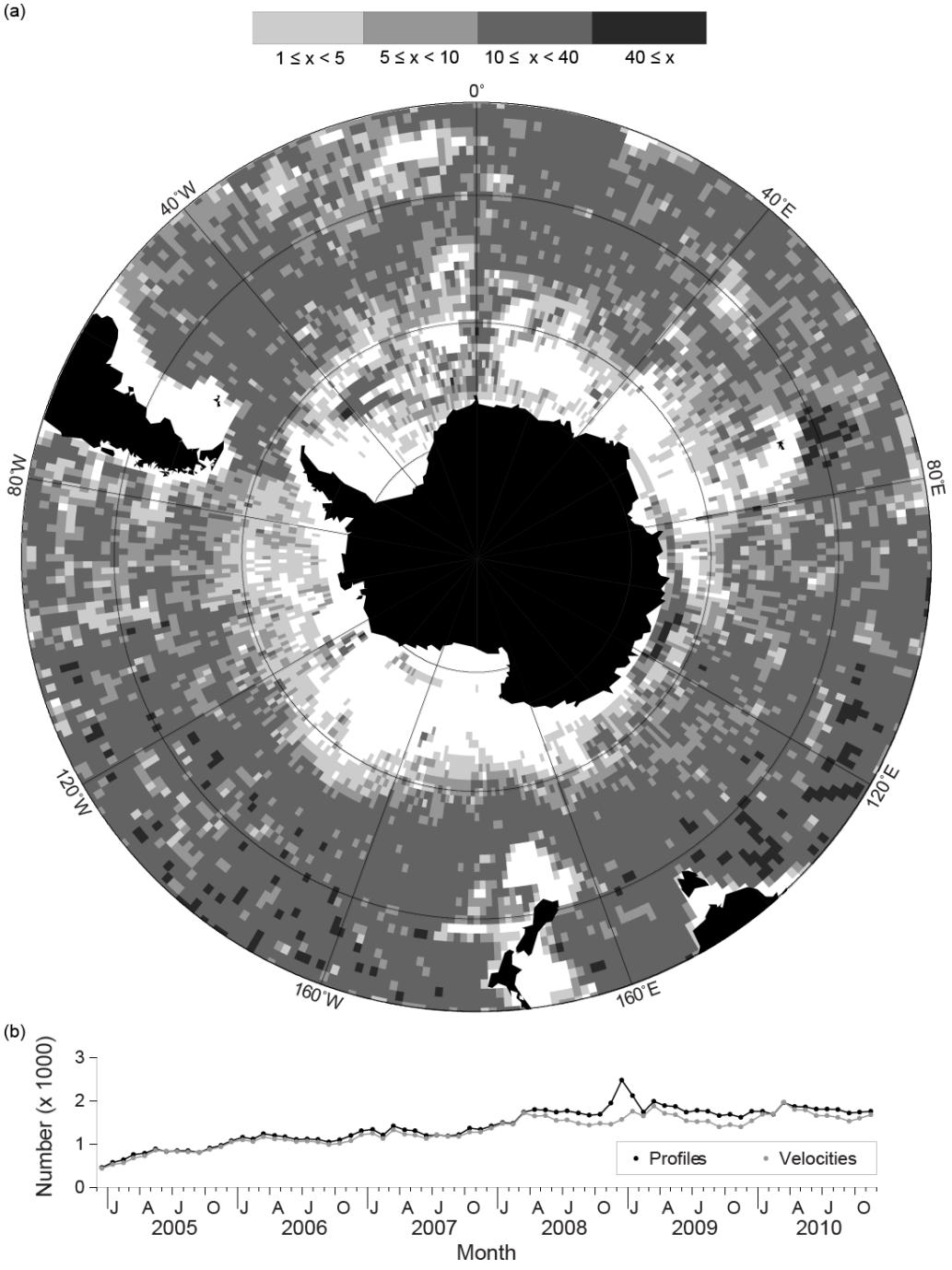

Figure 4.1: (a) Spatial distribution of all profile data south of 35°S, shown as the number of profiles in each 1° x 1° box and (b) temporal distribution of both profile and velocity data, shown as the number of data in each month during the study period. The spatial distribution of the velocity data is very similar to (a).

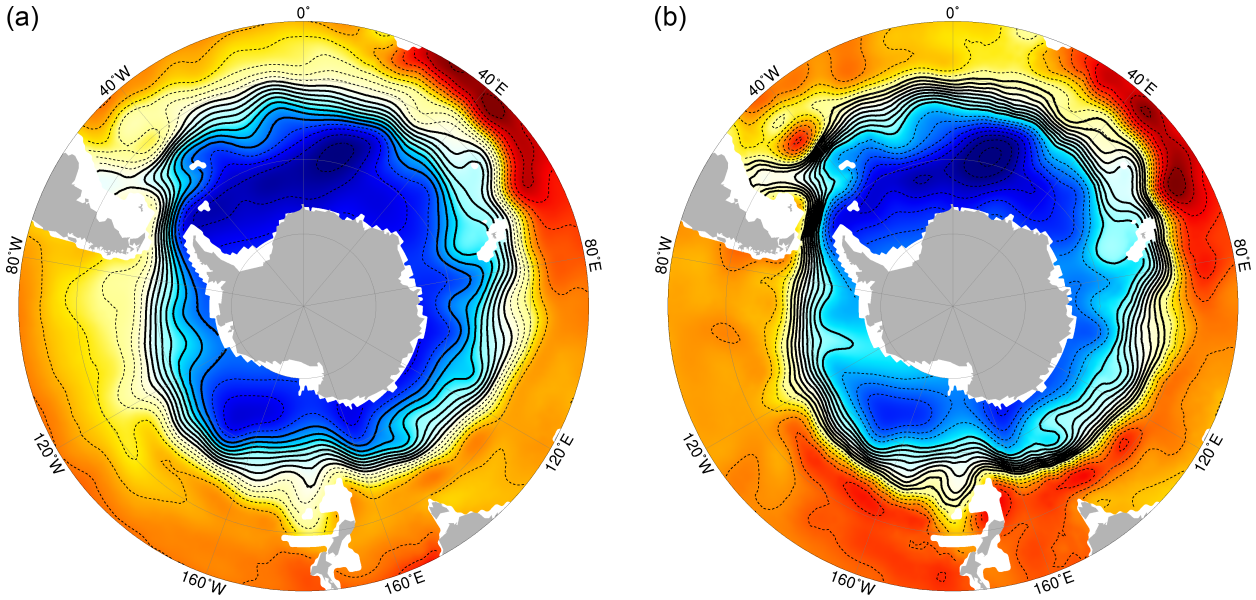

Figure 4.2: Time-mean absolute geostrophic streamfunction south of 35°S at (a) 5 db and (b) 1000 db. The contour interval is 12.5 dyn cm in (a) and 5 dyn cm in (b), where 1 dyn cm = 10 m^2 s^{-2}. The solid contours are the circumpolar streamlines used for zonally averaging, and at each pressure level the streamlines have been normalized so that the most poleward circumpolar streamline is 0 dyn cm. For each plot, the colors span the full range of streamfunction values in that plot and show highs (lows) in reds (blues), which are associated with anticyclonic (cyclonic) flows.

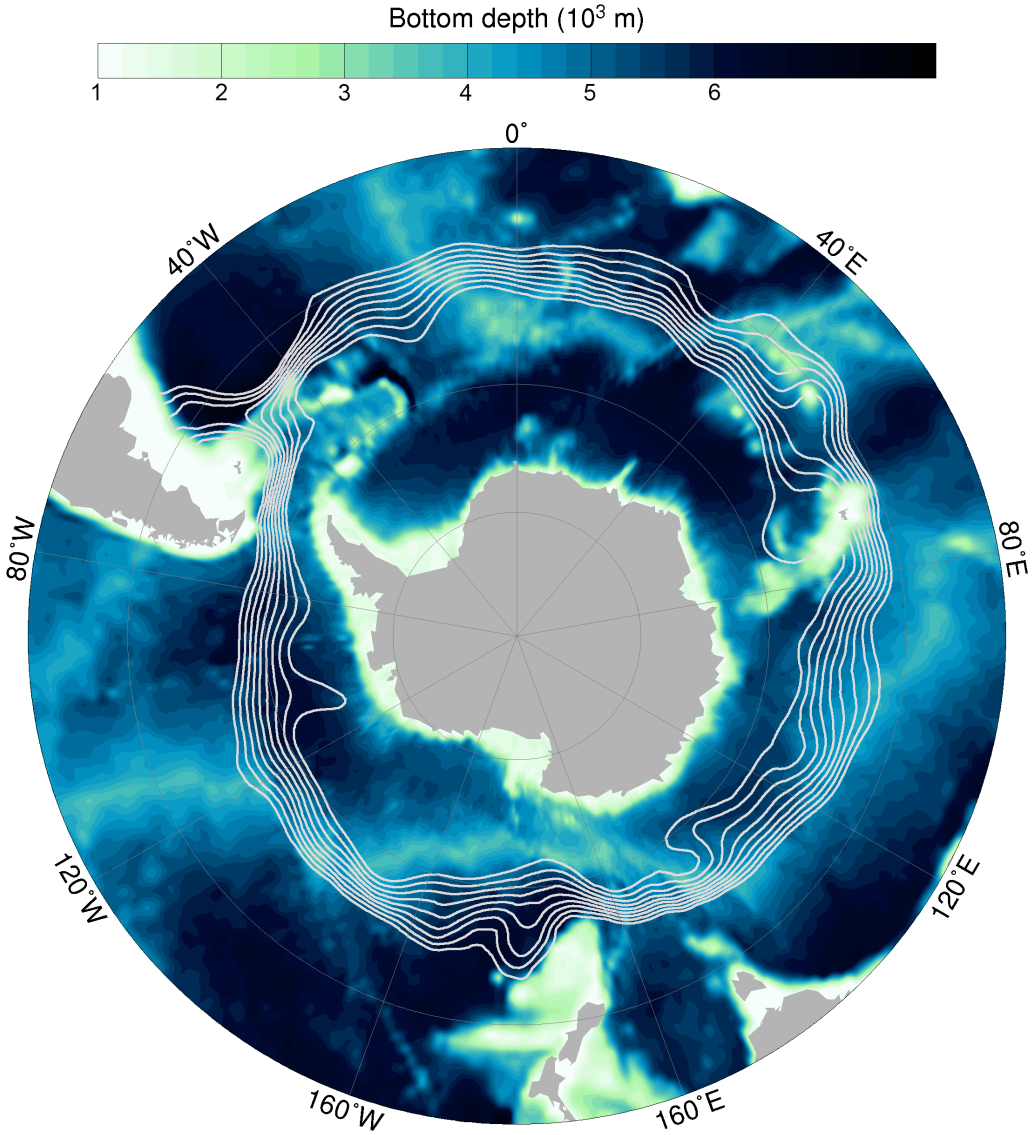

Figure 4.3: Bathymetry of the Southern Ocean computed in 1° grid boxes using ETOPO1.0 relief data Amante and Eakins (2009). The white contours are the circumpolar streamlines of the time-mean geostrophic flow at 1000 db.

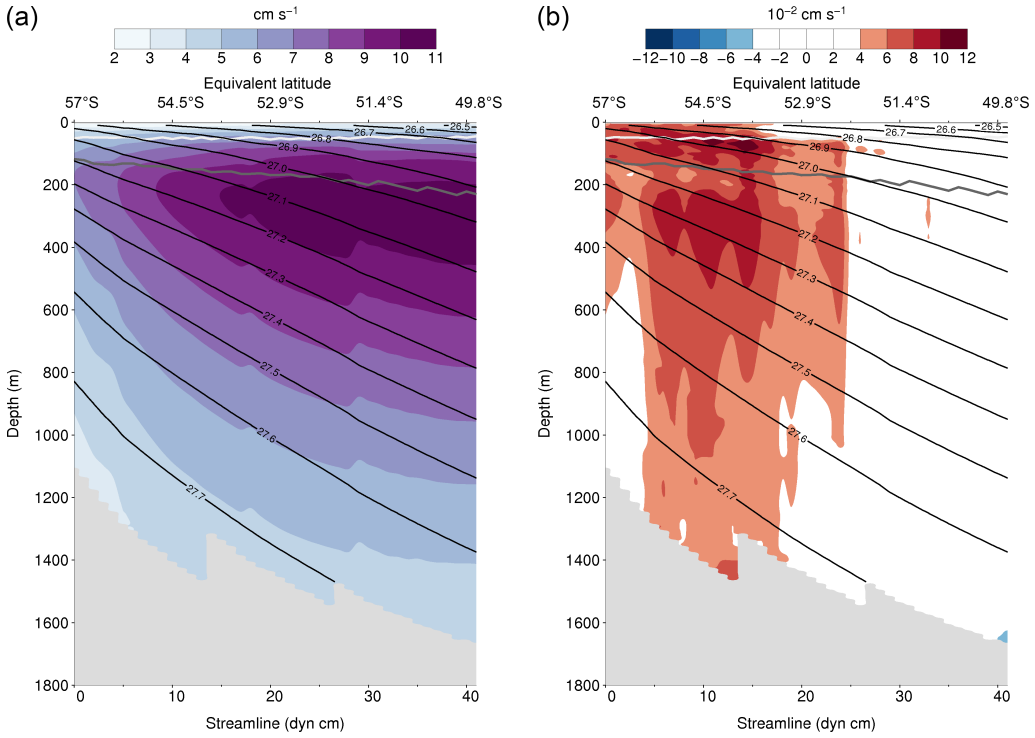

Figure 4.4: Time- and zonal-mean velocity computed using streamlines from the 1000 db contour depth, along with contours of mean σ_θ in black. Zonal velocities are shown in (a) and meridional velocities in (b). The thick dark gray (light gray) line gives the maximum (median) mixed layer depth found along each streamline in the time-mean. At the bottom of the region, the jagged contours arise from the isopycnal averaging process because the maximum isopycnal layer that is fully resolved in the depth range of the Argo floats varies with streamline location.

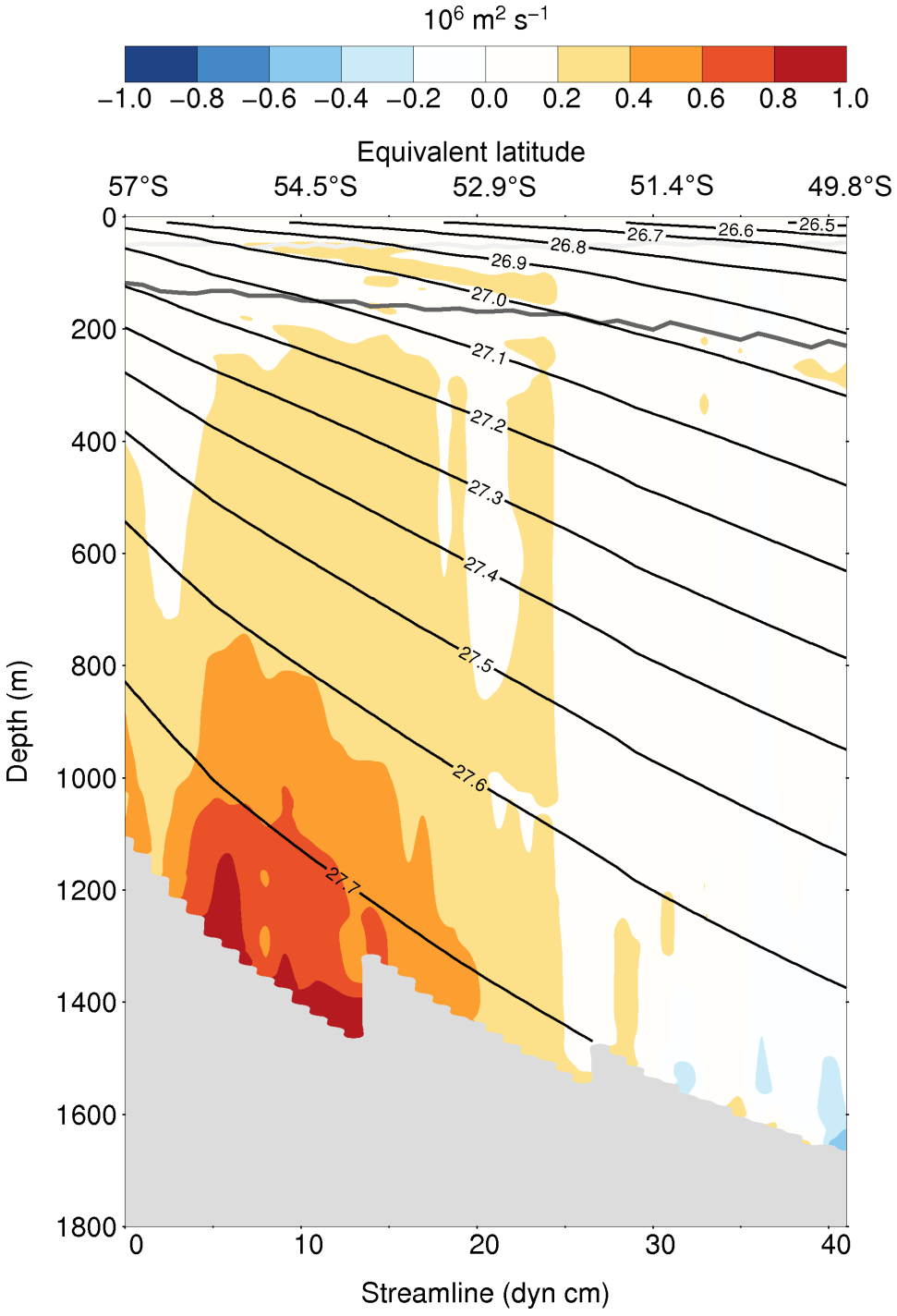

Figure 4.5: Geostrophic Eulerian mean component of meridional overturning circulation given as the meridional transport $\langle \overline{v_g} \rangle \langle \overline{h} \rangle$.

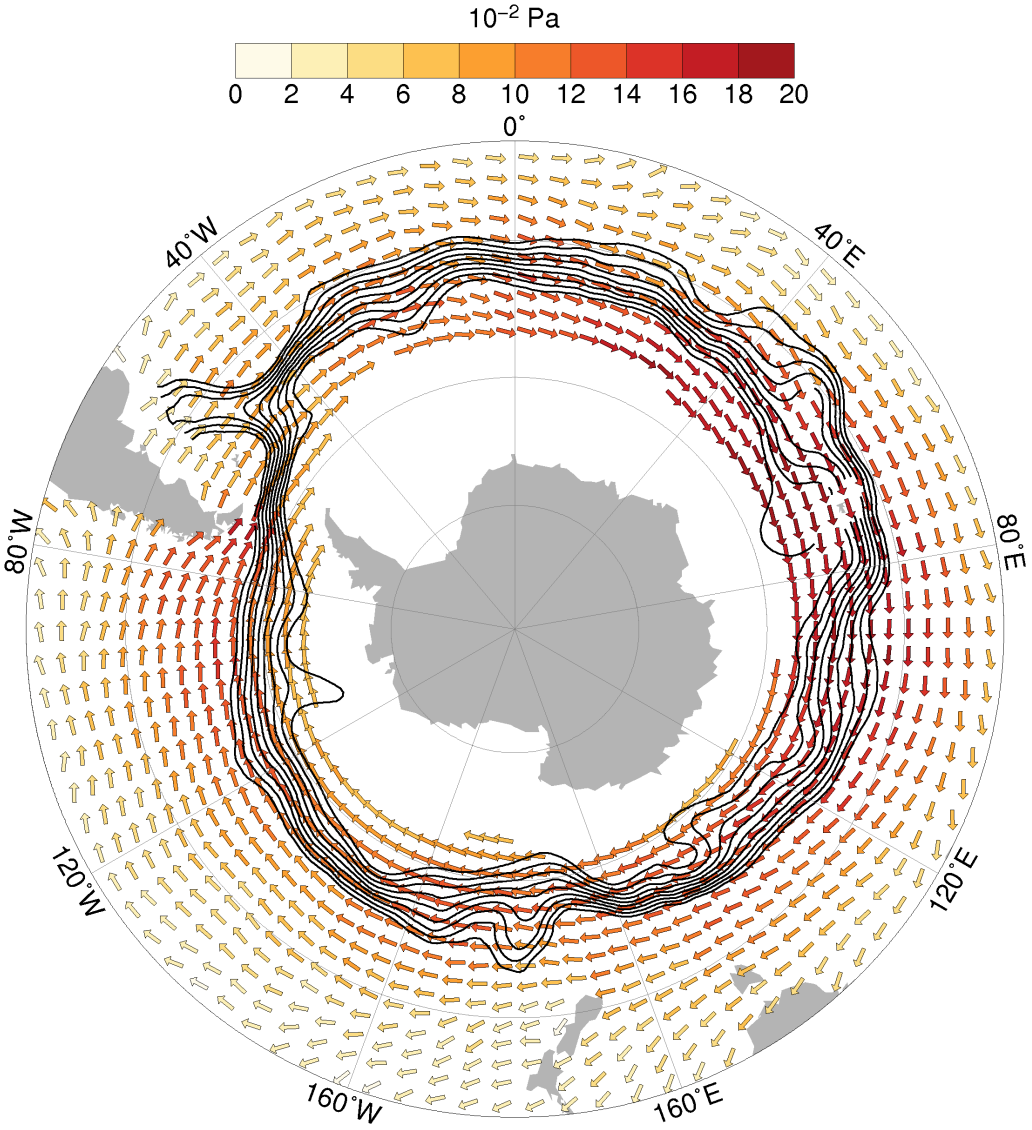

Figure 4.6: Time-mean wind stress in the Southern Ocean computed from NOC winds. The magnitude of the wind stress is indicated by the color of each arrow. The black contours show the time-mean geostrophic streamlines using the 1000 db contour depth.

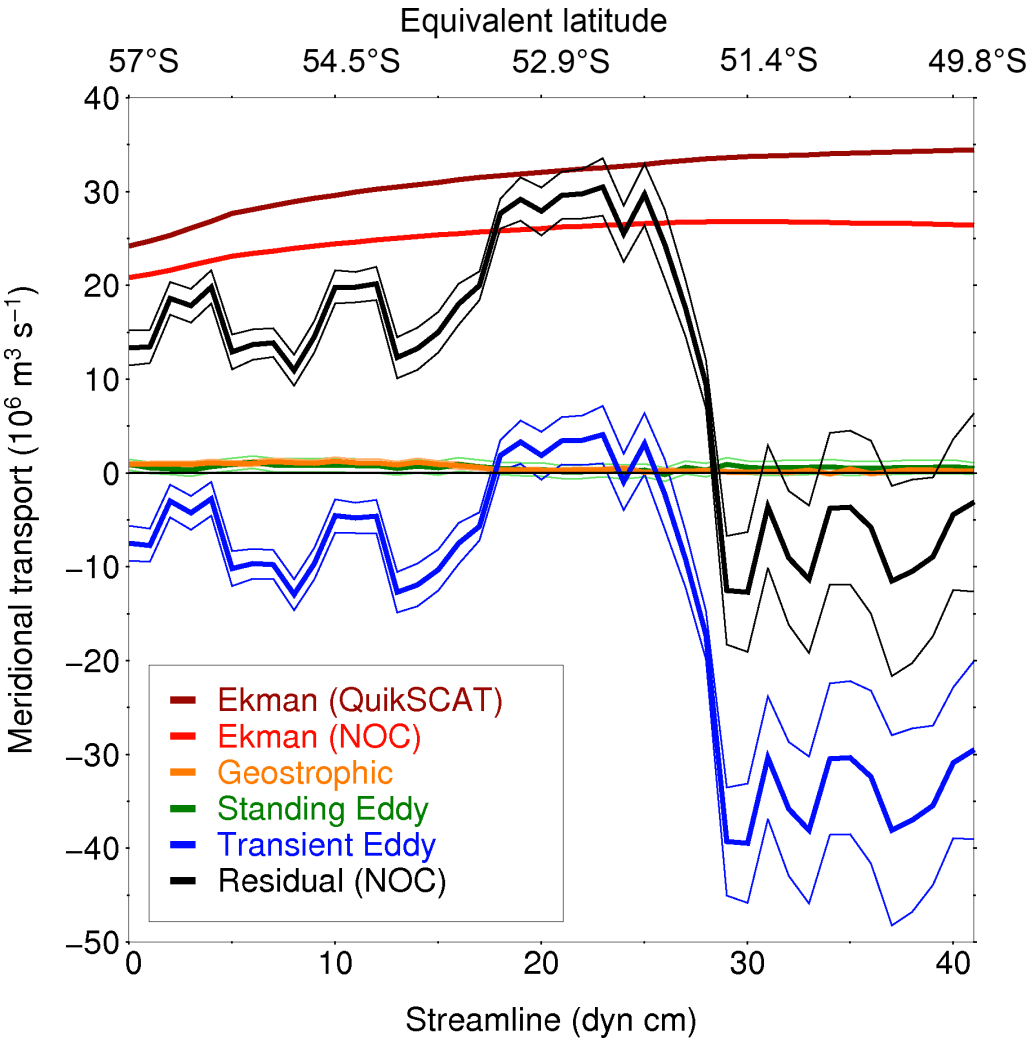

Figure 4.7: The components of the mean meridional transport in the layer from the surface to the mean mixed layer density at each streamline.

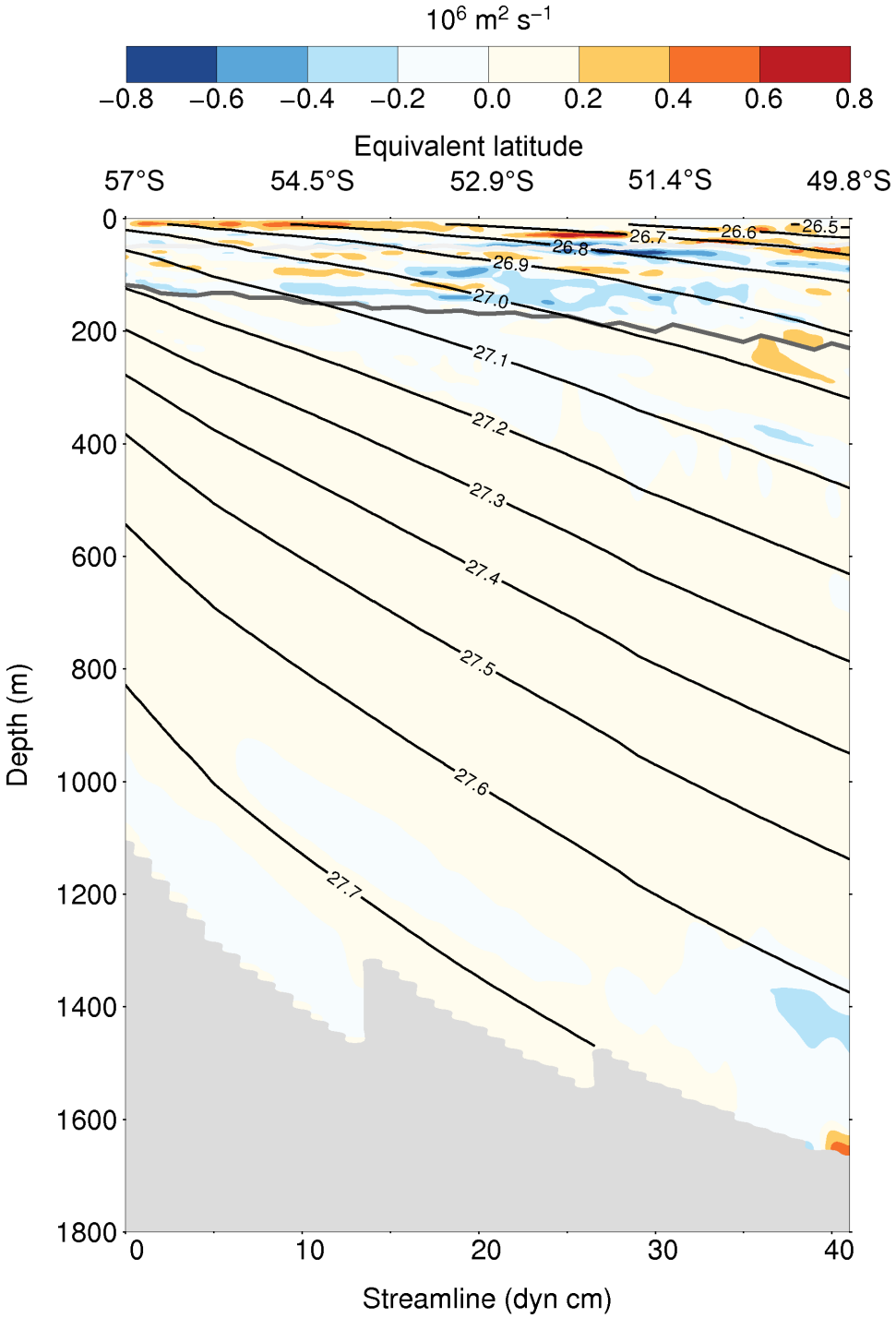

Figure 4.8: Standing eddy component of meridional overturning circulation given as the meridional transport $\langle \overline{v}^{+} \overline{h}^{+} \rangle$.

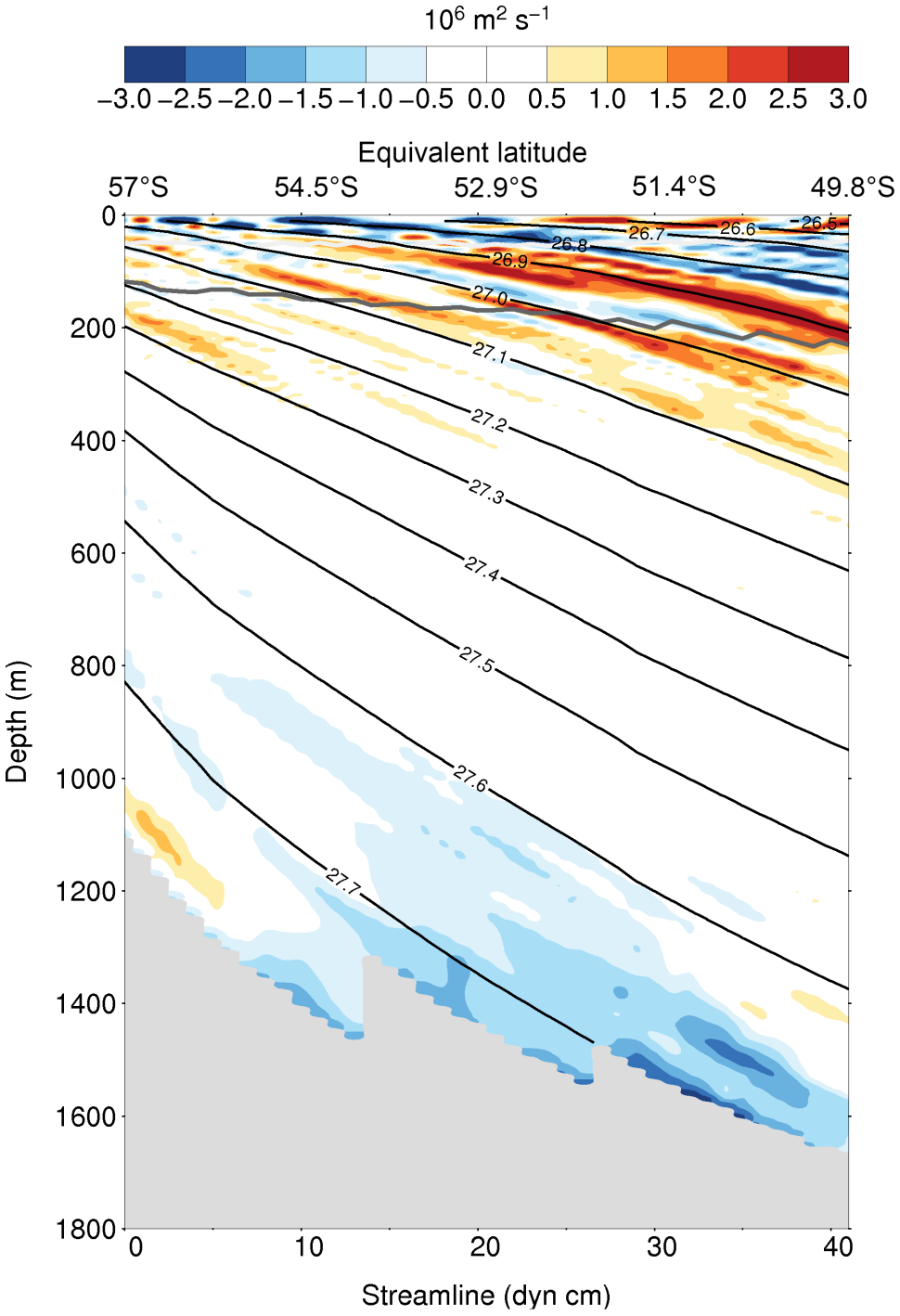

Figure 4.9: Transient eddy component of meridional overturning circulation given as the meridional transport $\langle \overline{v'h'} \rangle$. White areas indicate values not statistically different from zero.

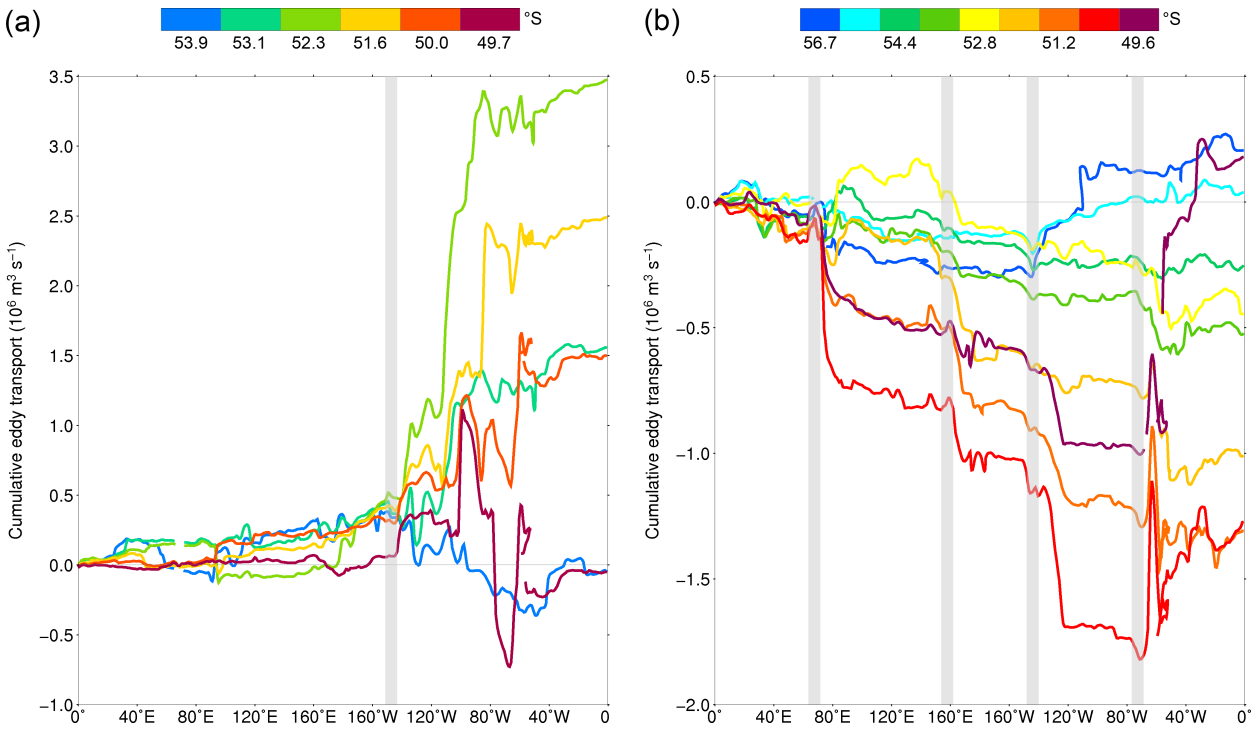

Figure 4.10: Cumulative zonally-integrated meridional eddy transport for selected streamlines in the (a) 27.01 σ_θ layer, within the AAIW water mass and (b) 27.67 σ_θ layer, within the UCDW water mass. The gray regions highlight the longitude range where the time-mean streamlines pass over major bathymetric features. The single region in (a) shows the location of the Pacific-Antarctic Ridge, and the four regions in (b) indicate, from left to right, the Kerguelen Plateau, the Macquarie Ridge, the Pacific-Antarctic Ridge, and the Scotia sill just past Drake Passage.

Chapter 5
CONCLUSIONS

The overall goal of this dissertation is to further our understanding of the forces that shape the large-scale circulation of the ocean using observations from the Argo array of autonomous profiling floats. The temperature, salinity, and velocity data provided by these instruments were used to quantitatively estimate the large-scale circulation of the upper 2000 db of the global ocean. The resulting velocity maps formed the foundation for analyses of two different aspects of the large-scale circulation, the wind-driven circulation and the meridional overturning circulation in the Southern Ocean. By investigating these components of the large-scale circulation, this work aims to help advance our knowledge of the role that ocean circulation plays in the global climate system and in the global marine ecosystem.

In Chapter 2, a new method for objectively analyzing scattered data was developed and tested. This technique uses an iterative generalized least squares procedure together with standard objective analysis to map fields with multiple spatial and temporal scales and is particularly advantageous when the statistics of the field are not known a priori. In addition, this work highlighted the use of spherical radial basis functions for fitting the large-scale signal in basin- to global-scale domains. The method was tested using simulated dynamic height data and high-resolution model output and then applied to the global Argo data set in order to map absolute geostrophic velocity, temperature, and salinity in the upper 2000 db of the world ocean. The resulting estimate of the large-scale circulation has a number of advantages, including no ad hoc assumption regarding the reference velocity and significant increases in the spatial and temporal resolution of the data.

The study presented in Chapter 3 used these Argo-derived velocity, temperature, and salinity estimates, together with satellite observations of wind stress, to assess one of the most basic models of the wind-driven circulation, Sverdrup balance. Using two different approaches to evaluating this theoretical relationship from data, Sverdrup balance was found to accurately predict the meridional geostrophic transport in large portions of the global ocean, primarily the subtropical and tropical oceans away from boundaries. Possible reasons for why this relation does not appear to hold in other areas, such as the high latitude oceans and western boundary current regions, were discussed. Overall, this study demonstrated that although Sverdrup balance provides a useful starting point for a description of the large-scale wind-driven circulation, it is not applicable everywhere.

Chapter 4 focused on using the velocity, temperature and salinity maps constructed from Argo data to examine how different aspects of the circulation in the Southern Ocean interact to produce the southern branch of the global meridional overturning circulation. The mean circulation was determined from the Argo-derived gridded estimates and wind stress observations. The individual Argo data were also used to directly estimate eddy fluxes of isopycnal thickness, which are thought to play a leading-order role in the dynamics of the Antarctic Circumpolar Current and the resulting meridional overturning circulation, and further work to validate and verify the techniques used to derive these fluxes is underway. By adopting a streamwise coordinate system, this study found significant cross-stream eddy fluxes in the time- and zonal-mean transport, which generally corresponded to expectations based on the leading theoretical model of the overturning circulation in this region. In addition, eddy transports were seen to be enhanced downstream of topographic features, as observed in both analytical and high-resolution numerical models.

In addition to the scientific results presented here, this dissertation demonstrates that the observations of temperature, salinity, and velocity collected by the Argo array of profiling floats can be used to quantitatively estimate the large-scale circulation of

the upper 2000 db of the global ocean. In addition to further analyses of numerous different features of the large-scale circulation, these purely data-based estimates may also be useful for model validation and initialization. As long as the Argo array is maintained, these maps of temperature, salinity, and absolute geostrophic velocity can be continually improved and expanded to cover a longer time period. This work also shows that data from profiling floats have a great deal of potential for accurately estimating eddy fluxes of mass, heat, and freshwater, which could lead to significant insight into many aspects of ocean dynamics.

BIBLIOGRAPHY

Abernathey, R. and P. Cessi, 2014: Topographic enhancement of eddy efficiency in baroclinic equilibration. *J. Phys. Oceanogr.*, **44 (8)**, 2107–2126, doi:10.1175/JPO-D-14-0014.1.

Amante, C. and B. W. Eakins, 2009: ETOPO1 1 Arc-Minute Global Relief Model: Procedures, Data Sources and Analysis. NOAA Tech. Memo. NESDIS NGDC-24, 19 pp.

Andrews, D. and M. McIntyre, 1976: Planetary waves in horizontal and vertical shear - Generalized Eliassen-Palm relation and mean zonal acceleration. *J. Atmos. Sci.*, **33 (11)**, 2031–2048, doi:10.1175/1520-0469(1976)033⟨2031:PWIHAV⟩2.0.CO;2.

Batchelor, G. K., 1970: *The Theory of Homogeneous Turbulence*. Cambridge University Press, 197 pp.

Bleck, R., 2002: An oceanic general circulation model framed in hybrid isopycnic-Cartesian coordinates. *Ocean Model.*, **4 (1)**, 55–88.

Bretherton, F. P., R. E. Davis, and C. B. Fandry, 1976: Technique for objective analysis and design of oceanographic experiments applied to Mode-73. *Deep-Sea Res.*, **23 (7)**, 559–582.

Bretherton, F. P. and J. C. McWilliams, 1980: Estimations from irregular arrays. *Rev. Geophys.*, **18 (4)**, 789–812, doi:10.1029/RG018i004p00789.

Buhmann, M. D., 2003: *Radial Basis Functions: Theory and Implementations*. Cambridge University Press, 259 pp.

Caldeira, K. and P. Duffy, 2000: The role of the Southern Ocean in uptake and storage of anthropogenic carbon dioxide. *Science*, **287 (5453)**, 620–622.

Chelton, D. B., R. A. DeSzoeke, M. G. Schlax, K. E. Naggar, and N. Siwertz, 1998: Geographical variability of the first baroclinic Rossby radius of deformation. *J. Phys. Oceanogr.*, **28 (3)**, 433–460.

Chiles, J.-P. and P. Delfiner, 1999: *Geostatistics: Modeling Spatial Uncertainty.* Wiley, 695 pp.

Chinn, B. S. and S. T. Gille, 2007: Estimating eddy heat flux from float data in the North Atlantic: The impact of temporal sampling interval. *J. Atmos. Oceanic Technol.*, **24 (5)**, 923–934, doi:10.1175/JTECH2057.1.

Cressie, N., 1985: Fitting variogram models by weighted least squares. *Math. Geol.*, **17 (5)**, 563–586, doi:10.1007/BF01032109.

Cressie, N. A. C., 1993: *Statistics for Spatial Data.* Rev. ed., Wiley, 900 pp.

Danabasoglu, G. and J. C. McWilliams, 1995: Sensitivity of the global ocean circulation to parameterizations of mesoscale tracer transports. *J. Climate*, **8 (12)**, 2967–2987, doi:10.1175/1520-0442(1995)0082.0.CO;2.

Davis, R. E., 1985: Objective mapping by least-squares fitting. *J. Geophys. Res.*, **90 (NC3)**, 4773–4777.

Davis, R. E., 1998: Preliminary results from directly measuring middepth circulation in the tropical and South Pacific. *J. Geophys. Res.*, **103 (C11)**, 24 619–24 639.

Davis, R. E., 2005: Intermediate-depth circulation of the Indian and South Pacific Oceans measured by autonomous floats. *J. Phys. Oceanogr.*, **35 (5)**, 683–707.

Deacon, G., 1937: The hydrology of the Southern Ocean. *Discov. Rep.*, **15**, 1–124.

del Pino, G., 1989: The unifying role of iterative generalized least squares in statistical algorithms. *Stat. Sci.*, **4 (4)**, 394–403.

deSzoeke, R. and M. Levine, 1981: The advective flux of heat by mean geostrophic motions in the Southern Ocean. *Deep-Sea Res., Part A*, **28 (10)**, 1057–1085, doi:10.1016/0198-0149(81)90048-0.

Döös, K. and D. Webb, 1994: The Deacon cell and the other meridional cells of the Southern Ocean. *J. Phys. Oceanogr.*, **24 (2)**, 429–442, doi:10.1175/1520-0485(1994)0242.0.CO;2.

Fasshauer, G., 2007: *Meshfree Approximation Methods with MATLAB*. World Scientific, 500 pp.

Fasshauer, G. E. and L. L. Schumaker, 1998: Scattered data fitting on the sphere. *Mathematical Methods for Curves and Surfaces II: Lillehammer, 1997*, M. Dæhlen, T. Lyche, and L. L. Schumaker, Eds., Vanderbilt University Press.

Franke, R., 1982: Scattered data interpolation: Tests of some methods. *Math. Comp.*, **38 (157)**, 181–200, doi:10.2307/2007474.

Frankignoul, C., N. Sennechael, Y.-O. Kwon, and M. A. Alexander, 2011: Influence of the meridional shifts of the Kuroshio and the Oyashio extensions on the atmospheric circulation. *J. Climate*, **24 (3)**, 762–777, doi:10.1175/2010JCLI3731.1.

Freeden, W., T. Gervens, and M. Schreiner, 1998: Spherical radial basis fucntions. *Constructive Approximation on the Sphere with Applications to Geomathematics*, Clarendon Press.

Fritsch, F. N. and R. E. Carlson, 1980: Monotone piecewise cubic interpolation. *SIAM J. Numer. Anal.*, **17**, 238–246.

Ganachaud, A., 2003: Large-scale mass transports, water mass formation, and diffusivities estimated from World Ocean Circulation Experiment (WOCE) hydrographic data. *J. Geophys. Res.*, **108 (C7)**, 3213, doi:10.1029/2002JC001565.

Ganachaud, A. and C. Wunsch, 2000: Improved estimates of global ocean circulation, heat transport and mixing from hydrographic data. *Nature*, **408 (6811)**, 453–457.

Gille, S. T., 2003a: Float observations of the Southern Ocean. Part I: Estimating mean fields, bottom velocities, and topographic steering. *J. Phys. Oceanogr.*, **33 (6)**, 1167–1181.

Gille, S. T., 2003b: Float observations of the Southern Ocean. Part II: Eddy fluxes. *J. Phys. Oceanogr.*, **33 (6)**, 1167–1181, doi:10.1175/1520-0485(2003)033⟨1167:FOOTSO⟩2.0.CO;2.

Goldstein, H., 1986: Multilevel mixed linear model analysis using iterative generalized least squares. *Biometrika*, **73 (1)**, 43–56.

Goldstein, H., 2011: *Multilevel Statistical Models*. 4th ed., Wiley, 358 pp.

Gray, A. R. and S. C. Riser, 2014: A global analysis of Sverdrup balance using absolute geostrophic velocities from Argo. *J. Phys. Oceanogr.*, **44**, 1213–1229, doi:10.1175/JPO-D-12-0206.1.

Gray, A. R. and S. C. Riser, 2014, submitted: A method for multiscale optimal analysis with application to Argo data. *J. Geophys. Res.*

Gruber, N. and J. L. Sarmiento, 1997: Global patterns of marine nitrogen fixation and denitrification. *Global Biogeochem. Cycles*, **11 (2)**, 235–266, doi: 10.1029/97GB00077.

Hallberg, R. and A. Gnanadesikan, 2001: An exploration of the role of transient eddies in determining the transport of a zonally reentrant current. *J. Phys. Oceanogr.*, **31**, 3312–3330, doi:10.1175/1520-0485(2001)031⟨3312:AEOTRO⟩2.0.CO;2.

Hallberg, R. and A. Gnanadesikan, 2006: The role of eddies in determining the structure and response of the wind-driven Southern Hemisphere overturning: Results from the Modeling Eddies in the Southern Ocean. *J. Phys. Oceanogr.*, **36 (12)**, 2232–2252, doi:10.1175/JPO2980.1.

Hardy, R. L., 1990: Theory and applications of the multiquadric-biharmonic method: 20 years of discovery 1968-1988. *Comput. Math. Appl.*, **19 (8-9)**, 163–208, doi:10.1016/0898-1221(90)90272-L.

Hardy, R. L. and W. M. Göpfert, 1975: Least squares prediction of gravity anomalies, geoidal undulations, and deflections of the vertical with multiquadric harmonic functions. *Geophys. Res. Lett.*, **2 (10)**, 423–426.

Hartigan, J. A., 1975: *Clustering Algorithms*. Wiley, New York, 351 pp.

Hartmann, D. L., 1994: The ocean general circulation and climate. *Global Physical Climatology*, Academic Press, International Geophysics Series, Vol. 56, 171–203.

Hautala, S. L., D. H. Roemmich, and W. J. Schmitz, 1994: Is the North Pacific in Sverdrup balance along 24°N? *J. Geophys. Res.*, **99 (C8)**, 16 041–16 052.

Holte, J. and L. Talley, 2009: A new algorithm for finding mixed layer depths with applications to Argo data and Subantarctic Mode Water formation. *J. Atmos. Oceanic Technol.*, **26 (9)**, 1920–1939.

Ivchenko, V., K. Richards, and D. Stevens, 1996: The dynamics of the Antarctic Circumpolar Current. *J. Phys. Oceanogr.*, **26 (5)**, 753–774, doi: 10.1175/1520-0485(1996)0262.0.CO;2.

Jackett, D. R. and T. J. McDougall, 1997: A neutral density variable for the world's oceans. *J. Phys. Oceanogr.*, **27**, 237–263, doi:{10.1175/1520-0485(1997) 0272.0.CO;2}.

Johnson, G. and H. Bryden, 1989: On the size of the Antarctic Circumpolar Current. *Deep Sea Res., Part A*, **36 (1)**, 39–53, doi:10.1016/0198-0149(89) 90017-4.

Josey, S., E. Kent, and P. Taylor, 2002: Wind stress forcing of the ocean in the SOC climatology: Comparisons with the NCEP-NCAR, ECMWF, UWM/COADS, and Hellerman and Rosenstein Datasets. *J. Phys. Oceanogr.*, **32 (7)**, 1993–2019, doi:10.1175/1520-0485(2002)032⟨1993:WSFOTO⟩2.0.CO;2.

Kariya, T. and H. Kurata, 2004: *Generalized least squares*. Wiley, 289 pp.

Karsten, R., H. Jones, and J. Marshall, 2002: The role of eddy transfer in setting the stratification and transport of a circumpolar current. *J. Phys. Oceanogr.*, **32 (1)**, 39–55, doi:10.1175/1520-0485(2002)0322.0.CO;2.

Karsten, R. and J. Marshall, 2002: Constructing the residual circulation of the ACC from observations. *J. Phys. Oceanogr.*, **32 (12)**, 3315–3327, doi:10.1175/ 1520-0485(2002)0322.0.CO;2.

Katsumata, K., B. M. Sloyan, and S. Masuda, 2013: Diapycnal and isopycnal transports in the Southern Ocean estimated by a box inverse model. *J. Phys. Oceanogr.*, **43 (11)**, 2270–2287, doi:10.1175/JPO-D-12-0210.1.

Katsumata, K. and H. Yoshinari, 2010: Uncertainties in global mapping of Argo drift data at the parking level. *J. Oceanogr.*, **66 (4)**, 553–569.

Keffer, T. and G. Holloway, 1988: Estimating Southern Ocean eddy flux of heat and salt from satellite altimetry. *Nature*, **332 (6165)**, 624–626, doi:{10.1038/ 332624a0}.

Key, R., et al., 2004: A global ocean carbon climatology: Results from Global Data Analysis Project (GLODAP). *Global Biogeochem. Cycles*, **18 (4)**, doi: 10.1029/2004GB002247.

Klees, R., R. Tenzer, I. Prutkin, and T. Wittwer, 2008: A data-driven approach to local gravity field modelling using spherical radial basis functions. *J. Geodesy*, **82 (8)**, 457–471, doi:10.1007/s00190-007-0196-3.

Kroese, D. P. and Z. I. Botev, 2013: Spatial process generation. *arXiv preprint arXiv:1308.0399*.

Kunze, E., E. Firing, J. M. Hummon, T. K. Chereskin, and A. M. Thurnherr, 2006: Global abyssal mixing inferred from lowered ADCP shear and CTD strain profiles. *J. Phys. Oceanogr.*, **36 (8)**, 1553–1576, doi:10.1175/JPO2926.1.

Kwon, Y. O. and S. C. Riser, 2004: North Atlantic Subtropical Mode Water: A history of ocean-atmosphere interaction 1961-2000. *Geophys. Res. Lett.*, **31 (19)**, doi:10.1029/2004GL021116.

Le Quéré, C., et al., 2007: Saturation of the Southern Ocean CO_2 sink due to recent climate change. *Science*, **316 (5832)**, 1735–8, doi:10.1126/science.1136188.

Ledwell, J., A. Watson, and C. Law, 1998: Mixing of a tracer in the pycnocline. *J. Geophys. Res.*, **103 (C10)**, 21 499–21 529, doi:10.1029/98JC01738.

Ledwell, J. R., L. C. St. Laurent, J. B. Girton, and J. M. Toole, 2011: Diapycnal mixing in the Antarctic Circumpolar Current. *J. Phys. Oceanogr.*, **41 (1)**, 241–246, doi:10.1175/2010JPO4557.1.

Leetmaa, A., P. Niiler, and H. Stommel, 1977: Does the Sverdrup relation account for the mid-Atlantic circulation? *J. Mar. Res.*, **35 (1)**, 1–10.

LeTraon, P. Y., 1990: A method for optimal analysis of fields with spatially-variable mean. *J. Geophys. Res.*, **95 (C8)**, 13 543–13 547.

Liu, W. T., W. Tang, and X. Xie, 2008: Wind power distribution over the ocean. *Geophys. Res. Lett.*, **35**, L13 808, doi:doi:10.1029/2008GL034172.

Lozier, M. S., M. S. McCartney, and W. B. Owens, 1994: Anomalous anomalies in averaged hydrographic data. *J. Phys. Oceanogr.*, **24 (12)**, 2624–2638.

Lumpkin, R. and K. Speer, 2007: Global ocean meridional overturning. *J. Phys. Oceanogr.*, **37 (10)**, 2550–2562, doi:10.1175/JPO3130.1.

Luyten, J. R., J. Pedlosky, and H. Stommel, 1983: The ventilated thermocline. *J. Phys. Oceanogr.*, **13 (2)**, 292–309.

MacCready, P. and P. Rhines, 2001: Meridional transport across a zonal channel: Topographic localization. *J. Phys. Oceanogr.*, **31 (6)**, 1427–1439, doi: 10.1175/1520-0485(2001)0312.0.CO;2.

Macdonald, A. M., 1998: The global ocean circulation: A hydrographic estimate and regional analysis. *Prog. Oceanogr.*, **41 (3)**, 281–382.

Macdonald, A. M. and C. Wunsch, 1996: An estimate of global ocean circulation and heat fluxes. *Nature*, **382 (6590)**, 436–439.

MacRobert, T. M. and I. N. Sneddon, 1967: *Spherical harmonics.* 3d ed., Pergamon Press, 349 pp.

Mann, K. H. and J. R. N. Lazier, 2006: Ocean basin circulation: The biology of major currents, gyres, rings, and eddies. *Dynamics of marine ecosystems: biological-physical interactions in the oceans*, Blackwell Publishing, 3d ed.

Marshall, J., 1981: On the parameterization of geostrophic eddies in the ocean. *J. Phys. Oceanogr.*, **11 (2)**, 257–271, doi:10.1175/1520-0485(1981)011⟨0257: OTPOGE⟩2.0.CO;2.

Marshall, J., D. Olbers, H. Ross, and D. Wolf-Gladrow, 1993: Potential vorticity constraints on the dynamics and hydrography of the Southern Ocean. *J. Phys. Oceanogr.*, **23 (3)**, 465–487, doi:10.1175/1520-0485(1993)0232.0.CO;2.

Marshall, J. and T. Radko, 2003: Residual-mean solutions for the Antarctic Circumpolar Current and its associated overturning circulation. *J. Phys. Oceanogr.*, **33 (11)**, 2341–2354, doi:10.1175/1520-0485(2003)0332.0.CO;2.

Marshall, J. and K. Speer, 2012: Closure of the meridional overturning circulation through Southern Ocean upwelling. *Nature Geoscience*, **5 (3)**, 171–180, doi:10.1038/ngeo1391.

McCartney, M. S., 1977: Subantarctic mode water. *A Voyage of Discovery: George Deacon 70th Anniversary Volume*, M. Angel, Ed., Pergamon, New York, 103–119.

McDougall, T. and P. McIntosh, 2001: The temporal-residual-mean velocity. Part II: Isopycnal interpretation and the tracer and momentum equations. *J. Phys. Oceanogr.*, **31 (5)**, 1222–1246, doi:10.1175/1520-0485(2001)031⟨1222:TTRMVP⟩2.0.CO;2.

McIntosh, P. and T. McDougall, 1996: Isopycnal averaging and the residual mean circulation. *J. Phys. Oceanogr.*, **26**, 1655–1661.

McWilliams, J., W. Holland, and J. Chow, 1978: Description OF numerical Antarctic Circumpolar Currents. *Dyn. Atmos. Oceans*, **2 (3)**, 213–291, doi:10.1016/0377-0265(78)90018-0.

Munk, W., 1966: Abyssal recipes. *Deep Sea Res.*, **13**, 707–730.

Munk, W. and E. Palmén, 1951: Note on the dynamics of the Antarctic Circumpolar Current. *Tellus*, **3**, 53–55.

Munk, W. and C. Wunsch, 1998: Abyssal recipes II: Energetics of tidal and wind mixing. *Deep Sea Research Part I: Oceanographic Research Papers*, **45 (12)**, 1977–2010, doi:10.1016/S0967-0637(98)00070-3.

Narcowich, F. J. and J. D. Ward, 1991: Norms of inverses and condition numbers for matrices associated with scattered data. *J. Approx. Theory*, **64 (1)**, 69–94, doi:10.1016/0021-9045(91)90087-Q.

Niller, P. P. and C. J. Koblinksy, 1985: A local time-dependent Sverdrup balance in the Eastern North Pacific Ocean. *Science*, **229 (4715)**, 754–756.

Nowlin, W. and J. Klinck, 1986: The physics of the Antarctic Circumpolar Current. *Rev. Geophys.*, **24 (3)**, 469–491, doi:10.1029/RG024i003p00469.

Olbers, D., 1998: Comments on "On the obscurantist physics of 'form drag' in theorizing about the Circumpolar Current". *J. Phys. Oceanogr.*, **28 (8)**, 1647–1654, doi:10.1175/1520-0485(1998)028⟨1647:COOTOP⟩2.0.CO;2.

Olbers, D. and M. Visbeck, 2005: A model of the zonally averaged stratification and overturning in the Southern Ocean. *J. Phys. Oceanogr.*, **35 (7)**, 1190–1205, doi:10.1175/JPO2750.1.

Orsi, A. H., T. Whitworth, and W. D. Nowlin, 1995: On the meridional extent and fronts of the Antarctic Circumpolar Current. *Deep-Sea Res., Part I*, **42 (5)**, 641–673.

Park, J. J., K. Kim, B. A. King, and S. C. Riser, 2005: An advanced method to estimate deep currents from profiling floats. *J. Atmos. Oceanic Technol.*, **22**, 12941304.

Pelland, N. A., C. C. Eriksen, and C. M. Lee, 2013: Subthermocline eddies over the Washington continental slope as observed by Seagliders, 2003-09. *J. Phys. Oceanogr.*, **43 (10)**, 2025–2053, doi:10.1175/JPO-D-12-086.1.

Phillips, H. and S. Rintoul, 2000: Eddy variability and energetics from direct current measurements in the Antarctic Circumpolar Current south of Australia. *J. Phys. Oceanogr.*, **30 (12)**, 3050–3076, doi:{10.1175/1520-0485(2000)030⟨3050:EVAEFD⟩2.0.CO;2}.

Piola, A. and D. Georgi, 1982: Circumpolar properties of Antarctic Intermediate Water and Subantarctic Mode Water. *Deep Sea Res., Part A*, **29 (6)**, 687–711.

Polton, J. A. and D. P. Marshall, 2007: Overturning cells in the Southern Ocean and subtropical gyres. *Ocean Sci.*, **3 (1)**, 17–30.

Qiu, B. and T. M. Joyce, 1992: Interannual variability in the midlatitude and low-latitude western North Pacific. *J. Phys. Oceanogr.*, **22 (9)**, 1062–1079.

Quak, E., N. Sivakumar, and J. D. Ward, 1993: Least squares approximation by radial functions. *SIAM journal on mathematical analysis*, **24 (4)**, 1043–1066.

Radko, T. and J. Marshall, 2006: The Antarctic Circumpolar Current in three dimensions. *J. Phys. Oceanogr.*, **36 (4)**, 651–669, doi:10.1175/JPO2893.1.

Reid, J. L., 1989: On the total geostrophic circulation of the South Atlantic Ocean: Flow patterns, tracers, and transports. *Prog. Oceanogr.*, **23 (3)**, 149–244.

Reid, J. L., 1994: On the total geostrophic circulation of the North Atlantic Ocean: Flow patterns, tracers, and transports. *Prog. Oceanogr.*, **33 (1)**, 1–92.

Reid, J. L., 1997: On the total geostrophic circulation of the Pacific Ocean: Flow patterns, tracers, and transports. *Prog. Oceanogr.*, **39 (4)**, 263–352.

Reid, J. L., 2003: On the total geostrophic circulation of the Indian Ocean: Flow patterns, tracers, and transports. *Prog. Oceanogr.*, **56 (1)**, 137–186.

Ren, L., K. Speer, and E. P. Chassignet, 2011: The mixed layer salinity budget and sea ice in the Southern Ocean. *J. Geophys. Res.-Oceans*, **116**, doi:10.1029/2010JC006634.

Rhines, P. B. and W. R. Young, 1982: A theory of the wind-driven circulation. I. Mid-ocean gyres. *J. Mar. Res.*, **40 (S)**, 559–596.

Ridgway, K. R. and J. R. Dunn, 2007: Observational evidence for a Southern Hemisphere oceanic supergyre. *Geophys. Res. Lett.*, **34 (13)**, doi:10.1029/2007GL030392.

Rintoul, S., C. Hughes, and D. Olbers, 2001: The Antarctic Circumpolar system. *Ocean Circulation and Climate*, G. Siedler, J. Church, and J. Gould, Eds., Academic Press, International Geophysics Series, Vol. 77, 271–302.

Roemmich, D., S. Riser, R. Davis, and Y. Desaubies, 2004: Autonomous profiling floats: Workhorse for broad-scale ocean observations. *Mar. Technol. Soc. J.*, **38 (2)**, 21–29.

Sabine, C. L., et al., 2004: The oceanic sink for anthropogenic CO_2. *Science*, **305 (5682)**, 367–371.

Sallee, J. B., K. Speer, and S. R. Rintoul, 2011: Mean-flow and topographic control on surface eddy-mixing in the Southern Ocean. *J. Mar. Res.*, **69 (4-6)**, 753–777.

Sanford, T. B., J. H. Dunlap, J. A. Carlson, D. C. Webb, and J. B. Girton, 2005: Autonomous velocity and density profiler: EM-APEX. *Proc. IEEE/OES Eighth Working Conf. on Current Measurement Technology, University of Southampton, United Kingdom, IEEE*, 152–156.

Schmitz, W. J., J. D. Thompson, and J. R. Luyten, 1992: The Sverdrup circulation for the Atlantic along 24°N. *J. Geophys. Res.-Oceans*, **97 (C5)**, 7251–7256.

Severini, T. A., 2000: *Likelihood Methods in Statistics*. Oxford University Press, Oxford, 380 pp.

Siani, G., et al., 2013: Carbon isotope records reveal precise timing of enhanced Southern Ocean upwelling during the last deglaciation. *Nature communications*, **4**, 2758, doi:10.1038/ncomms3758.

Siedler, G., S. M. Griffies, J. Gould, and J. Church, (Eds.) , 2013: *Ocean Circulation and Climate: A 21st Century Perspective*, International Geophysics Series, Vol. 103. Academic Press, 868 pp.

Sivakumar, N. and J. D. Ward, 1993: On the least squares fit by radial functions to multidimensional scattered data. *Numerische Mathematik*, **243**, 219–243.

Sloyan, B. and S. Rintoul, 2000: Estimates of area-averaged diapycnal fluxes from basin-scale budgets. *J. Phys. Oceanogr.*, **30 (9)**, 2320–2341, doi:{10.1175/1520-0485(2000)030⟨2320:EOAADF⟩2.0.CO;2}.

Sloyan, B. M. and S. R. Rintoul, 2001: The Southern Ocean limb of the global deep overturning circulation. *J. Phys. Oceanogr.*, **31 (1)**, 143–173.

Speer, K., S. Rintoul, and B. Sloyan, 2000: The diabatic Deacon cell. *J. Phys. Oceanogr.*, **30 (12)**, 3212–3222, doi:10.1175/1520-0485(2000)030⟨3212:TDDC⟩2.0.CO;2.

Stammer, D., 1998: On eddy characteristics, eddy transports, and mean flow properties. *J. Phys. Oceanogr.*, 727–739.

Sverdrup, H., 1933: On vertical circulation in the ocean due to the action of the wind with application to conditions within the Antarctic Circumpolar Current. *Discov. Rep.*, **7**, 139–170.

Sverdrup, H., 1947: Wind-driven currents in a baroclinic ocean; with application to the equatorial currents of the eastern Pacific. *Proc. Natl. Acad. Sci. (USA)*, **33 (11)**, 318–326.

Talley, L. D., 1988: Potential vorticity distribution in the North Pacific. *J. Phys. Oceanogr.*, **18 (1)**, 89–106.

Talley, L. D., 2003: Shallow, intermediate, and deep overturning components of the global heat budget. *J. Phys. Oceanogr.*, **33 (3)**, 530–560.

Talley, L. D., G. L. Pickard, W. J. Emery, and J. H. Swift, 2011a: Brief history of physical oceanography: Supplementary web site materials for chapter 1. *Descriptive Physical Oceanography: An Introduction*, Academic Press, 6th ed., 1–14.

Talley, L. D., G. L. Pickard, W. J. Emery, and J. H. Swift, 2011b: *Descriptive Physical Oceanography: An Introduction*. 6th ed., Academic Press, 560 pp.

Thomas, L. N., J. R. Taylor, R. Ferrari, and T. M. Joyce, 2013: Symmetric instability in the gulf stream. *Deep Sea Res., Part II*, **91**, 96–110, doi:10.1016/j.dsr2.2013.02.025.

Thompson, A. F. and A. C. Naveira Garabato, 2014: Equilibration of the Antarctic Circumpolar Current by standing meanders. *J. Phys. Oceanogr.*, **44 (7)**, 1811–1828, doi:10.1175/JPO-D-13-0163.1.

Toggweiler, J. and B. Samuels, 1995: Effect of Drake Passage on the global thermohaline circulation. *Deep Sea Res., Part I*, **42**, 477–500.

Toggweiler, J. and B. Samuels, 1998: On the ocean's large-scale circulation near the limit of no vertical mixing. *J. Phys. Oceanogr.*, **28 (9)**, 1832–1852.

Trani, M., P. Falco, E. Zambianchi, and J. B. Sallee, 2014: Aspects of the Antarctic Circumpolar Current dynamics investigated with drifter data. *Prog. Oceanogr.*, **125**, 1–15, doi:{10.1016/j.pocean.2014.05.001}.

Treguier, A. M., M. H. England, S. R. Rintoul, G. Madec, J. Le Sommer, and J.-M. Molines, 2007: Southern Ocean overturning across streamlines in an eddying simulation of the Antarctic Circumpolar Current. *Ocean Sci.*, **3 (4)**, 491–507.

Tsai, Y.-T. and Z.-C. Shih, 2006: All-frequency precomputed radiance transfer using spherical radial basis functions and clustered tensor approximation. *ACM T. Graphic.*, **25 (3)**, 967–976, doi:10.1145/1141911.1141981.

Tuch, D. S., 2004: Q-ball imaging. *Magn. Reson. Med.*, **52 (6)**, 1358–1372, doi:10.1002/mrm.20279.

Vallis, G. K., 2006: *Atmospheric and Oceanic Fluid Dynamics: Fundamentals and Large-Scale Circulation*. Cambridge University Press, 745 pp.

Viebahn, J. and C. Eden, 2012: Standing eddies in the meridional overturning circulation. *J. Phys. Oceanogr.*, **42 (9)**, 1486–1508, doi:10.1175/JPO-D-11-087.1.

Vivier, F., K. A. Kelly, and L. Thompson, 1999: Contributions of wind forcing, waves, and surface heating to sea surface height observations in the Pacific Ocean. *J. Geophys. Res.-Oceans*, **104 (C9)**, 20 767–20 788.

Watson, A. J. and A. C. Naveira Garabato, 2006: The role of Southern Ocean mixing and upwelling in glacial-interglacial atmospheric CO_2 change. *Tellus B*, **58 (1)**, 73–87, doi:10.1111/j.1600-0889.2005.00167.x.

Wunsch, C., 1999: Where do ocean eddy heat fluxes matter? *J. Geophys. Res.*, **104 (C6)**, 13 235, doi:10.1029/1999JC900062.

Wunsch, C., 2010: Toward a midlatitude ocean frequency-wavenumber spectral density and trend determination. *J. Phys. Oceanogr.*, **40 (10)**, 2264–2281.

Wunsch, C., 2011: The decadal mean ocean circulation and Sverdrup balance. *J. Mar. Res.*, **69 (2-3)**, 417–434.

Wunsch, C. and D. Roemmich, 1985: Is the North Atlantic in Sverdrup balance? *J. Phys. Oceanogr.*, **15 (12)**, 1876–1880.

VITA

Alison R. Gray was born and raised in Texas. She graduated from Rice University in 2002 with a Bachelor of Arts in Philosophy and a Bachelor of Science in Chemical Physics. At the University of Washington, she earned a Master of Science in Physical Oceanography in 2009 and a Master of Science in Applied Mathematics in 2010.